






























# The dawn of disks: unveiling the turbulent ionised gas kinematics of the galaxy population at $z \sim 4 - 6$ with JWST/NIRCam grism spectroscopy

A. Lola Danhaive <sup>1,2\*</sup>, Sandro Tacchella <sup>1,2</sup>, Hannah Übler <sup>3</sup>, Anna de Graaff <sup>4</sup>, Eiichi Egami <sup>5</sup>, Benjamin D. Johnson <sup>6</sup>, Fengwu Sun <sup>5</sup>, Santiago Arribas <sup>7</sup>, Andrew J. Bunker <sup>8</sup>, Stefano Carniani <sup>9</sup>, Gareth C. Jones <sup>1,2</sup>, Roberto Maiolino <sup>1,2</sup>, William McClymont <sup>1,2</sup>, Eleonora Parlanti <sup>3,9</sup>, Charlotte Simmonds <sup>1,2</sup>, Natalia C. Villanueva <sup>10</sup>, William M. Baker <sup>11</sup>, Daniel T. Jaffe<sup>10</sup>, Daniel Eisenstein <sup>6</sup>, Kevin Hainline <sup>5</sup>, Jakob M. Helton <sup>5</sup>, Zhiyuan Ji <sup>5</sup>, Xiaojing Lin <sup>12</sup>, Dávid Puskás <sup>1,2</sup>, Marcia Rieke <sup>5</sup>, Pierluigi Rinaldi <sup>5</sup>, Brant Robertson <sup>13</sup>, Jan Scholz <sup>1,2</sup>, Christina C. Williams <sup>14</sup>, Christopher N. A. Willmer <sup>5</sup>

Affiliations are listed at the end of the paper.

Accepted XXX. Received YYY; in original form ZZZ

## ABSTRACT

Recent studies of gas kinematics at high redshift have reported disky systems which appear to challenge models of galaxy formation, but it is unclear whether they are representative of the underlying galaxy population. We present the first statistical sample of spatially resolved ionised gas kinematics at high redshift, comprised of 272 H $\alpha$  emitters in GOODS-S and GOODS-N at redshifts  $z \approx 3.9 - 6.5$ , observed with JWST/NIRCam slitless spectroscopy and imaging from JADES, FRESCO and CONGRESS. The sample probes two orders of magnitude in stellar mass ( $\log(M_\star[M_\odot]) \approx 8 - 10$ ) and star formation rate ( $\text{SFR} \approx 0.3 - 100 M_\odot/\text{yr}$ ), and is representative down to  $\log(M_\star[M_\odot]) \approx 9$ . Using a novel inference tool, `GEKO`, we model the grism data to measure morphological and kinematic properties of the ionised gas, as probed by H $\alpha$ . Our results are consistent with a decrease of the rotational support  $v/\sigma_0$  and increase of the velocity dispersion  $\sigma_0$  with redshift, with  $\sigma_0 \approx 100$  km/s and  $v/\sigma_0 \approx 1 - 2$  at  $z \approx 3.9 - 6.5$ . We study the relations between  $\sigma_0$ , and  $v/\sigma_0$ , and different star formation tracers and find a large scatter and diversity, with the strongest correlations between  $\sigma_0$  and SFR and SFR surface density. The fraction of rotationally supported systems ( $v/\sigma_0 > 1$ ) slightly increases with cosmic time, from  $(36 \pm 6)\%$  to  $(41 \pm 6)\%$  from  $z \sim 5.5$  to  $z \sim 4.5$ , for galaxies with masses  $9 < \log(M_\star[M_\odot]) < 10$ . Overall, disks do not dominate the turbulent high-redshift galaxy population in the mass range probed by this work. When placed in the context of studies up to cosmic noon, our results are consistent with a significant increase of disk-like systems with cosmic time.

**Key words:** galaxies: kinematics and dynamics – galaxies: evolution – galaxies: high-redshift – galaxies: structure

## 1 INTRODUCTION

In the  $\Lambda$ CDM framework, galaxy evolution is driven by four key processes: the accretion of cold gas, the formation of stars from the collapse of the gas, the feedback from both stars and black holes, and galaxy-galaxy mergers. The morphology and kinematics of a galaxy trace these processes and are hence deeply connected to the galaxy’s evolutionary stage and mass assembly history. In this work, we focus on constraining the kinematics and stellar populations of galaxies in the first 2 billion years of the Universe’s history (redshifts  $z = 3.9 - 6.5$ ) to shed new light onto the interplay between these different physical processes in the assembly of galaxies.

In the simple analytical models of galaxy formation, gas flows into the centre of dark matter halos and cools to form stars. The gas conserves most of its angular momentum as it falls into the halo,

approximately reflecting the size of the halo at the time of accretion. This means that gas cooling at later times will have higher angular momentum and settle further out into an extended star-forming disk (Fall & Efstathiou 1980; Mo et al. 1998). This formalism implies that galaxies are expected to grow from the inside-out, with new stars forming in the disk.

Beyond this simple model, feedback from stars and black holes also plays an important role in regulating star formation. Stars inject momentum into the interstellar medium through supernovae, stellar winds, and radiation pressure (Ostriker & Shetty 2011; Newman et al. 2012; Shetty & Ostriker 2012; Rathjen et al. 2023). These processes heat and disrupt surrounding gas, and sufficiently strong feedback can drive strong outflows which eject gas from the galaxy entirely (Oppenheimer & Davé 2008; Oppenheimer et al. 2010; Brook et al. 2012; Übler et al. 2014). Such processes re-distribute gas and affect the kinematics of cold ( $\approx 100$  K, e.g. CO and [CII]) and, in particular, warm ionised ( $\approx 10^4$  K, e.g. H $\alpha$  and [OIII]) gas. Similarly, the

\* ald66@cam.ac.uk

accretion of baryons onto a nuclear supermassive black hole, hence triggering an active galactic nucleus (AGN), can generate powerful outflows and heavily disrupt the star formation and dynamics of its host galaxy (Silk & Rees 1998; Cattaneo et al. 2009; Kormendy & Ho 2013; Reines & Volonteri 2015; Harrison 2017; Florian et al. 2020; D’Eugenio et al. 2024). Furthermore, complex processes such as the formation of dust (Inoue 2011; Marshall et al. 2022; Matharu et al. 2023; Le Bail et al. 2024; Li et al. 2024; Schneider & Maiolino 2024) and metals (Mannucci et al. 2010; Wuyts et al. 2016a; Simons et al. 2021; Sharda et al. 2021; Boardman et al. 2023; Venturi et al. 2024), galaxy-galaxy interactions and mergers (Wright et al. 2009; Qu et al. 2010; Duan et al. 2024b; Nakazato et al. 2024; Puskás et al. 2025), and violent gas inflows (Dekel et al. 2009; Klessen & Hennebelle 2010; Gabor & Bournaud 2014; Forbes et al. 2023) can affect the morphology and kinematics of the galaxy by introducing clumpy star formation and turbulence (van den Bosch 2001; Bournaud et al. 2007; Mandelker et al. 2017; Oklopčić et al. 2017). These effects are especially important at early cosmic times when the gas fractions and overall densities are higher, causing more intense star formation, and galaxies have lower stellar masses, and are therefore less resistant to feedback processes due to their shallow potential wells (El-Badry et al. 2016; Hopkins et al. 2023). Such effects are thought to be the cause of the highly variable, or “bursty”, star formation which has been identified at high redshift (Tacchella et al. 2023; Endsley et al. 2024; Looser et al. 2024; Baker et al. 2025a; McClymont et al. 2025a; Witten et al. 2025). The direct impact of bursty star formation on the kinematics has not been directly studied, however, it has been associated with massive gas inflows and outflows on short timescales (Tacchella et al. 2020; Zhu et al. 2024; McClymont et al. 2025a; Saldana-Lopez et al. 2025) and rapid morphological evolution, including the fluctuations of galaxy sizes (El-Badry et al. 2016; McClymont et al. 2025b), implying that the impact on kinematics is likely important.

Observational studies of the local Universe paint a picture of a variety of galaxy dynamical states and morphologies, which are outcomes of their complex mass assembly history (Sales et al. 2012; Dubois et al. 2016; Tacchella et al. 2016b, 2019). Galaxies are often separated into two broad categories – star-forming spiral disk galaxies with younger stellar populations and bulge-dominated quiescent galaxies with older stellar populations (e.g., Hubble 1926; Kormendy & Kennicutt 2004; Simard et al. 2011). However, various dynamical studies have shown that the picture is more complex, with the kinematics and morphology not always tracing the state of star formation. This can be seen through the structural and dynamical variety of early-type galaxies, which are made up of both fast and slow rotators (e.g. review by Cappellari 2016).

The theoretical framework outlined above allow us to reproduce well the large population of  $M_* = 10^{9-11} M_\odot$  disk galaxies found in the local Universe (van der Wel et al. 2014; Zhu et al. 2018; Wang et al. 2020; Rigamonti et al. 2024). Studies of both ionised and molecular gas kinematics find that these star-forming disks are characterized by high rotational support and low velocity dispersions of the order of 10 – 20 km/s (Dib et al. 2006; Walter et al. 2008; Tacconi et al. 2013; Yu et al. 2019). Studies of stellar kinematics, the key tracer of mass assembly history, have found strong correlations between shape (i.e., ellipticity), age, and rotational support. This supports the idea that the young stellar populations in star-forming disks have low stellar velocity dispersions compared to the older bulge-dominated elliptical systems (Cappellari et al. 2007; Emsellem et al. 2007; Cappellari et al. 2011; Krajnović et al. 2011; Naab et al. 2014; van de Sande et al. 2018), although quiescent galaxies have been found in a variety of kinematic states (Bezanson et al. 2018; New-

man et al. 2018; Ji et al. 2024). Studies of stellar kinematics at high redshift are difficult due to detection limits of current observational facilities, with current measurements reaching  $z \approx 2 - 3$  (Newman et al. 2015; D’Eugenio et al. 2024).

The studies from the local Universe out to cosmic noon (at  $z \sim 1 - 3$ ) agree that star-forming disks grow inside out at these epochs (Muñoz-Mateos et al. 2007; Wuyts et al. 2011; van der Wel et al. 2014; Nelson et al. 2016; Ji & Giavalisco 2023), which aligns with predictions from theoretical models and cosmological simulations (Mo et al. 1998; Hasheminia et al. 2024). However, the picture becomes more complex at cosmic noon, where the bulk of the cosmic star formation occurs (Madau & Dickinson 2014). Star-forming disks exist at these epochs but they are less massive, more turbulent, thicker, and more gas-rich than in the local Universe (Genzel et al. 2017; Förster Schreiber & Wuyts 2020; Tacconi et al. 2020), and kinematic studies have shown that they are characterized by a range of dark matter profiles (Genzel et al. 2020; Bouché et al. 2022; Nestor Shachar et al. 2023). Furthermore, these star-forming galaxies have significant bulges in their cores and their specific star-formation rate (sSFR) radial profiles are roughly flat, indicating little inside-out growth on average (Tacchella et al. 2015; Mosleh et al. 2020; Jain et al. 2024).

Spatially resolved studies of ionised gas kinematics have shown that the median rotational support  $v/\sigma_0^1$  of galaxies decreases with redshift, while the intrinsic velocity dispersion  $\sigma_0$  increases, from  $\sigma_0 \sim 10 - 20$  km/s to average values of  $\sigma_0 \sim 50$  km/s at  $z \sim 2.5$  (Wisnioski et al. 2015; Price et al. 2016; Simons et al. 2017; Turner et al. 2017b; Übler et al. 2019; Wisnioski et al. 2019; Price et al. 2020) with some systems going up to  $\sigma_0 \sim 100$  km/s. Some works find that the higher turbulence is mainly driven by gravitational instabilities in the disk, with a less important role of stellar feedback (Krumholz et al. 2018; Übler et al. 2019), while others report that stellar feedback alone is sufficient to explain the measured turbulence in cold gas kinematics across redshifts (Rizzo et al. 2024). Many works find a dependence of  $\sigma_0$  on global star-formation rate (SFR) (Wisnioski et al. 2015; Arribas et al. 2014; Simons et al. 2016; Yu et al. 2019; Price et al. 2020), but some studies highlight no local dependence on SFR surface density  $\Sigma_{\text{SFR}}$  (Übler et al. 2019), whose detection would support a scenario of stellar feedback-induced turbulence. However, most works agree on the large scatter in the  $\sigma_0 - z$  relation, which could be caused by the non-disk systems probing different origins of turbulence (including mergers) from their rotationally-supported disk counterparts. Some of the increase in the measured  $\sigma_0$  could also be explained by an increased contribution of diffuse ionized gas, which typically has higher  $\sigma_0$  than gas emitted from HII regions (Della Bruna et al. 2020), to the  $H\alpha$  flux at high-redshift (Ejdetjärn et al. 2024).

All of these works highlight the importance of linking resolved studies of star formation to the stellar and gas kinematics of galaxies. Studying the dependence of  $\sigma_0$  and  $v/\sigma_0$  on both redshift and physical galaxy properties such as SFR and its evolution with cosmic time beyond  $z > 3$  is crucial to understand when and how galaxies settle into rotationally-supported systems.

Many galaxy simulations predict that, on average, disk galaxies only become prominent at  $z < 4$  (Zolotov et al. 2015; Pillepich et al. 2019; Lapiner et al. 2023; Hopkins et al. 2023; Semenov et al. 2024c), but observations in the last decade, firstly with the Atacama Large Millimeter Array (ALMA), and now with the James Webb Space Telescope (JWST) have unveiled a different picture. Studies of

<sup>1</sup> We discuss our definitions of  $v/\sigma_0$  and  $\sigma_0$  in Sec. 3.4.2

molecular gas kinematics with ALMA have found dynamically cold (typically  $v/\sigma_0 \gtrsim 4$ ) disks out to  $z \sim 6$  (Rizzo et al. 2020; Lelli et al. 2021; Pope et al. 2023), with a  $v/\sigma_0 \sim 11$  system found as early as  $z = 7.31$  (Rowland et al. 2024). Studies of ionised gas kinematics are now possible out to similar redshifts, and down to lower masses ( $\log(M_\star [M_\odot]) < 9$ ) and SFR regimes, with JWST, both with the NIRSpec integral field unit (IFU) and slit spectrograph (e.g., Arribas et al. 2024; de Graaff et al. 2024a; Übler et al. 2024), and with NIRCam slitless spectroscopy (Li et al. 2023; Nelson et al. 2023). Taken at face value, these studies imply that galaxies are able to settle into cold disks much earlier than many models are able to explain. However, it is unclear whether these studies probe a representative sample of star-forming galaxies.

Nonetheless, recent theoretical work has explored mechanisms to generate disks at high redshift, and some simulations have been successful in promoting the formation of disks beyond  $z \sim 4$  through smooth accretion of cold gas from the cosmic web filaments (Feng et al. 2015; Kohandel et al. 2024) and high resolution on-the-fly modelling of the cold interstellar medium (ISM) (Semenov et al. 2024b,a). While such efforts are encouraging, it is now crucial to understand the kinematics of high-redshift galaxies with representative statistics in order to inform the next generation of models. While purely morphological studies support this idea, with disk-like morphologies found out to  $z \sim 7$  (Ferreira et al. 2022, 2023; Robertson et al. 2023; Tohill et al. 2024; Baker et al. 2025b), there has thus far been no systemic study of ionised gas kinematics on a large galaxy sample beyond  $z = 4$ .

The NIRCam grism mode offers a unique opportunity to address the questions arising from these recent results in a statistically significant way. Its  $R \sim 1600$  ( $\Delta v = 80$  km/s at  $\lambda = 3 - 5 \mu\text{m}$ ) spectral resolution allows for the study of kinematic signatures in the resolved 2D spectra. This mode is only available in the long-wavelength filters, yielding a spatial resolution of  $\approx 0.12 - 0.16''$  ( $\approx 0.9$  kpc at  $z \approx 5$ ). One of the main benefits of slitless spectroscopy is that each exposure contains spectra for all of the galaxies in the instrument's field of view, resulting in a (relatively) unbiased large sample of galaxies to analyse. This is in contrast with slit spectrographs such as the NIRSpec micro-shutter assembly (MSA), which can benefit from greater sensitivity and higher spectral resolution, with point source resolution up to  $R \sim 4000 - 5000$  (de Graaff et al. 2024a), and lower sky background noise, but covers fewer galaxies, which are also usually specifically selected, introducing a bias that is hard to quantify. Also, the slit typically only covers part of a galaxy. However, recent efforts in using slit-stepping strategies with the NIRSpec MOS have been shown to produce integral field spectrograph (IFS) data with a significant gain in efficiency over the NIRSpec IFU (Barišić et al. 2024; Ju et al. 2025). The latter benefits from high spatial resolution ( $\approx 0.1 - 0.2''$ ) pixel-by-pixel spectra that provide resolved constraints on the kinematics of the galaxy, ideal for detailed studies of interesting systems (e.g., Arribas et al. 2024; Jones et al. 2024; Parlanti et al. 2024; Übler et al. 2024). However, the IFU's limited field of view generally implies that these studies are restricted to single objects, or relatively small samples. In order to push our understanding of if and how disks form at high redshift, the large samples offered by the NIRCam grism are crucial in order to place single/few object observations with NIRSpec MOS and IFU into a broader picture.

In this paper, we present a systematic study of  $\sim 250$  H $\alpha$  emitters at  $z = 3.9 - 6.5$  found in the First Reionization Epoch Spectroscopically Complete Observations survey (FRESCO, Oesch et al. 2023, PI: Oesch, PID: 1895), in both GOODS fields (Giavalisco et al. 2004), and the COmplete NirCam Grism REDShift Survey (CONGRESS, PIs: Egami, Sun, PID: 3577), in the GOODS-N field. We use a new

tool, the Grism Emission-line Kinematics tOol (GEKO; Danhaive et al. in prep), to combine NIRCam F444W grism measurements with NIRCam multi-band imaging from the JWST Advanced Deep Extragalactic Survey (JADES; Bunker et al. 2020; Rieke 2020; Eisenstein et al. 2023, PIs: Rieke and Lützgendorf) in order to infer morphological and kinematic constraints on the H $\alpha$  emission for each galaxy in the sample.

This paper is organised as follows. The data and their reduction are presented in Sec. 2, along with the description of the sample selection. In Sec. 3, we introduce GEKO and outline the techniques used to forward-model the NIRCam grism instrument and infer the spatially resolved kinematics of an emission line using a Bayesian inference framework and well-motivated choices of analytical models for the morphology and kinematics of the galaxy. We present our results on the redshift evolution of ionised gas and its relation to stellar populations in Sec. 4, analysing the observed trends and comparing them to studies at lower redshift. Finally, we interpret our results in the context of the fraction of rotationally supported systems and the build-up of disks with cosmic time (Sec. 5), and we summarize our findings in Sec. 6. Throughout this work we assume  $\Omega_0 = 0.315$  and  $H_0 = 67.4$  km s $^{-1}$  Mpc $^{-1}$  (Planck Collaboration et al. 2020).

## 2 OBSERVATIONS AND FINAL SAMPLE

We will begin by describing the data used in this work, along with its reduction, then proceed to outline the selection criteria used to obtain our final sample.

### 2.1 NIRCam grism

In this work, we use JWST/NIRCam wide field slitless spectroscopy (WFSS) observations in the F444W filter ( $3.9 - 5.0 \mu\text{m}$ ) in both GOODS fields obtained with FRESCO (Oesch et al. 2023) and in the F356W filter ( $3 - 4 \mu\text{m}$ ) with CONGRESS (PIs: Egami, Sun, PID: 3577) in GOODS-N. The observations for both surveys are all taken using the row-direction grisms (GRISMR mode) with modules A and B, and the spectral resolution is  $R \sim 1400 - 1650$  across the filters used.

The data reduction for these observations is described in detail in Sun et al. (2023b) and Helton et al. (2024a), so we will only provide a brief overview here. The raw data is first reduced to stage-1 products using the standard JWST pipeline. The stage-1 data is corrected by flat-fields and the sigma-clipped median sky background is subtracted from each individual exposure, and a world coordinate system (WCS) is assigned. We then use the corresponding long wavelength (LW) images taken after each grism exposure to assign every trace to an object and hence apply wavelength calibration to the 2D spectra of each galaxy. The LW images are astrometrically calibrated using the simultaneous SW exposures taken in parallel with the grism. The spectral tracing, grism dispersion, and sensitivity functions are obtained from commissioning and Cycle-1 calibration data (PID: 1076, 1536, 1537, 1538; Sun et al. 2022, 2023b). In order to obtain 2D continuum-subtracted emission-line maps from the grism data, we use row-by-row median filtering (Kashino et al. 2023) in order to remove residual continuum from the object itself and any neighbouring objects that may leave traces in the spectrum. The 2-step (iterative) median filtering used in this technique aims to ensure that the continuum is accurately removed but the emission line flux is not harmed.

Thanks to the  $\sim 3 - 5 \mu\text{m}$  range probed by the FRESCO and CONGRESS surveys, we are able to study star-forming galaxies,

through their  $H\alpha$  emission, at  $z \approx 3.9 - 6.5$ . Our sample is built following the technique from Helton et al. (2024a); Sun et al. (2024) to accurately search for  $H\alpha$  emitters at these redshifts. First, photometric redshifts are estimated using EAZY (Brammer et al. 2008) using the templates and parameters described in Helton et al. (2024a) and Hainline et al. (2024). We select sources based on their EAZY photometric redshifts  $z_{\text{phot}}$  and confidence intervals  $\Delta z_{\text{phot}} < 1$ , then extract their grism spectrum following the method outlined above. The extracted 2D spectra are then collapsed to 1D spectra using a boxcar aperture of  $0.31''$  (five NIRCcam LW pixels). For high signal-to-noise  $S/N > 5$  detections, we assign an emission line solution that minimizes the difference between the spectroscopic and photometric redshifts, then perform visual inspection to confirm the redshifts. For the final  $H\alpha$  emitter catalogue, the 1D spectra are optimally extracted with Gaussian profiles to obtain accurate spectroscopic redshifts, emission line fluxes, and their corresponding integrated  $S/N$ . We obtain 393 galaxies in CONGRESS and 189 in FRESKO that have  $H\alpha$  detections verifying  $S/N > 10$ , for a total of 582 emitters (Helton et al. 2024b, Lin et al. in prep).

## 2.2 NIRCcam imaging

There is a wealth of NIRCcam data in the GOODS fields. The FRESKO and CONGRESS grism programs obtained parallel imaging data in the F182M and F210M, and F090W and F115W filters, respectively. In addition, the FRESKO and CONGRESS footprints have a large overlap with JADES (Eisenstein et al. 2023; Rieke et al. 2023), a Guaranteed Time Observations (GTO) programme of the NIRCcam and NIRSpc instrument teams that obtained imaging of an area of  $\sim 175 \text{ arcmin}^2$  in the GOODS-S and GOODS-N fields with an average exposure time of 20 hours with 8-10 filters. For 497 out of the 582 galaxies in our  $S/N > 10$  sample, we were able to complement the FRESKO and CONGRESS imaging with wide band  $F090W$ ,  $F115W$ ,  $F150W$ ,  $F200W$ ,  $F277W$ ,  $F356W$ , and deeper  $F444W$  observations, and medium band  $F335M$  and  $F410M$  observations from JADES. For certain regions in our sample, we also use additional medium bands  $F182M$ ,  $F210M$ ,  $F430M$ ,  $F460M$ , and  $F480M$  from the JWST Extragalactic Medium Band Survey (JEMS; Williams et al. 2023) in GOODS-S. Specifically, we use high-resolution data and photometric catalogues obtained from drizzled mosaics, and the full details on the data reduction, catalogue generation, and photometry can be found in Rieke et al. (2023), and are also detailed in Robertson et al. (2024). This wide range of filters allows us to obtain tight constraints on the stellar population from spectral energy distribution (SED) fitting (Sec. 3.1) and accurate morphology priors for our inference tool (Sec. 3.4).

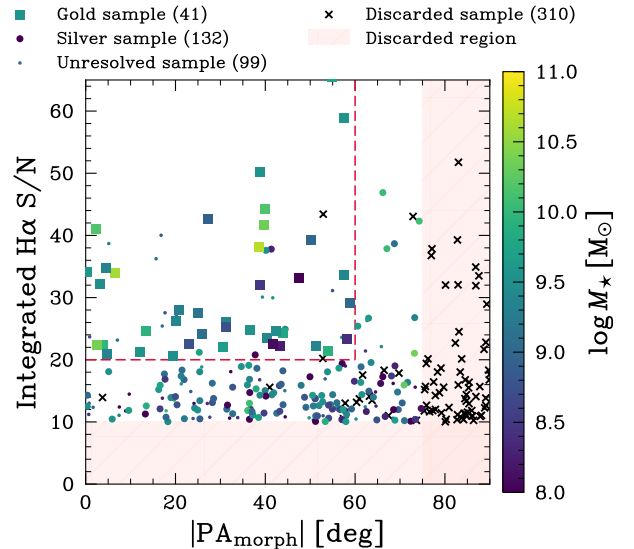
## 2.3 Sample selection

From the emission line catalogue described above, there are  $> 1000$   $H\alpha$  detections in the FRESKO and CONGRESS grism data. We introduce a  $S/N$  cut for the integrated  $H\alpha$  emission of  $S/N > 10$ , following recovery tests done on mock data (Danhaive et al. in prep), narrowing the sample down to a total of 582 galaxies. Below this  $S/N$ , we are not able to reliably constrain key kinematic properties  $\sigma_0$  and  $v/\sigma_0$ , as we discuss in Appendix D (see Fig. D1), where we present results from the testing process of our tool GEKO (Sec. 3.3). We then introduce additional cuts to separate our final sample into three categories, which are summarized in Tab. 1 and described below:

– *Gold sample*: This is the sample containing the galaxies for

Sample	$N$	$S/N$	$ \text{PA}_{\text{morph}} $ [ $^\circ$ ]	$r_e$ [ $''$ ]	$\frac{v_{\text{re}}}{\Delta v_{\text{re}}}$	$r_{\text{obs}}$
Gold	41	$> 20$	$< 60$	$> 0.12$	$> 1$	-
Silver	132	$> 10$	$< 75$	$> 0.12$	$> 1$	-
Unresolved	99	$> 10$	$< 75$	-	-	-
Extended	80	$> 10$	$< 75$	$> 0.12$	$> 1$	$> r_e$

**Table 1.** Summary of the sub-samples defined in this work and their selection criteria. The extended sample is a sub-sample of the gold and silver samples. For each category, we report the number of galaxies  $N$  it contains, the  $S/N$  cut-off, the morphological position angle  $\text{PA}_{\text{morph}}$  cut-off, the size  $r_e$  requirement. We add constraints on whether the velocity gradient at  $r_e$  has to be resolved,  $\frac{v_{\text{re}}}{\Delta v_{\text{re}}} > 1$ , where  $\Delta v(r = r_e)$  is the  $1\sigma$  lower limit, and constraints regarding the extent  $r_{\text{obs}}$  of the observed grism emission line map.



**Figure 1.** Selection of our sample in the plane of  $H\alpha$   $S/N$  and  $|\text{PA}_{\text{morph}}|$ , colour-coded by stellar mass. The discarded region highlights the parameter space in which galaxies are discarded due to low  $S/N$  and/or a  $\text{PA}$  that is too close to the dispersion direction ( $\text{PA} = 90^\circ$ ). The  $S/N = 20$  and  $|\text{PA}_{\text{morph}}| = 60^\circ$  cut-off for the gold sample is highlighted with the red dashed line. The small dots represent the unresolved sample of galaxies that have a spatial resolution below the FWHM of the  $F444W$  PSF and/or for which we do not measure a resolved velocity gradient. Based on the selection cuts described in Sec. 2.3, we obtain 41 galaxies in the gold sample, 132 in the silver sample, and 99 in the unresolved sample (see Tab. 1).

which we have the most reliable constraints. These galaxies have high integrated  $H\alpha$   $S/N$  ( $S/N > 20$ ) and have a position angle ( $\text{PA}$ ) distinct from the dispersion direction (which is at  $\text{PA}_{\text{disp}} = 90^\circ$ <sup>2</sup>):  $|\text{PA}_{\text{morph}}| < 60^\circ$ .  $\text{PA}_{\text{morph}}$  is measured from the imaging data (see

<sup>2</sup> We adopt a convention where the position angles  $|\text{PA}_{\text{morph}}|$  and  $|\text{PA}_{\text{kin}}|$  are defined from the vertical spatial  $y$ -axis in a clockwise way.

Sec. 3.2). Throughout the paper, this sample of 41 galaxies is plotted with squares.

– *Silver sample*: This sample contains the galaxies with  $S/N \geq 10$  and has a looser PA cut  $|\text{PA}_{\text{morph}}| < 75^\circ$ . Throughout the paper, this sample of 132 galaxies is plotted with circles.

– *Unresolved sample*: This sample contains the galaxies whose inferred  $r_e$  is smaller than half of the FWHM of the F444W PSF and/or whose velocity gradient is unresolved, i.e. its value is consistent with zero within  $1\sigma$ . We hence qualify galaxies as unresolved if  $|\nu(r = r_e)|/\Delta\nu(r = r_e) < 1$ , where  $\Delta\nu(r = r_e)$  is the  $1\sigma$  lower limit. This final cut can of course only be done after the kinematic fitting is completed (Sec. 3.4). This sample of 99 galaxies will be plotted with dots.

– *Extended sample*: This sample contains 80 galaxies which are in the gold or silver sample and have grism data which extends beyond the best-fit effective radius of the  $H\alpha$  emission.

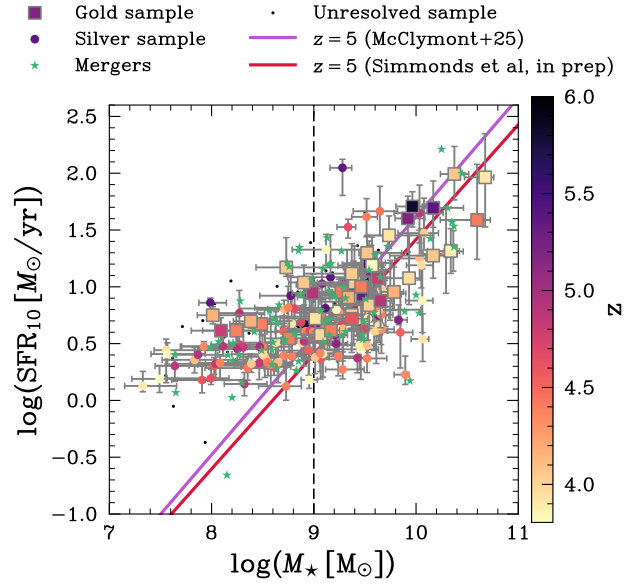
– *Discarded sample*: This sample of 310 galaxies is not included in the paper. It contains galaxies whose fits provided large residuals (often due to clumpy/merging morphology) and hence need further analysis. It also contains galaxies that are almost parallel to the dispersion direction  $|\text{PA}_{\text{morph}}| > 75^\circ$  and therefore cannot be kinematically constrained, and galaxies with a low  $H\alpha$  integrated S/N ( $S/N < 10$ ). These cuts are all based on testing done on mock data (Danhaive et al. in prep). Finally, we also discard galaxies whose best-fit kinematic and morphological position angles are in disagreement  $|\text{PA}_{\text{kin}} - \text{PA}_{\text{morph}}| > 30^\circ$ .

The gold, silver, and unresolved categories make up a total sample of 272  $H\alpha$  emitters. Fig. 1 shows the separation of the sample in these categories to highlight the cuts made. In the rest of the paper, we will plot these different samples in similar ways as this plot to distinguish them. In the 393 (CONGRESS) plus 189 (FRESCO) galaxies with  $S/N > 10$ , we found (and discarded) 108 additional objects that showed a merging structure in the NIRCcam imaging. These objects do not show clustering in their SFRs or stellar masses (Fig. 2), so discarding them should not impact our sample in this plane of parameter space. We discuss the impact of excluding these systems on our inferred disk fraction in Sec. 5.1. Additionally, 14 systems were classed as AGN due to their broad  $H\alpha$  emission in the NIRCcam grism spectra, indicative of an AGN broad line region (BLR). Out of these AGN candidates, seven are confirmed Little Red Dots (LRDs) (Matthee et al. 2024). We exclude these objects from our sample as they require multiple component modelling to account for the BLR, which is an opportunity for future study but out of the scope of this work.

We obtain SFRs and stellar masses from PROSPECTOR modelling of both photometry from NIRCcam imaging and emission line fluxes from NIRCcam grism (details in Sec. 3.1), and find that our sample is representative of galaxies on the star-forming main sequence (SFMS) at  $z \sim 5$ , as shown on Fig. 2, using the SFMS prescription from Simmonds et al. (in prep). This SFMS is derived from PROSPECTOR modelling of JADES galaxies from  $z = 3 - 9$ , 90% complete in stellar mass down to  $\log(M_\star [M_\odot]) \approx 7.5$ , presented in Simmonds et al. (2024) for GOODS-S and extended to include galaxies in GOODS-N (Simmonds et al., in prep).

We also include the prescription from the THESAN-ZOOM simulations (Kannan et al. 2025), presented in McClymont et al. (2025a). Our sample lies on the relations above  $M_\star \approx 10^9 M_\odot$ , but we note that, due to our S/N cut, the low-mass end ( $M_\star \lesssim 10^9 M_\odot$ ) of the SFMS is biased to systems that are brighter and hence more star-forming.

In terms of the redshift distribution of the galaxies in our sam-

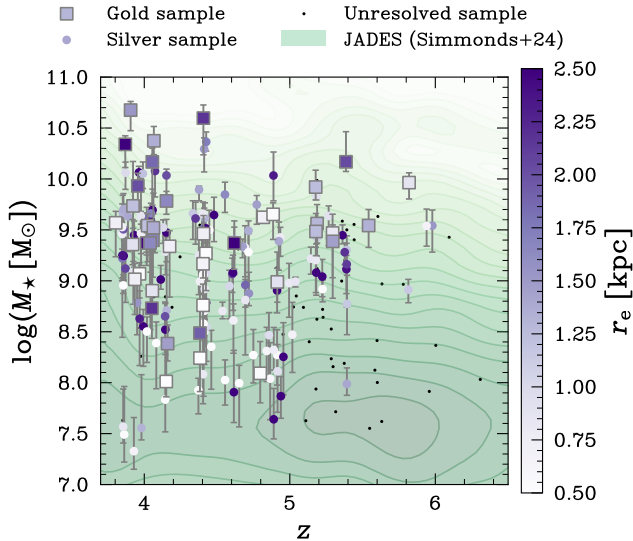


**Figure 2.** Star-formation rates ( $\text{SFR}_{10}$ ) and stellar masses ( $M_\star$ ) of our sample, derived with PROSPECTOR, colour-coded by the spectroscopic redshifts. The SFRs are averaged over 10 Myr. We compare our sample to SFMS prescriptions from McClymont et al. (2025a) and Simmonds et al. (in prep.). Our sample is representative of the star-forming galaxy population at  $M_\star > 10^9 M_\odot$  (indicated by the vertical dashed line). Below this stellar mass, because our sample selection is based on S/N in  $H\alpha$  (Fig. 1), it is biased toward high SFRs relative to the SFMS. The discarded merger sample (green stars) is evenly spread across the parameter space and discarding it does not bias our results.

ple, we show in Fig. 3 that galaxies in the lower redshift region ( $3.8 < z < 5$ ) have more galaxies and span a wider range in stellar mass. On the other hand, the higher redshift ( $5 < z < 6.5$ ) galaxies are, in comparison, biased to higher masses, where most gold and silver sample systems lying above  $M_\star \sim 10^9 M_\odot$ . The effective radii, measured from rest-frame near-UV imaging, indicate that our galaxies are representative of the population at  $z \sim 4 - 6$ , consistent with Allen et al. (2024) (see also Danhaive et al. in prep). At fixed stellar mass, galaxies span a wide range of sizes, as can be seen from the colour-coding in Fig. 3. The distribution of the UV sizes in arcseconds for the gold and silver sample galaxies (see Appendix A, Fig. A1) does not show a strong bias, although our gold sample galaxies do not probe the extended tail visible for the silver sample. Our S/N cut likely causes this bias, since at fixed stellar mass, more compact galaxies have a higher integrated S/N.

### 3 INFERRING STELLAR POPULATIONS, MORPHOLOGY, AND KINEMATICS

In order to obtain a global view of the objects in our sample, we combine NIRCcam imaging and spectroscopy, along with a wide range of techniques, to infer the stellar populations, morphologies, and kinematics of the galaxies in our sample. In Sec. 3.1, we describe our SED-fitting approach with PROSPECTOR to obtain constraints on the stellar mass and SFRs. Then, we briefly introduce our method for fitting one-component Sérsic models to our data with PYSERSIC (Sec. 3.2) in order to characterize the galaxy’s morphology. Finally, Secs. 3.3 and 3.4 introduce a novel code GEKO and describes how we use it to infer key kinematic and morphological parameters for the emission lines probed by the grism data.



**Figure 3.** Distribution of our sample in the stellar mass ( $M_*$ )-redshift plane. Our gold sample spans a wide range in stellar mass, but lies preferentially at  $z < 5$ . There are overall fewer galaxies at  $z > 5$ , with only few low mass systems ( $M_* \lesssim 10^9 M_\odot$ ) falling in the gold and silver samples. Overall, our sample probes the high mass end of photometric candidates, as shown by the green contours representative of the JADES sample from Simmonds et al. (2024, and in prep), which is expected from our S/N cut. We colour-code galaxies in the gold and silver samples by their effective radius  $r_e$  in the rest-frame near-UV, highlighting that although more massive galaxies are typically larger, at fixed stellar mass, galaxies span a wide range of sizes.

### 3.1 SED modelling

In order to characterize the stellar populations in the galaxies in our sample, we use the SED inference code PROSPECTOR (Johnson et al. 2021). We fit all of the available photometry from the JADES survey, which contains all of the NIRCcam wide and some medium band filters ( $F070W$ ,  $F090W$ ,  $F115W$ ,  $F150W$ ,  $F162M$ ,  $F200W$ ,  $F250M$ ,  $F277W$ ,  $F300M$ ,  $F335M$ ,  $F356W$ ,  $F410M$ , and  $F444W$ ), the MIRI filters  $F770W$  and  $F1280W$ , and in certain regions also included medium bands from the JEMS and FRESKO surveys ( $F182M$ ,  $F210M$ ,  $F430M$ ,  $F460M$ , and  $F480M$ ). We also use photometry from the Hubble Space Telescope (HST) Advanced Camera for Surveys (ACS) bands  $F435W$ ,  $F606W$ ,  $F775W$ ,  $F814W$ , and  $F850LP$  (the GOODS survey Dickinson et al. 2004; Giavalisco et al. 2004). Following Tacchella et al. (2023), we self-consistently model the photometry with  $H\alpha$  line fluxes from NIRCcam grism data from the FRESKO and CONGRESS surveys, and, for FRESKO galaxies in the GOODS-N field, we also include, when detected,  $[\text{OIII}]5007\text{\AA}$ ,  $[\text{OIII}]4959\text{\AA}$ ,  $H\beta$ , and  $[\text{SIII}]9533\text{\AA}$  fluxes from the CONGRESS survey.

Within PROSPECTOR, there is the option to allow for an overall rescaling of the input emission line fluxes, in order to account for potential discrepancies in the flux calibrations of the different instruments. This rescaling factor then becomes a free parameter of the model, and a difference in calibrations would likely manifest as a similar ‘‘constant’’ best-fit factor found throughout our sample. However, we find no over-arching consistent rescaling factor, meaning the best-fit value changes significantly between objects. Because the best-fit values for stellar masses and SFRs remain consistent within the uncertainties in both cases, with and without rescaling, we adopt the model with no rescaling. We also use the spectroscopic redshifts

derived from the grism spectra to fix the redshift in the fits, which allows us to break the degeneracy between redshift and physical properties such as stellar mass.

In terms of priors, we assume a non-parametric continuity star formation history (SFH) prior (Leja et al. 2019) with six SFR bins. We assume a Student’s  $t$ -distribution, with a width of  $\sigma = 0.5$ , for the ratio of the SFR in each bin, which allows for more variable SFHs than the standard continuity prior (Tacchella et al. 2022). We assume a two-component dust attenuation model (Charlot & Fall 2000; Conroy et al. 2009), where the first component (a birth-cloud component) only affects the nebular and stellar emission from young stars formed in the last 10 Myr, and the second acts on the full emission from the galaxy (a diffuse component). We use the attenuation curve from Kriek & Conroy (2013) for the diffuse dust component, where the dust bump at  $2175\text{\AA}$  is directly coupled to the dust index  $n$ , which is modelled as an offset from the Calzetti et al. (2000) attenuation curve. We include self-consistent modelling of the nebular emission, coupling the number of Lyman-continuum photons to the SFH (Byler et al. 2017).

Using the wide range of photometry and the additional constraints from the grism data, we infer key properties such as stellar mass, SFR, and dust attenuation for all of the galaxies in our sample. PROSPECTOR also produces a best-fit SFH for each galaxy, which can help inform us on the burstiness of star formation and the overall mass assembly history. Finally, we note that the definition of stellar mass that we use in this paper is the mass of stars and remnants, and not the full integral of the SFH. This effectively means that we correct the SFH integral by removing mass that is put back in the ISM.

### 3.2 Inferring morphology

In order to obtain constraints on the morphological parameters of our galaxies, we use the fully Bayesian code PYSERSIC (Pasha & Miller 2023). PYSERSIC models imaging data from any filter to infer the best fit Sérsic profile(s) parameters. We fit photometry in relevant filters (see Sec. 3.4) with a one-component Sérsic model for every galaxy in our sample to obtain estimates of the position angle  $\theta$ , ellipticity  $e$ , Sérsic index  $n$ , light centroid  $(x_0, y_0)$ , and half-light radius  $r_e$ . We note that prior to fitting, the images from JADES (Sec. 2.2) are PA-matched to the grism data in order to compare the morphological PA to the dispersion direction. Also, as described in Sec. 3.3.1, we assume an intrinsic axis ratio  $q_0$  when deriving the inclination from the ellipticity. Through this modelling, we are able to highlight mergers through their strong residual in single component fits. We also fit the continuum-subtracted grism emission line with PYSERSIC in order to obtain an estimate of the total  $H\alpha$  flux. Because of how we define the position angle from the vertical  $y$ -axis, we note the conversion  $\text{PA}_{\text{morph}} = 90 - \theta$  degrees, where  $\theta$  is the PYSERSIC output angle computed from the positive  $x$ -axis.

### 3.3 Inferring the kinematics

In this section, we describe our methods for jointly inferring morphological and dynamical parameters from imaging and grism data using the forward-modelling and Bayesian inference tool GEKO. We follow a similar methodology to Price et al. (2016), which demonstrated such a forward modelling approach for kinematic inference with only one spatial dimension (see also Li et al. 2023; de Graaff et al. 2024a). We will summarize the main aspects of the code here, but refer to an upcoming paper for a full description of the code and testing on mock and real data (Danhaive et al., in prep). We note that

in this work, we focus on the  $H\alpha$  emission, but this methodology can be extended to any other emission line.

### 3.3.1 Dynamical modelling

The simplest assumption one can make about a galaxy's kinematics is to approximate the galaxy as a thin rotating disk, which is a good assumption for the disk galaxies we observe in the local Universe. Because these exponential disks are embedded in dark matter haloes, their kinematics are well modelled by the arctangent function (Courteau 1997; Miller et al. 2011):

$$V_{\text{rot}}(r_{\text{int}}, r_t, V_a) = \frac{2}{\pi} V_a \arctan \frac{r_{\text{int}}}{r_t}, \quad (1)$$

where  $V_{\text{rot}}$  is the rotational velocity at a given radius  $r_{\text{int}}$  in the intrinsic galaxy plane,  $V_a$  is the asymptotic value that the arctangent rotation curve tends to at large radii  $r_{\text{int}} \rightarrow \infty$ , and  $r_t$  is the turn-around radius of the rotation curve. To project this velocity on the observation plane, we need to account for the galaxy's inclination  $i$ :

$$V_{\text{obs}}(x, y) = V_{\text{rot}}(r_{\text{int}}, r_t, V_a) \cdot \sin i \cdot \cos \phi_{\text{int}}, \quad (2)$$

where  $\phi_{\text{int}}$  is the polar angle coordinate in the galaxy plane. Because galaxies are thought to be thicker at high-redshift (van der Wel et al. 2014), we compute the inclination assuming an intrinsic disk axis ratio, which is the ratio of scale height to scale length,  $(b/a)_0 = q_0 = 0.2$  (Wuyts et al. 2016b; Genzel et al. 2017; Price et al. 2020; Übler et al. 2024), where  $q_0 = 0$  corresponds to the thin disk approximation. This gives for the inclination  $i$

$$\cos i = \left( \frac{q^2 - q_0^2}{1 - q_0^2} \right)^{1/2}, \quad (3)$$

where  $q = b/a$  is the measured axis ratio. We note that the choice of  $q_0$  between common values of  $q_0 = 0.0 - 0.2$  does not strongly affect the inferred kinematics properties (Förster Schreiber & Wuyts 2020; Price et al. 2020). We model a constant isotropic velocity dispersion  $\sigma_0$  across the disk based on deep adaptive optics imaging spectroscopy studies at lower redshift (Genzel et al. 2008; Förster Schreiber et al. 2018). Although some high-resolution observations of molecular and atomic gas in the local Universe have shown radially declining velocity dispersions, the observed radial changes are well below the NIRCcam grism spectral resolution (for a more detailed discussion see Übler et al. 2019, and references therein). We also introduce a velocity offset  $v_0$ , which acts as an effective redshift offset in the observed wavelength of  $H\alpha$  by shifting the full 2D emission line map. For this disk model, the free parameters are therefore the inclination  $i$ , the position angle  $\text{PA}_{\text{kin}}$ , the asymptotic velocity  $V_a$ , the turn-around radius  $r_t$ , the intrinsic velocity dispersion  $\sigma_0$ , and the net velocity offset  $v_0$ . We fix the centre of the velocity map to the centre of the light distribution  $(x_0, y_0)$ , which is fit simultaneously to the kinematics (Tab. 2). It is important to note that no assumption is made on the nature of the gravitational support (rotation or pressure). The only assumption we do is that the gaseous disk is infinitely thin, without any constraint on the amplitude of the velocities or velocity dispersions.

### 3.3.2 Morphological modelling

In order to model the flux distribution of the chosen emission line, GEKO has a parametric and non-parametric option. For the scope of this study, the parametric flux modelling was chosen due to the small observed sizes of our galaxies ( $r_{e,H\alpha} \lesssim 3$  kpc), and we will not

expand on the non-parametric model here. We parametrize the flux distribution with a Sérsic profile (Sérsic 1968):

$$I(r) = I_e \exp \left( -b_n \left[ \left( \frac{r}{r_e} \right)^{1/n} - 1 \right] \right), \quad (4)$$

where  $I_e$  is the intensity at the half-light radius  $r_e$  and  $n$  is the Sérsic index. The radius  $r$  is defined based on coordinates centred on  $(x_0, y_0)$  on the sky, which are two additional free parameters of the model. For  $b_n$ , we use the polynomial expansion from Ciotti & Bertin (1999)<sup>3</sup>, which provides a good approximation (Graham & Driver 2005). This morphological model also needs a position angle,  $\text{PA}_{\text{morph}}$ , which we let differ from the kinematic position angle, and an inclination  $i$  which we fix to the kinematic inclination.

In order to correctly sample the inner radii of the Sérsic profile, we oversample our model grid by a factor of 125. In general, the model space has 5 times the spatial resolution of the observed images and 9 times the spectral resolution of the grism data. This is to ensure that we are accurately computing our models on a fine grid before sampling down to the instrument resolution.

We obtain a 3D cube  $I(x_0, y_0, \lambda)$  by convolving the arctangent velocity field with our flux profile, with two spatial dimensions and one spectral dimension. This cube can then be collapsed onto the 2D detector plane, going from the high-resolution 3D model space to the low-resolution 2D observation space thanks to a careful forward-modelling of the instrument.

### 3.3.3 Instrument modelling

The next step in the forward modelling of grism data is to project our data cube  $I(x, y, \lambda)$  onto the NIRCcam detector plane. The instrument is defined by a well-calibrated dispersion function  $dx$  which dictates where a pixel at position  $(x_0, y_0)$  on the image and emitting at a wavelength  $\lambda_0$  will end up on the detector  $x_d = x_0 + dx$  (for full details, see Sun et al. 2023a). This function is calibrated for each filter/pupil/module combination. Due to the limited spectral extent of the region we are modelling (the emission line), we assume no spectral tracing,  $dy = 0$ . Before projecting the cube onto the detector grid  $D(x, y)$ , we convolve it with the filter-specific point spread function,  $\text{PSF}(x, y)$  and the line-spread function  $\text{LSF}(x, y)$

$$I(x, y, \lambda) \otimes \text{PSF}(x, y) \otimes \text{LSF}(\lambda) \rightarrow D(x, y).$$

The convolution is done in the high dimensional 3D model space, before collapsing to the spatial x-axis and resampling the model down to the instrument resolution. We approximate the PSF in each filter using the model PSFs (mPSFs) from Ji et al. (2024) constructed by mosaicing WebbPSF models repeatedly over the field identically to our exposure mosaics and then measuring the average PSF. The model PSFs are then resample down to the grism resolution. The wavelength-dependent one-dimensional LSF is modelled as the sum of two Gaussian distributions, to account for the broader wings. It was calibrated using SMP-LMC-058, a compact planetary nebula in the LMC (see also Jones et al. 2023) using extraction from JWST commissioning, Cycle-1 and 2 calibration observations (Sun et al., in prep.). The spectral resolution as function of wavelength is similar to the pre-launch measurements (Greene et al. 2017). Based on the measurement for the four combination of modules (A or B) and dispersion directions (R or C), we estimate a typical error on the LSF of 10%. We can now join our analytical models for galaxy morphology

<sup>3</sup>  $b(n) = 2n - 1/3 + 4/405n + 46/25515n^2 + 131/1148175n^3 - 2194697/30690717750n^4$ .

and kinematics with the forward modelling of the instrument in a Bayesian inference framework.

### 3.4 Fitting

To place the forward modelling in an inference framework, GEKO uses the Bayesian inference tool NUMPYRO (Phan et al. 2019), which is based on JAX, a python library tailored for array-oriented numerical computation, with automatic differentiation and just-in-time (JIT) compilation, and optimized for running code on graphic processing units (GPUs). This state-of-the-art approach allows us to run GEKO on a large number of galaxies, with  $\sim 20 - 60$  minutes per galaxy depending mainly on the S/N.

#### 3.4.1 Physically motivated priors

A key step when using Bayesian inference is choosing appropriate priors. In order to set informed priors for the morphological modelling, we run PYSERSIC on the F115W (or F182M) imaging for all of our objects (Sec. 3.2), obtaining PSF-deconvolved measurements of the effective radius  $r_e$ , the position angle  $\text{PA}_{\text{morph}}$ , the inclination  $i$ , the Sérsic index  $n$ , the total  $\text{H}\alpha$  flux, and the light centroid  $(x_0, y_0)$ . In our redshift range  $z \sim 3.9 - 6.5$ , F115W and F182M probe the near-UV continuum ( $\lambda_{\text{rest}} \sim 2000 \text{ \AA}$ ), so we use scaling relations to infer estimates of  $r_e$  for the  $\text{H}\alpha$  emission based on Villanueva et al. (in prep). Specifically, for our prior, we boost the near-UV sizes by a factor of 1.58, which is also consistent with the measured increase of  $\text{H}\alpha$  equivalent widths at large radii (Matharu et al. 2024; Nelson et al. 2024).

In Villanueva et al. (in prep), they carefully model and subtract the rest-optical continuum from the F356W photometry by using non-contaminated neighbouring medium band filters. They infer  $\text{H}\alpha$  morphologies at  $z \sim 4 - 5$  and compare them to the near and far UV and optical morphologies. However, this method for inferring  $\text{H}\alpha$  morphologies directly from the photometry only applies in the redshift ranges where  $\text{H}\alpha$  falls in a wide band and outside neighbouring medium bands. Also, it would be less precise at  $z > 5$  where  $\text{H}\alpha$  falls in the F444W filter, since most of the FRESCO and CONGRESS footprints have no F460M or F480M imaging, with the exception of the JEMS area where the overlap is minimal. For these reasons, we instead use the conversions they derive and use the near UV morphologies, with boosted sizes, so we can have a consistent prior for all the galaxies in our sample. Using a shorter wavelength filter also has the benefit of a smaller PSF and hence more accurate measurements.

We use Gaussian priors for all of these morphological parameters, doubling the uncertainty obtained from PYSERSIC since we are not measuring the true emission-line morphology, and to account for scatter in the relations in Villanueva et al. (in prep). For the kinematic parameters, we use uniform priors on  $\sigma_0$ ,  $V_a$ , and  $r_t$ , where this last parameter is bounded by  $r_e$ , motivated by lower redshift studies finding  $r_t \sim 0.25 r_e$  (Miller et al. 2011). The prior for the kinematic position angle  $\text{PA}_{\text{kin}}$  is the same as for  $\text{PA}_{\text{morph}}$ . The free parameters of our model and their priors are summarized in Tab. 2.

For a given set of parameters, the likelihood is computed by comparing the grism model and observations and assuming a pixel-by-pixel normal distribution. In order to sample our posterior, we use the No U-Turn Sampler (NUTS; Hoffman & Gelman 2011) which is an optimized Hamiltonian Monte Carlo (HMC) sampler. We fit the grism data, centred on the emission line of interest, to derive the posterior distributions of all of the free parameters of the model:  $i$ ,  $\text{PA}_{\text{kin}}$ ,  $r_t$ ,  $V_a$ ,  $\sigma_0$ ,  $v_0$ ,  $\text{PA}_{\text{morph}}$ ,  $r_e$ ,  $I_e$ ,  $n$ ,  $x_0$ , and  $y_0$ .

Figs. 4 and 5 show an example of the outputs of GEKO. On the top panel of Fig. 4, we show the observed continuum subtracted grism data centred on  $\text{H}\alpha$ , followed by our best fit model and the residual  $\chi$  map which is defined by:

$$\chi = \frac{\text{model} - \text{obs}}{\text{obs uncertainty}}, \quad (5)$$

and where the bounds for plotting are  $\chi = [-5, 5]$ . We also highlight the best-fit effective radius  $r_e$  of  $\text{H}\alpha$  which is well probed by the grism data. On the bottom row we show the inferred velocity, velocity dispersion, and intrinsic flux maps for  $\text{H}\alpha$ . The centre of the velocity curve is marked by a black cross on all three plots. In Fig. 5 we show the posterior distributions of all of the free parameters of the model. We also highlight the best fit values and uncertainties, computed from the 16<sup>th</sup> and 84<sup>th</sup> quantiles, for the three key kinematic parameters studied in this work: the intrinsic velocity dispersion  $\sigma_0$ , the rotational support  $v/\sigma_0$ , and the dynamical mass  $M_{\text{dyn}}$ . These last two are not free parameters of the model, and are instead derived from them.

#### 3.4.2 Model-derived parameters

We will now briefly outline our definitions for the model-derived parameters. In kinematic studies, a variety of different prescriptions are used to define rotation and dispersion, depending on how many spatial dimensions are probed by the data and on the focus of the work. In this work, and similar to Price et al. (2016, 2020), we define the intrinsic velocity dispersion  $\sigma_0$  as constant throughout the galaxy and measure it as a broadening that is equally applied across the system. In IFU studies, the velocity dispersion can be measured at (or averaged over) different radii, which can introduce differences in the derived relations (e.g., see discussion in Stott et al. 2016).

For the rotational velocity  $v_{\text{rot}}$ , and the derived rotational support  $v/\sigma_0$ , the prescriptions are even more varied. Some works measure  $v_{\text{rot}}$  at a certain radius, such as the effective radius  $r_e$  (e.g., de Graaff et al. 2024a),  $r = 2.2r_s$  (e.g., Price et al. 2016, 2020), or  $r = 2.2r_e$  (e.g., Stott et al. 2016). Others instead use the maximal observed velocity gradient across the kinematic axis (e.g., Wisnioski et al. 2015), or the maximum observed rotational velocity (e.g., Rowland et al. 2024). Due to the grism sensitivity constraints, we do not probe  $\text{H}\alpha$  emission to large enough radii and hence measurements at  $r = 2.2r_s$  or  $r = 2.2r_e$  would be extrapolations. In this work, we choose to measure the rotational velocity at the effective radius  $r_e$  because that is where we have constraints from our data. We also explore using the maximal observed rotational velocity  $v_{\text{rot}} = v_{\text{obs,max}}$ , but we do not find significant changes in our conclusions (see Appendix B for full discussion), although the quantitative trends slightly change (by  $\lesssim 10\%$ ).

In order to infer constraints on dynamical masses, we first need to compute circular velocities  $v_{\text{circ}}$ . The circular velocity is computed assuming an asymmetric drift correction to account for the pressure support (Newman et al. 2013; Wuyts et al. 2016b), which is even more prominent in the turbulent high-redshift galaxies in our sample. We hence defined this term as in Price et al. (2020)

$$v_{\text{circ}}(r) = \sqrt{v_{\text{rot}}^2(r) + 2(r/r_s)\sigma_0^2}. \quad (6)$$

At the effective radius  $r_e$ , where we compute the circular velocity  $v_{\text{circ}}(r_e)$ , we have  $2(r_e/r_s) = 3.36$  under the assumption of an

<sup>4</sup>  $r_s$  is the disk scale length  $r_s \approx 0.6r_e$  (Burkert et al. 2010; Miller et al. 2011).



Name	Parameter Description	Prior	Prior Description
PA <sub>morph</sub>	Position angle of H $\alpha$ morphology	Normal( $\mu_{PA}$ , $\sigma_{PA}$ )	Normal prior, in degrees, based on the image PYSERSIC fit results.
$i$	Inclination angle	TruncNormal <sub>[0,90]</sub> ( $\mu_i$ , $\sigma_i$ )	Truncated normal prior based on the image PYSERSIC fit results for ellipticity.
$A$	Amplitude of brightness	TruncNormal <sub>[0,\infty]</sub> ( $\mu_A$ , $\sigma_A$ )	Normal prior, in degrees, based on the grism PYSERSIC fit results.
$r_e$	Effective radius	TruncNormal <sub>[r<sub>min</sub>,r<sub>max</sub>]</sub> ( $\mu_r$ , $2 \cdot \sigma_r$ )	Truncated normal prior in pixels based on the image PYSERSIC fit results for effective radius with boosted uncertainty.
$n$	Sérsic index	Normal( $\mu_n$ , $2 \cdot \sigma_n$ )	Normal prior, in degrees, based on the image PYSERSIC fit results with boosted uncertainty.
$x_0$	X-coordinate of center	Normal( $\mu_{x_0}$ , $2 \cdot \sigma_{x_0}$ )	Normal prior, in degrees, based on the image PYSERSIC fit results with boosted uncertainty.
$y_0$	Y-coordinate of center	Normal( $\mu_{y_0}$ , $2 \cdot \sigma_{y_0}$ )	Normal prior, in degrees, based on the image PYSERSIC fit results with boosted uncertainty.
PA <sub>kin</sub>	Position angle of kinematics	Normal( $\mu_{PA}$ , $\sigma_{PA}$ )	Same prior as PA <sub>morph</sub> , but fit independently.
$V_\alpha$	Asymptotic rotational velocity	Uniform(0, 1000)	Uniform prior from 0 to 1000 km/s, with modifiable upper limit.
$\sigma_0$	Intrinsic velocity dispersion	Uniform(0, 500)	Uniform prior from 0 to 500 km/s, with modifiable upper limit.
$r_t$	Turnover radius	Uniform(0, $r_e$ )	Uniform prior from 0 to $r_e$ pixels.
$v_0$	Systemic velocity	Normal(0, 50)	Normal prior with mean 0 and standard deviation 50 km/s.

**Table 2.** Description of morphological (top section) and kinematic parameters (bottom section) being fit as free parameters in our GEKO modelling, along with their priors. For all of the parameters  $p$  with Gaussian priors based on the Pysersic modelling, we refer to the best-fit value as  $\mu_p$  and its uncertainty  $\sigma_p$ .

exponential disk. We compute the total dynamical mass following

$$M_{\text{dyn}} = k_{\text{tot}} \frac{r_e v_{\text{circ}}^2(r_e)}{G}, \quad (7)$$

where  $G$  is the gravitational constant and  $k_{\text{tot}}$  is the virial coefficient (Price et al. 2020). Because we have modelled our galaxies with  $q_0 = 0.2$ , we choose  $k_{\text{tot}} = 1.8$  as it is the coefficient for galaxies with  $q_0 = 0.2$  and  $n \sim 1 - 4$  (Price et al. 2022). The virial coefficient  $k_{\text{tot}}$  allows us to infer the total dynamical masses based on measurements out to  $r_e$ .

#### 4 THE INTERPLAY BETWEEN KINEMATICS AND STELLAR POPULATIONS FROM $Z = 0 - 6.5$

Studies out to  $z < 4$  describe the star-forming galaxy population as apparently evolving from turbulent thick disks at cosmic noon to thin disks with ordered rotation in the local Universe. In this section we extend relations between kinematics, redshift, and star formation out to  $z \gtrsim 4$  in order to understand how galaxies are growing in the early Universe. We present results from modelling with GEKO and PROSPECTOR on our final sample of  $\sim 250$  H $\alpha$  emitters. We begin by discussing the redshift evolution of the velocity dispersion  $\sigma_0$  and

rotational support  $v/\sigma_0$  in our sample, and compare our findings to cosmological simulations and low-redshift measurements (Sec. 4.1). Then, in Sec. 4.2, we analyse the relation between these two key kinematic parameters and stellar population parameters, such as stellar mass and SFRs. The median values of  $\sigma_0$  and  $v/\sigma_0$  presented in this section are summarized in Appendix A (Tabs. A2 and A1), along with the kinematic and star-forming properties of every object in the gold sample (Tab. A3). The fits for the gold sample are shown in Appendix F (Fig. F1).

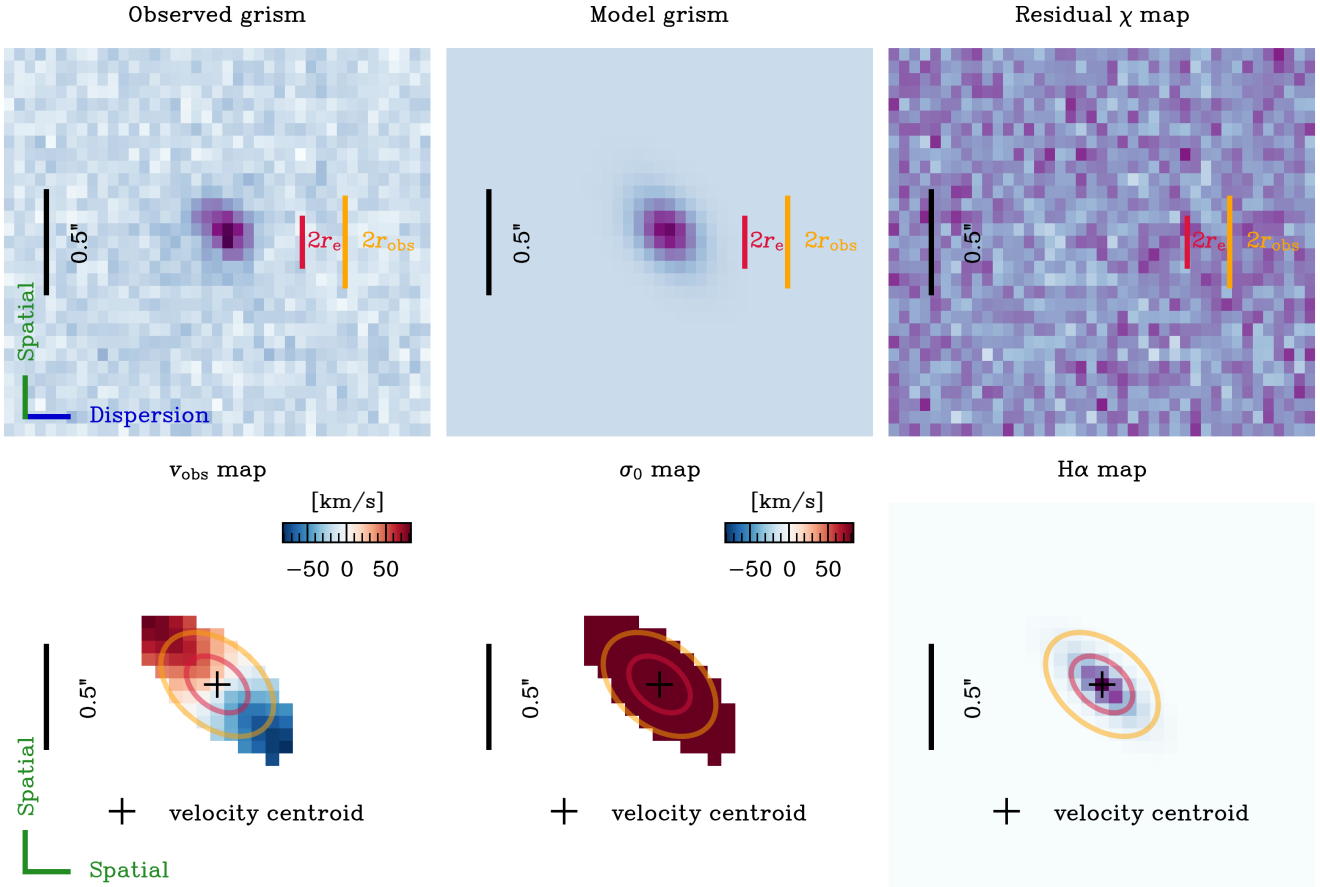
#### 4.1 Redshift evolution of ionised gas kinematics from $z = 0$ to $z \sim 6.5$

##### 4.1.1 Kinematics at $z \sim 3.9 - 6.5$

Fig. 6 shows the evolution of the intrinsic H $\alpha$  velocity dispersion  $\sigma_0$  and the rotational support  $v/\sigma_0$  as a function of redshift for the galaxies in this work. Colour-coded by stellar mass, we plot objects in our gold, silver, and unresolved samples, including upper<sup>5</sup> and lower

<sup>5</sup> For  $v/\sigma_0$ , we mark a measurement as an upper limit when the 16<sup>th</sup> quantile of the posterior distribution of  $v_{\text{re}}$  includes zero. All of the unresolved objects fall into this category. For  $\sigma_0$  measurements, upper limits are defined in a

## Object JADES ID: 1083165



**Figure 4.** Example science products obtained with `GEKO` for a galaxy in our gold sample. In the top panels, we show the observed grism data, the best-fit model, and the corresponding residuals computed with the  $\chi$  metric. The plotting range is  $\chi = [-5, -5]$ . We also highlight the best fit effective diameter  $D_e = 2r_e$  for the  $H\alpha$  emission, and the (projected) diameter of the  $S/N > 3$  observed map. In the bottom panel, we show the derived best-fit velocity field, velocity dispersion field (which has the same velocity scale as the velocity field plot), and the intrinsic  $H\alpha$  emission map. In all of the panels on the left side, we show the scale in arcseconds (black) along with the velocity centroid (black cross). In each row, we show the physical meaning of the axes (spatial vs dispersion).

limit<sup>6</sup> detections for which the value at  $1\sigma$  is plotted instead. We compute (and report in Appendix A) the median values of  $v/\sigma_0$  and  $\sigma_0$ , for three redshift bins probing  $\approx 250$  Myr, for the gold sample only (Tab. A2) and for the extended galaxies in the gold and silver samples (Tab. A1). We define galaxies as extended when the grism data extends beyond the best-fit  $H\alpha$  effective radius (see Sec. 2.3 and Tab. 1). In both cases we report measured for  $v_{\text{rot}} = v_{\text{re}}$  as well as  $v_{\text{rot}} = v_{\text{obs,max}}$  in (Tabs. A1 and A2).

We find a weak increase in the median values for the velocity dispersion  $\sigma_0$  from  $z \sim 4$  to  $z \sim 6$  for both the gold sample and the extended sample, with  $\sigma_0 = 73^{+60}_{-41}$  km/s to  $\sigma_0 = 103^{+35}_{-33}$  km/s,

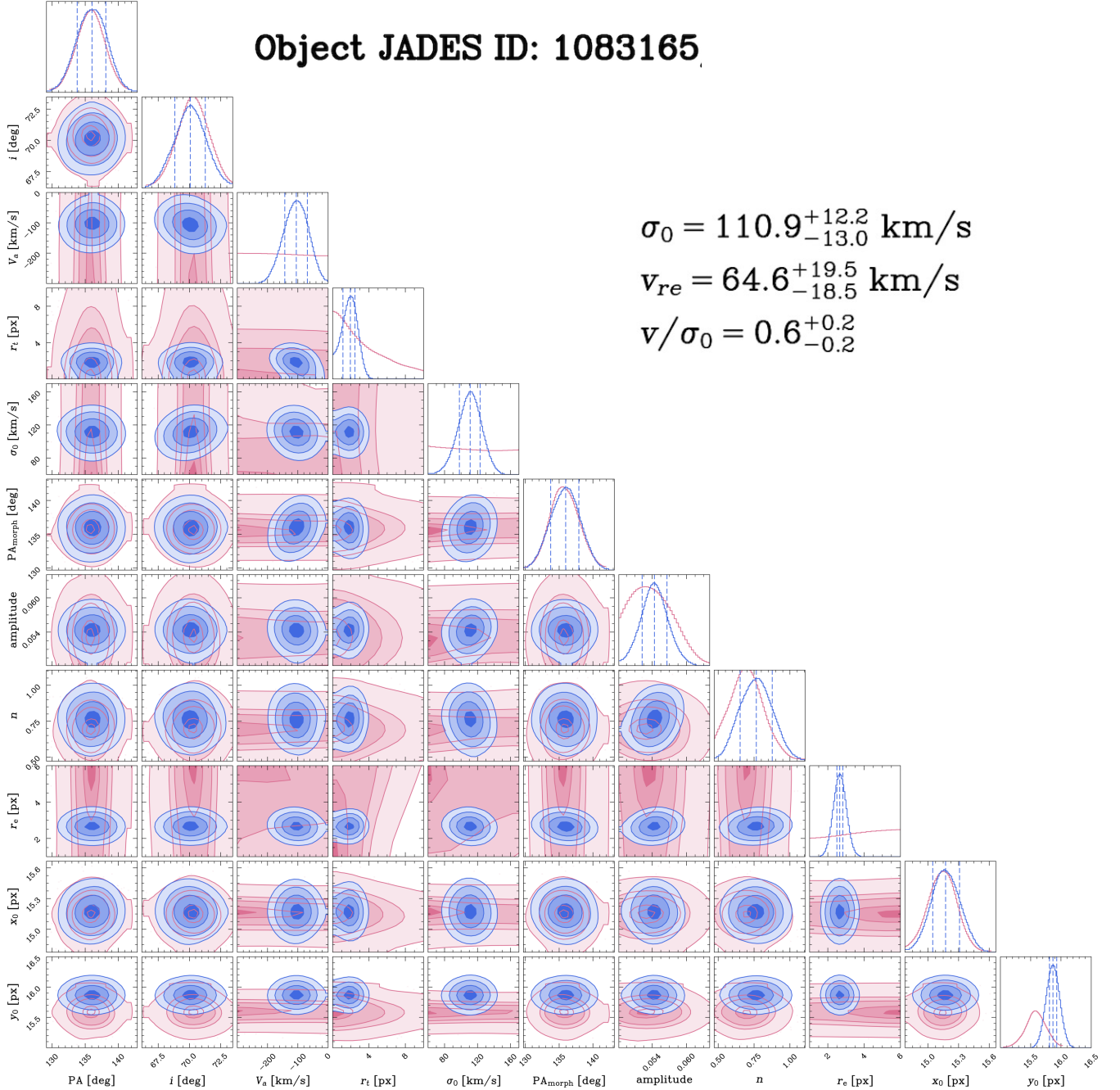
similar way but we loosen the requirement to the 16<sup>th</sup> quantile being smaller than 30 km/s, due to resolution limits.

<sup>6</sup> If the  $\sigma_0$  measurement is an upper limit for a given  $v/\sigma_0$  point, then this point is marked as a lower limit, since the ratio diverges when  $\sigma_0 \rightarrow 0$ . If a given  $v/\sigma_0$  verifies both upper and lower limits criteria, meaning its posterior distribution both coincides with zero and has a long tail, then we mark it as a lower limit since the velocity constraint is more secure than the velocity dispersion, which is rarely zero and likely only hits the limit due to resolution effects.

and with  $\sigma_0 = 77^{+55}_{-36}$  km/s to  $\sigma_0 = 98^{+40}_{-30}$  km/s, respectively. We do not find significant differences between the medians for these two subsamples. This is consistent given that they probe similar stellar mass distributions (Tab. A2). Where the high and low redshift bins probe similar stellar masses, the median mass in the central bin ( $4.2 < z < 5.0$ ) is  $\sim 0.3 - 0.4$  dex lower (Tabs. A1 and A2), which could explain the lower median value of  $\sigma_0$  found (see Sec. 4.2). We investigate the overall mass dependence of the  $\sigma_0 - z$  evolution but find no distinct trend, suggesting that the observed evolution is redshift-driven.

We find an overall mild decrease of the rotational support with redshift between  $z \sim 4$  and  $z \sim 6$  for both the gold sample and the extended sample, with  $v/\sigma_0 = 1.1^{+0.8}_{-0.5}$  to  $v/\sigma_0 = 0.8^{+1.2}_{-0.2}$  and  $v/\sigma_0 = 1.2^{+1.1}_{-0.7}$  to  $v/\sigma_0 = 0.9^{+1.3}_{-0.3}$ , respectively. Similarly to the trends for  $\sigma_0$ , we do not find significant differences in the median values for these two subsets. These low values of  $v/\sigma_0$  highlight the turbulent nature of the galaxy population at high redshift, with medians falling in the dispersion-dominated regime by  $z \sim 6$ . At  $z \sim 4 - 5$ , the medians fall in the transition region where galaxies have some rotational support but are unstable.

The large observed scatter, spanning  $\approx 0.6$  dex in  $\sigma_0$  and  $\approx 2$  dex in

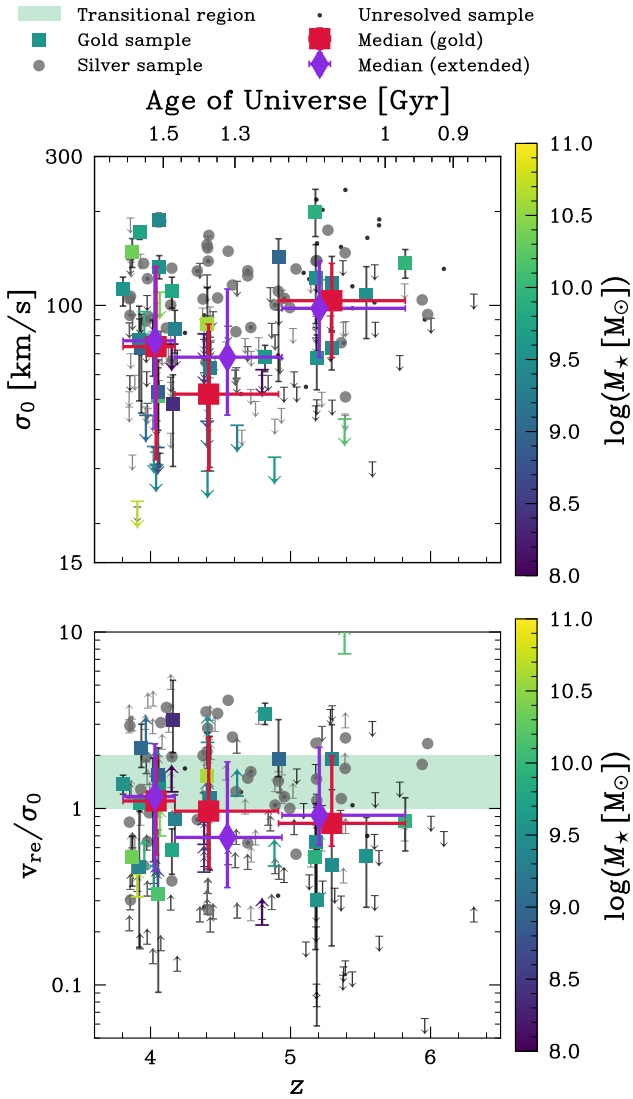
**Object JADES ID: 1083165**


**Figure 5.** Prior (pink) and posterior (blue) distributions inferred with `GEMO` for the same gold sample galaxy as in Fig. 4, for the free parameters of our model (Tab. 2). From these, we derive the posterior distributions for the rotational velocity at  $v_{re}$  and the rotational support  $v/\sigma_0$ , whose best fit values and uncertainties, computed from the 16<sup>th</sup> and 84<sup>th</sup> quantiles, are shown on the top right corner.

$v/\sigma_0$ , can in part be attributed to measurement uncertainties, which can reach  $\approx 0.3$  dex in  $\sigma_0$  and  $\approx 0.5$  dex in  $v/\sigma_0$ . However, it also highlights an intrinsic scatter in the galaxy population probed in this work, with resolved velocity dispersions spanning  $\sigma_0 \sim 50 - 200$  km/s. This can also be seen in the measurements of  $v/\sigma_0$ , with many galaxies being consistent with a dispersion-dominated state, but others reaching values  $v/\sigma_0 \sim 2 - 4$  that are consistent with turbulent disks.

Although many simulations predict that gas disks at high redshift are not highly rotationally dominated (El-Badry et al. 2018; Pillepich et al. 2019), consistent with what we see in this work, some works

also highlight the key role of undisturbed co-planar and co-rotating gas accretion in building and sustaining rotation-dominated disks (Dekel et al. 2009; Sales et al. 2012; Kretschmer et al. 2020, 2022; Kohandel et al. 2024). These disks survive until they are destroyed by external effects such counter-rotating streams and mergers, which happen on the order of a few orbital times (Dekel & Burkert 2014; Zolotov et al. 2015; Tacchella et al. 2016b,a; Dekel et al. 2020; Kretschmer et al. 2022). The effect of these processes on the measured rotational support of the gas could explain the range of  $v/\sigma_0$  values we measure on Fig. 6, where we probe galaxies in different stages of these fluctuations between disk build-up and dismantling.



**Figure 6.** Redshift evolution of the intrinsic velocity dispersion  $\sigma_0$  (top) and the rotational support  $v/\sigma_0$  (bottom) for the H $\alpha$  emitters in the gold sample (squares), silver (big circles), and unresolved (small dots) samples. The medians for the gold (red squares) and extended sample (purple diamonds), show a mild redshift evolution, for both  $\sigma_0$  and  $v/\sigma_0$ , between  $z \sim 4$  and  $z \sim 6$ . The errorbars on the medians represent the 16<sup>th</sup> and 84<sup>th</sup> quantiles along the y-axis, and the extent of the bin along the x-axis. Most of our sample lies in the dispersion supported regime ( $v/\sigma_0 < 1$ ) and the transitional regions ( $v/\sigma_0 = 1 - 2$ ; green shaded region), in part due to the high dispersions measured  $\sigma_0 \approx 100$  km/s.

#### 4.1.2 The evolution of the ionised gas velocity dispersion

We now place our measurements in the context of the other studies targeting cold and warm ionized gas across cosmic time (see Appendix E for details of each survey). For the rest of this paper, we use the term cold gas for tracers such as CO and [CII], in contrast with tracers of warmer (ionised) gas such as H $\alpha$  and [OIII]. We show the evolution of the velocity dispersion  $\sigma_0$ , shown in Fig. 7. The high values  $\sigma_0 \gtrsim 70 - 100$  km/s we find lie above measurements from cosmic noon (Wisnioski et al. 2015; Tiley et al. 2016; Simons et al. 2016; Turner et al. 2017a; Genzel et al. 2017; Übler et al. 2019; Price et al. 2020). It is important to note that many of these

	Gold sample	Extended sample
$\alpha$	$0.7 \pm 0.1$	$0.7 \pm 0.1$
$\beta$ [km/s]	$21.4 \pm 2.5$	$20.5 \pm 2.0$

**Table 3.** Best-fit parameters and uncertainties for the  $\sigma_0 = \beta(1+z)^\alpha$  relation based on our sample medians and medians from surveys at lower redshifts (Epinat et al. 2010; Simons et al. 2016; Tiley et al. 2016; Simons et al. 2017; Turner et al. 2017b).

works restrict their analyses to rotationally supported systems with  $v/\sigma_0 > 1$ , which could reduce the number of systems with high  $\sigma_0$  in their samples.

In order to quantify the evolution of  $\sigma_0$  from  $z \sim 0$  to  $z \sim 6$ , we fit our medians at  $z \sim 4$ ,  $z \sim 5$ , and  $z \sim 6$ , for the gold and extended sample, in conjunction with medians from selected surveys (Epinat et al. 2010; Simons et al. 2016; Tiley et al. 2016; Simons et al. 2017; Turner et al. 2017b) from  $z = 0$  to  $z \sim 3.5$ , following Übler et al. (2019). We fit with a power law form

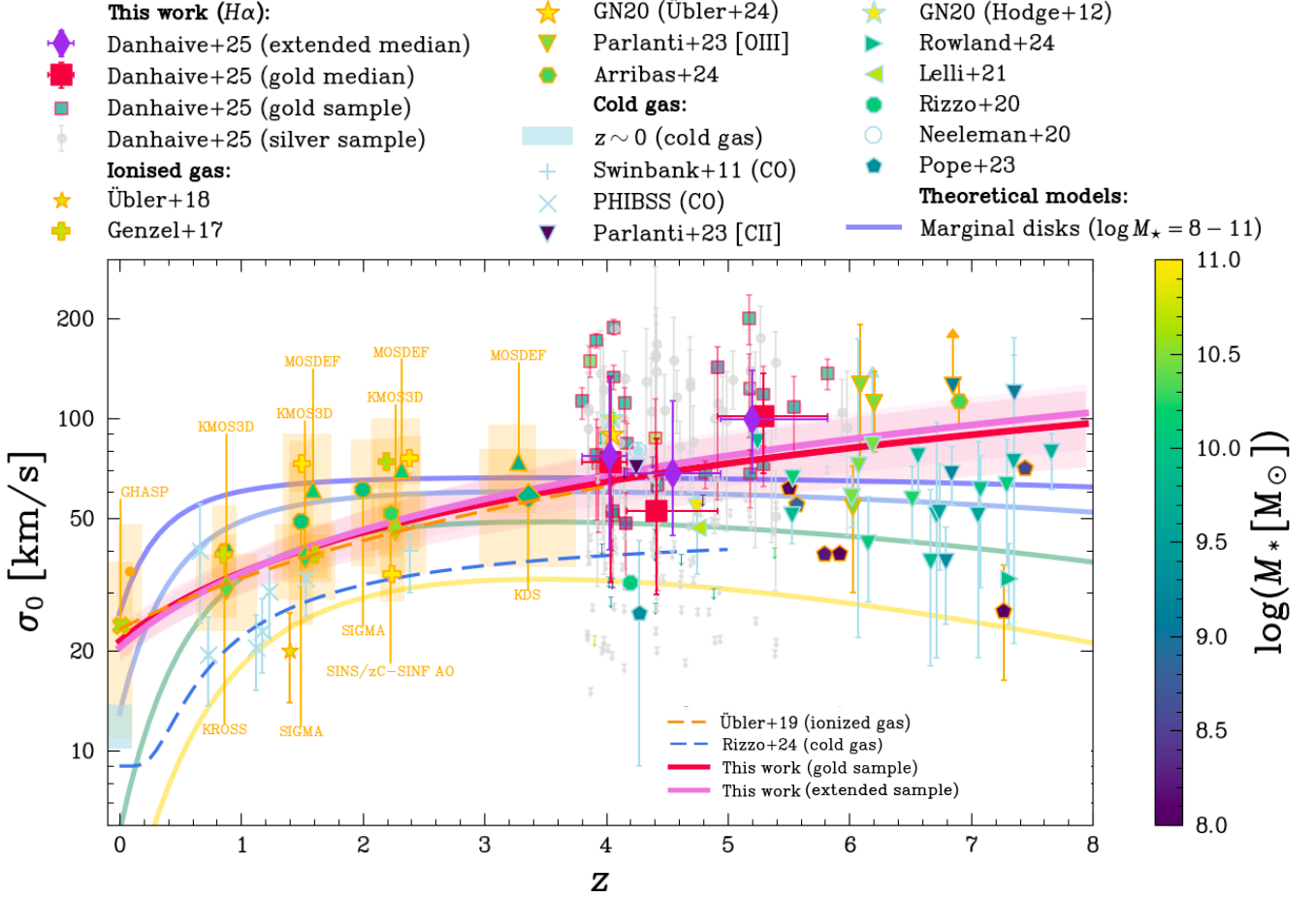
$$\sigma_0 = \beta(1+z)^\alpha, \quad (8)$$

and find the following best-fit parameters (summarized in Tab. 3):  $\alpha_{\text{gold}} = 0.7 \pm 0.1$ ,  $\beta_{\text{gold}} = 21.4 \pm 2.5$  km/s and  $\alpha_{\text{ext}} = 0.7 \pm 0.1$ ,  $\beta_{\text{ext}} = 20.5 \pm 2.0$  km/s. We plot our best-fit relations on Fig. 7. We find consistent results for the two sets of medians, indicating a soft, sub-linear, dependence of  $\sigma_0$  on  $(1+z)$ . However, 75% of galaxies from our gold sample (excluding upper limits) lie above the best-fit relation, which could suggest an even steeper increase. We note that our measurements span a large range of  $\sigma_0$ , so we cannot draw clear conclusions.

We compare our fit to the linear relation  $\sigma_0 = az + b$  from Übler et al. (2019), which is given by  $a = 9.8 \pm 3.5$  km/s,  $b = 23.3 \pm 4.9$  km/s, and is computed using the same  $z = 0 - 3.5$  median measurements. We find excellent agreement with the extrapolation of this relation to the  $z \sim 4 - 6$ , which highlights the increase of turbulence with redshift. Our velocity dispersions are in the same ranges as probed by the ionised gas measurements from Parlanti et al. (2023), although they probe higher stellar masses in general, most of which also lie above our relation. de Graaff et al. (2024a) find low values of  $\sigma_0$  that lie below the expected evolution of  $\sigma_0 - z$ , which could be driven by the low stellar masses probed  $\log M_\star [M_\odot] \approx 8$ .

When looking at cold gas tracers (i.e. CO, [CI], [CII]), the best fit exponential relation from Rizzo et al. (2024) also shows an increase in  $\sigma_0$  with redshift, with a factor of 2–3 lower normalization. Although the curve shows a flatter tail at high redshift compared to our fit for ionised gas, [CII] measurements from Parlanti et al. (2023) lie mostly above this relation, suggesting a steeper slope. The dynamically cold systems reported at high redshift (Swinbank et al. 2011; Neeleman et al. 2020; Rizzo et al. 2020; Lelli et al. 2021; Pope et al. 2023; Rowland et al. 2024) are in good agreement with the prediction from Rizzo et al. (2024), with low dispersions of  $\sigma_0 \approx 20 - 50$  km/s, which are characteristic of cold gas tracers.

In the framework of marginally stable disks, the expected evolution of  $v/\sigma_0$  and  $\sigma_0$  with redshift can be computed directly from the gas fraction using the Toomre parameter  $Q$  (Toomre 1964), which represents the instability of the disk through the turbulence in the ISM. In this empirical model, gas is accreted from the surrounding halo or cosmic web and is expelled through feedback (Förster Schreiber et al. 2006; Genzel et al. 2008; Dekel et al. 2009; Lilly et al. 2013). The Toomre parameter  $Q$  measures the equilibrium between the self-gravity of the gas and repelling forces due to turbulence and rotational support. Marginally stable disks are defined



**Figure 7.** Intrinsic  $H\alpha$  velocity dispersion  $\sigma_0$  as a function of redshift for our gold (red outlined squares) and silver (light gray circles) in the context of studies of warm ionised gas (i.e.  $H\alpha$  and  $[OIII]$ ; orange outlines) and cold gas (i.e.  $HI$ ,  $CO$ , and  $[CII]$ ; blue outlines) kinematics across redshifts. The medians for the gold and extended samples are plotted in red squares and purple diamonds, respectively. The errorbars on the medians represent the 16<sup>th</sup> and 84<sup>th</sup> quantiles along the y-axis, and the extent of the bin along the x-axis. Our results are consistent with a decrease of  $\sigma_0$  with cosmic time when compared to surveys from cosmic noon (KMOSS3D Wisnioski et al. 2015, KROSS Johnson et al. 2018, MOSDEF Price et al. 2016, 2020, KDS Turner et al. 2017b,a, SIGMA Simons et al. 2016, SINS/zC-SINF Förster Schreiber et al. 2006, 2018, PHIBSS Tacconi et al. 2013, and points from Swinbank et al. 2011; Genzel et al. 2017) and the local Universe (GHASP Epinat et al. 2010, DYNAMO Green et al. 2014, EDGE-CALIFA Bolatto et al. 2017, HERACLES Leroy et al. 2009, THINGS Walter et al. 2008, and Dib et al. 2006; blue shaded region). Our best-fit relations (Eq. 8), with (purple) and without (red) including upper limits, agree with the fit from Übler et al. (2019) (light red - long dashes), which is defined out to  $z \sim 4$ . Similarly, we also include the exponential fit for cold gas measurements from Rizzo et al. (2024) (dark blue - long dashes) defined out to  $z \sim 5$ , which highlight a similar evolution of  $\sigma_0$  tracing the cold gas, albeit with a factor 2-3 lower normalization. We compare our measurements with works at similar redshifts (Parlanti et al. 2023; Arribas et al. 2024; de Graaff et al. 2024a), as well as detection of dynamically cold systems at high-redshift Neeleman et al. (2020); Rizzo et al. (2020); Lelli et al. (2021); Pope et al. (2023); Rowland et al. (2024).

by  $Q_{\text{crit}} \sim 1$ , where  $Q_{\text{crit}} < 1$  indicates an unstable disk. In this model, the redshift evolution of  $v/\sigma_0$  and  $\sigma_0$  can be explained by the increase of gas fractions within these marginally stable disks (Genzel et al. 2011; Wisnioski et al. 2015):

$$v/\sigma_0 = \frac{a}{f_{\text{gas}}(z)Q_{\text{crit}}}, \quad (9)$$

where  $a = \sqrt{2}$  for a disk with a constant rotational velocity. In order to qualitatively compare this model to our measurements and to measurements from the literature, we plot, on Fig. 7,  $\sigma_0$  as predicted by Eq. 9 for  $Q = 1$ ,  $v = 100$  km/s, and a range of stellar masses  $\log M_{\star} [M_{\odot}] = 8 - 11$ . We derive the total gas fractions  $f_{\text{gas}} = M_{\text{gas}}/(M_{\text{gas}} + M_{\star})$  from the empirical relation derived in Tacconi et al. (2018, 2020), where  $f_{\text{gas}}(z)$  depends on total stellar mass, sSFR, and the distance from the star-forming main sequence. We plot this relation for galaxies on the main sequence.

Interestingly, the observed increase of  $\sigma_0$  with  $z$  is not well reproduced by the marginal disk model, which shows an increase of  $\sigma_0$  until cosmic noon ( $z \approx 2 - 3$ ) but then decreases slowly towards higher redshifts. When comparing our results to this model (Fig. 7), it is important to note that the Toomre marginal disk curves are at fixed stellar masses. At fixed stellar masses, the gas fraction is predicted to decrease at redshifts beyond cosmic noon, which then drives the decrease in  $\sigma_0$  (Eq. 9). However, in the measurements from observations, we probe lower and lower stellar masses with increasing redshift, so the average gas fractions would stay approximately constant, or could even increase due to the low stellar masses probed. The observed increase could also point to sources of turbulence beyond the gravitational instabilities described in the marginal disk model, such as feedback and mergers (see Secs. 5.1 and 5.2 for further discussion).

### 4.1.3 The evolution of the rotational support across cosmic time

Our results for ionised gas at  $z \sim 3.9 - 6.5$ , shown on Fig. 6, are consistent with the smooth decline in the average rotational support of galaxies with redshift. As highlighted by the Toomre instability criterion (Eq. 9), the evolution of the rotational support is deeply linked to that of the velocity dispersion, which acts as a proxy for the turbulence of the ISM. Hence, this observed decrease in  $v/\sigma_0$  with redshift is in part driven by the increase of  $\sigma_0$  with redshift.

As highlighted on Fig. 6, works from the local Universe (Epinat et al. 2010) to cosmic noon (Wisnioski et al. 2015; Simons et al. 2016; Price et al. 2020; Genzel et al. 2020) show that  $v/\sigma_0$  declines from an average of  $v/\sigma_0 \sim 10$  at  $z \sim 0 - 1$  to  $v/\sigma_0 \sim 2 - 4$  by  $z \sim 2.5 - 3.5$  for galaxies with stellar masses  $\approx 10^9 - 10^{11} M_\odot$ . In the local universe, star-forming galaxies have stellar masses up to  $\approx 10^{11} M_\odot$ , whereas studies at cosmic noon probe lower masses on average, partly driving the observed trend. These studies imply that star-forming discs are turbulent at cosmic noon and only settle into dynamically cold discs at later times. We find a further decrease to medians of  $v/\sigma_0 \approx 1$  by  $z \sim 3.9 - 6.5$ , consistent with predictions of a smooth decline of  $v/\sigma_0$  from the Illustris-TNG50 simulations, for the kinematics probed by H $\alpha$  (Pillepich et al. 2019).

Our sample probes a lower mass range than the studies in the local Universe and at cosmic noon, with the majority of galaxies in the  $\log M_\star [M_\odot] \sim 8 - 10$  range. The sample from de Graaff et al. (2024a) probes even lower masses  $\log M_\star [M_\odot] \sim 7 - 9$  but still shows a range of kinematic states. We further compare our results to the sample of ionised ([OIII]) and cold ([CII]) gas observations from Parlanti et al. (2023), which reaches out to  $z \sim 8$ . Many studies have shown that cold gas is typically less turbulent than ionised gas, resulting in overall lower velocity in both observations (e.g., Übler et al. 2019; Varidel et al. 2020; Rizzo et al. 2024) and simulations (e.g., Kohandel et al. 2024). Given these intrinsically lower velocity dispersions, as well as their higher masses (which typically imply higher rotational velocities), the measurements from Parlanti et al. (2023) are consistent with our observations of star-forming galaxies being turbulent at high redshift.

Various high-redshift dynamically cold disks have been reported with ALMA and JWST observations (Neeleman et al. 2020; Rizzo et al. 2020; Lelli et al. 2021; Pope et al. 2023; Rowland et al. 2024; Übler et al. 2024), and are plotted on Fig. 8. The first thing to note is their stellar masses. In fact, all of the galaxies reported in these works, with the exception of Pope et al. (2023), have stellar masses  $M_\star > 10^{10} M_\odot$  comparable to the star-forming discs observed at  $z < 3$ . Their high masses indicate that these systems are more evolved than their lower-mass counterparts and are not always representative of the bulk of the galaxy population at  $z \sim 3.9 - 6.5$ . For instance, the systems from Lelli et al. (2021), Rowland et al. (2024), and Übler et al. (2024) all lie close to or above the characteristic mass above which the stellar mass function at those redshifts drops exponentially (Weibel et al. 2024; Shuntov et al. 2025; Harvey et al. 2025), indicative of their extreme nature. Furthermore, all of these measurements (with the exception of Arribas et al. 2024; Übler et al. 2024) are based on cold gas tracers (CO and [CII]), which as mentioned previously typically have intrinsically lower velocity dispersions and hence higher rotational support. Finally, where we measure the rotational velocity at  $r_e$ , many of these works use different quantities such as the maximum observed velocity, which is typically higher (Rowland et al. 2024, e.g.).

In our sample, we find one system with comparable rotational support  $v/\sigma_0 \sim 10$  to these works, which is the massive galaxy previously reported in Nelson et al. (2024) as a rapidly rotating system

at  $z = 5.2$  with  $v_{\text{rot}}(r_e) = 240^{+50}_{-50}$  km/s. It is also discussed in Li et al. (2023) where they find a similar value of  $v_{\text{rot}}(r_e) = 211^{+21}_{-18}$  km/s. Our best fit value of  $v_{\text{rot}}(r_e) = 255^{+21}_{-20}$  km/s is in good agreement with these works. However, both Nelson et al. (2024) and Li et al. (2023) find low values for the rotational support,  $v/\sigma_0 \sim 2$ , in contrast with our finding of  $v/\sigma_0 \sim 10$ . This is most likely due to differences in the morphological and kinematic modelling. For example, the aforementioned works do not account for the instrument PSF and LSF when deriving the kinematics, which can heavily impact the derived velocity dispersion.

To compare our findings to the Toomre marginal disk model, we plot Eq. 9 on Fig. 8 for  $Q = 1$ , and a range of stellar masses  $\log M_\star [M_\odot] = 8 - 11$ . After a sharp decline from  $z = 0$  to  $z \sim 2$ , this model predicts nearly constant values of  $v/\sigma_0$  beyond  $z > 2$  at fixed stellar mass. This is driven by the strong dependence of gas fractions on stellar mass. In fact, most galaxies assemble the bulk of their stellar mass at cosmic noon where the cosmic SFR density peaks. At later cosmic times, galaxies are overall more massive and hence have lower gas fractions, which drives an increase in  $v/\sigma_0$  as they settle into cold disks (Eq. 9). At  $z > 2$ , the stellar masses probed are low on average  $\log M_\star [M_\odot] < 10$ , which is reflected in the high gas fractions and low values of  $v/\sigma_0$ , and, importantly, they evolve slower.

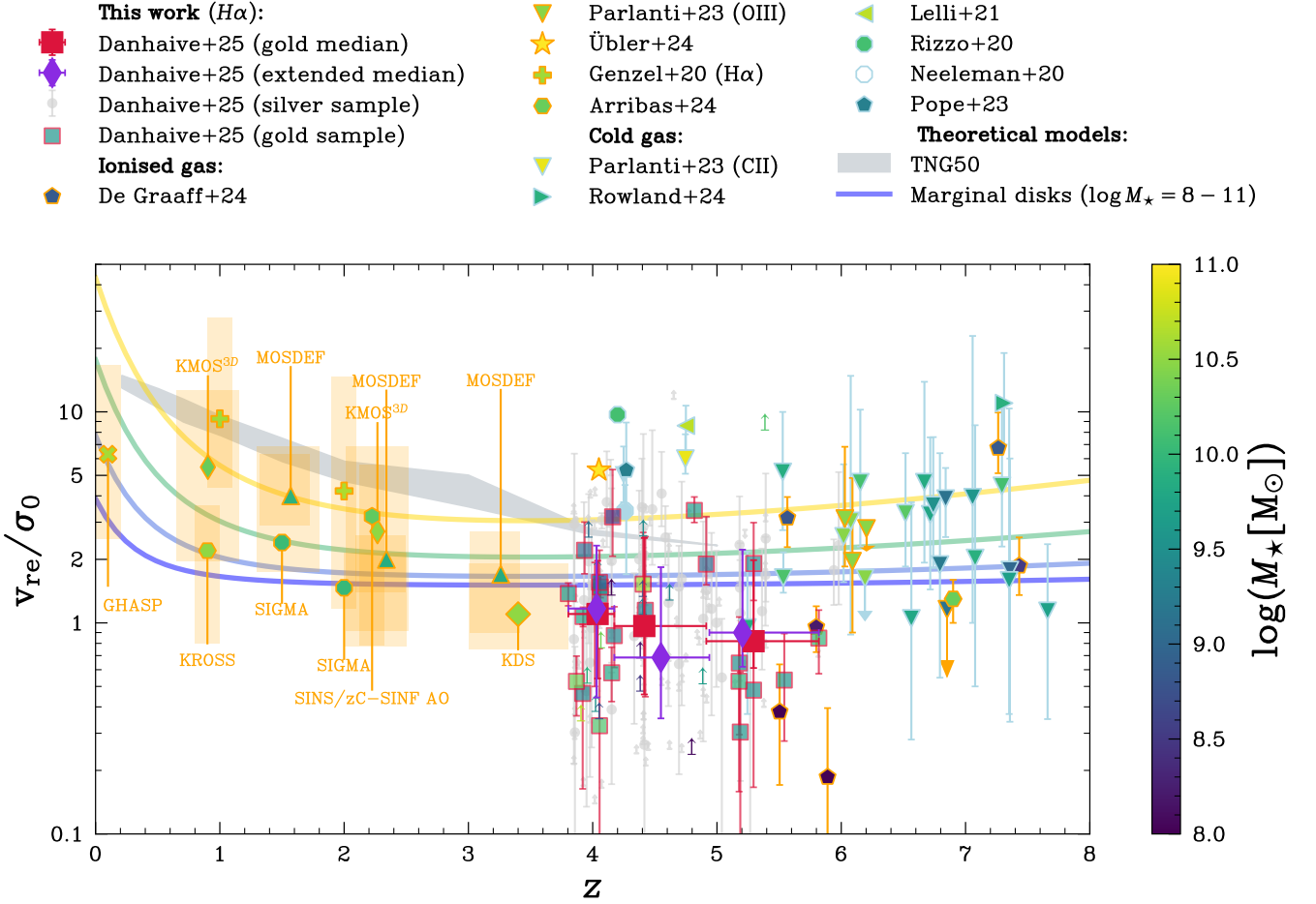
Our medians are broadly consistent with predictions from this simple model, as is the evolution of  $v/\sigma_0$  at lower redshift. This suggests that gravitational instabilities due to the high gas fraction observed in high-redshift galaxies (Tacconi et al. 2018; Parlanti et al. 2023) can drive the decrease in rotational support. Unstable disks are also qualified by fragmentation and clumpy star formation, which has been observed in this sample and other high-redshift observations (Nakazato et al. 2024). Our dispersion-supported systems naturally lie below this relation and occupy a more unstable regime, with  $Q < 1$ . The instability in these systems could be in part explained by stellar feedback and mergers, which are not accounted for in the Toomre model.

In summary, Fig. 8 shows that galaxies become increasingly turbulent at high redshift, with only the most evolved systems being able to settle into cold disks. Our findings underline high turbulence in high-redshift systems, with  $\sigma_0 \approx 100$  km/s and  $v/\sigma_0 \approx 1 - 2$  at  $z \sim 3.9 - 6.5$ . To explore what could be driving this strong increase, we will study how  $v/\sigma_0$  and  $\sigma_0$  are related to their stellar populations.

## 4.2 The effect of star formation on internal kinematics

At high redshift  $z > 3$ , the bulk of the galaxy population is in its early growth stages, and is characterized by smaller masses and sizes. These systems are hence less stable to perturbations from mergers, gas accretion, and stellar outflows, than their more evolved, low redshift counterparts. One of the characteristics of the large sample of galaxies studied in this work is the large scatter in their kinematic properties. In order to investigate what is driving the observed scatter, and to further understand the main causes of the high turbulence observed at high redshift, we look at how the velocity dispersion and rotational support correlate with other physical properties of the galaxy, specifically stellar mass  $M_\star$ , SFR averaged over the past 10 Myr ( $\text{SFR}_{10}$ ), the corresponding specific SFR ( $\text{sSFR}_{10}$ ) and SFR surface density ( $\Sigma_{\text{SFR}_{10}}$ ).  $\Sigma_{\text{SFR}_{10}}$  is computed assuming that half of the total SFR is arising from inside the half-light radius  $r_e$ :

$$\Sigma_{\text{SFR}_{10}} = \frac{\text{SFR}_{10}/2}{\pi r_e^2}. \quad (10)$$



**Figure 8.** Evolution of the rotational support  $v/\sigma_0$  with redshift for our gold (red outlined squares) and silver (light gray circles) in the context of studies of gas kinematics across redshifts. The medians for the gold and extended samples are plotted in red squares and purple diamonds, respectively. The errorbars on the medians represent the 16<sup>th</sup> and 84<sup>th</sup> quantiles along the y-axis, and the extent of the bin along the x-axis. All of our galaxies are  $7 < \log M_\star [M_\odot] \leq 10$ , and their kinematics are consistent with a decline of rotationally supported systems within our high-redshift sample, despite the presence of some rotation-supported systems (Fig. 6). They span similar  $v/\sigma_0$  values as the ones of de Graaff et al. (2024a), despite probing slightly higher masses, and are overall consistent with cold gas ([CII]) measurements (blue outlines) from Parlanti et al. (2023), who find turbulent disks at  $z \sim 6 - 7$ . Our results are placed in the context of surveys (shaded orange regions) of ionised gas (orange outline) from cosmic noon and the local Universe: MOSDEF (Price et al. 2016), KMOS3D (Wisnioski et al. 2015), SIGMA (Simons et al. 2016), SINS/zC-SINF AO (Förster Schreiber et al. 2018), KROSS (Stott et al. 2016; Tiley et al. 2016), KDS (Turner et al. 2017b,a), and GHASP (Epinat et al. 2010). We also include medians from Genzel et al. (2020), and measurements from Übler et al. (2024). We add single-object detections of dynamically cold systems in the early Universe (Rizzo et al. 2020; Neeleman et al. 2020; Lelli et al. 2021; Pope et al. 2023; Rowland et al. 2024), which probe higher masses (i.e. more evolved systems) than our sample, and an unsettled disc in a protocluster (Arribas et al. 2024). Our measurements are consistent with a decrease of  $v/\sigma_0$  with redshift as predicted by the TNG50 cosmological simulations (Pillepich et al. 2019), shown with the shaded gray region, and the Toomre (in)-stability model described in Wisnioski et al. (2011), indicated with solid lines. Within the context of lower- $z$  measurements, our results are consistent with a decline of rotational support with redshift.

We use the best fit half-light radius of the  $H\alpha$  emission, as it is the most representative of regions of recent star formation, as probed by  $SFR_{10}$ . After presenting the results for our sample (Sec. 4.2.1), we place them in the context of correlations found in other works (Sec. 4.2.2) and discuss the implications for the evolution of galaxies and the formation of disks at high redshift.

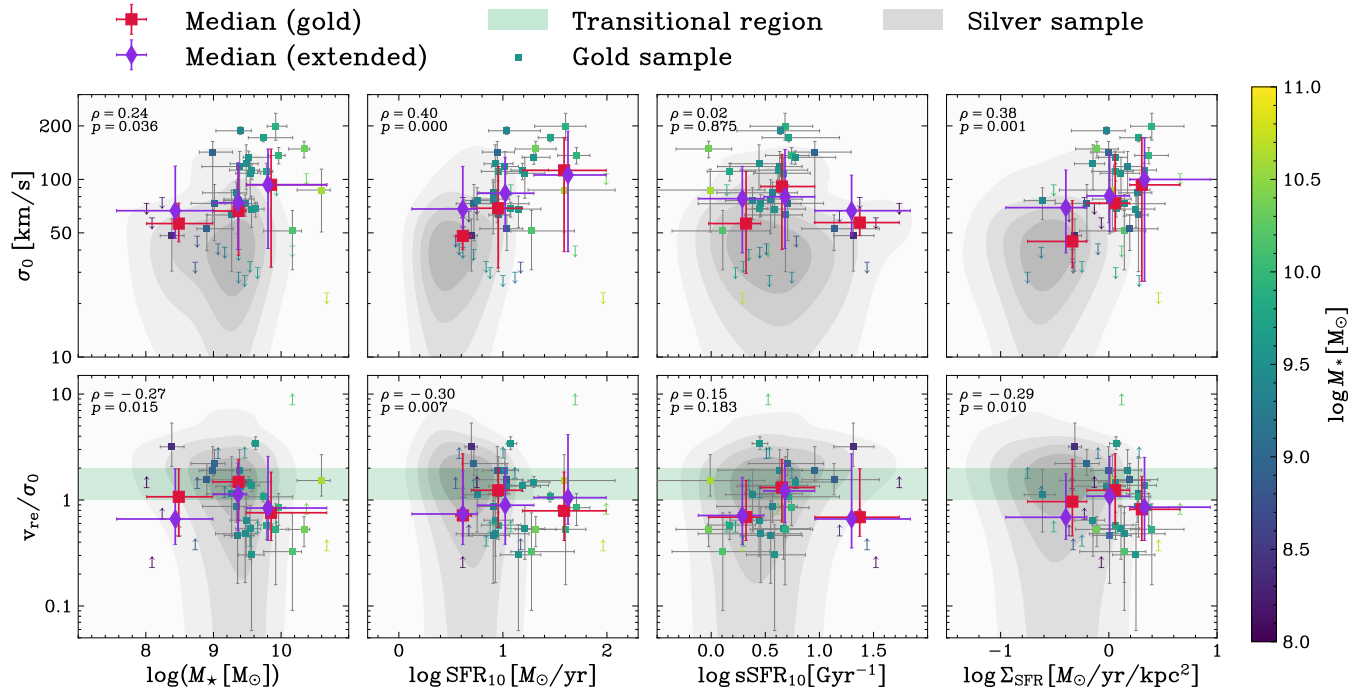
#### 4.2.1 Trends at $z \gtrsim 4$

Fig. 9 shows the evolution of  $\sigma_0$  and  $v/\sigma_0$  with  $M_\star$ ,  $SFR_{10}$ ,  $sSFR_{10}$ , and  $\Sigma_{SFR_{10}}$ , with medians plotted for the gold and extended samples, and summarized in Tabs. A1 and A2, respectively. The silver sample, highlighted in grey contours, lies on the lower portion of

the  $\sigma_0$  distribution when compared to the gold sample. This causes the gold sample medians to lie above the bulk of the silver sample measurements. Galaxies in the silver sample typically have lower  $SFR_{10}$  and  $\Sigma_{SFR_{10}}$ , but on average probe similar stellar masses and  $sSFR_{10}$  to the gold sample. This is likely due to our S/N cut, which is more lenient for the silver sample. The gold sample has the brightest  $H\alpha$  galaxies, which hence have higher SFRs and are typically more massive.

The strongest correlation<sup>7</sup> we observe is between  $\sigma_0$  and  $SFR_{10}$ , with Spearman rank coefficient  $\rho = 0.40$  and p-value  $p < 0.001$ ,

<sup>7</sup> We only discuss the correlations and medians for the extended sample, as presented on Fig. 9, but the medians of gold sample follow similar trends.



**Figure 9.** Dependence of the intrinsic velocity dispersion  $\sigma_0$  (top panels) and rotational support  $v/\sigma_0$  (bottom panels) on  $M_\star$ ,  $\text{SFR}_{10}$ ,  $\text{sSFR}_{10}$ , and  $\text{SFR}$  surface density  $\Sigma_{\text{SFR}_{10}}$  for our gold (squares) and silver sample (gray contours). We find a significant correlation between  $\sigma_0$  and  $\text{SFR}_{10}$ , which is highlighted by the running medians, for the gold sample (red squares) and for the extended sample (purple diamonds), and the Spearman rank coefficient  $\rho$  and  $p$ -value  $p$  for the resolved sample. The errorbars on the medians represent the 16<sup>th</sup> and 84<sup>th</sup> quantiles along the  $y$ -axis, and the extent of the bin along the  $x$ -axis. Both  $\sigma_0$  and  $v/\sigma_0$  show a (weaker) correlation with  $\Sigma_{\text{SFR}_{10}}$ , highlighting the role of surface density in efficiently driving turbulence in the gas. The trends with  $\text{SFR}_{10}$  and  $\Sigma_{\text{SFR}_{10}}$  are stronger for  $\sigma_0$  than  $v/\sigma_0$ , which could be caused by the fact that we probing many dispersion-supported systems ( $v/\sigma_0 < 1$ ) and systems in the transitional regions (green shaded region) between dispersion and rotation support, where stable rotation has not yet been established.

with averages going from  $\sigma_0 \approx 70 - 80$  at  $\text{SFR}_{10} = 10 M_\odot/\text{yr}$  to  $\sigma_0 \approx 100$  at  $\text{SFR}_{10} = 20 - 100 M_\odot/\text{yr}$ . This correlation naturally arises from the main physical drivers of turbulence, namely feedback from star formation and the release of gravitational energy through the radial inflow of gas through the disk (Krumholz & Burkhardt 2016; Krumholz et al. 2018), as both are connected to star-formation activity.

Our results at  $z \geq 4$  are broadly in agreement with predictions from gravitational-instability driven turbulence models (Figs. 7 and 6). This is consistent with studies finding that gravitational instabilities are the dominant source of turbulence at  $1 < z < 3$  (Krumholz & Burkhardt 2016; Krumholz et al. 2018; Übler et al. 2019). However, stellar feedback could be a more important driver of turbulence at high-redshift than at cosmic noon and in the local universe (see Sec. 4.2.2), which could explain the high values of  $\sigma_0$  that lie above the Toomre marginally stable disks.

We investigate this further, with the relevant results summarized in Appendix C. We first study the relation between  $\sigma_0$  and the offset from the main sequence  $\Delta\text{MS} = \text{SFR}/\text{SFR}_{\text{MS}}$ , but find no significant trend (Fig. C2). This is consistent with findings at cosmic noon (Übler et al. 2019) and implies that at fixed stellar masses, galaxies with higher SFRs do not show enhanced  $\sigma_0$ . This lack of enhancement does not support purely stellar feedback driven turbulence. These conclusions do not change if we include only galaxies in the conservative range of  $\log(M_\star [M_\odot]) = 9 - 10$ . We also find no trend between  $\sigma_0$  and  $\text{sSFR}_{10}$ . We explore the placement of galaxies around the MS, in Fig. C3, in relation to their kinematic properties. Although we find no overarching trend, as indicated by the lack of correlations with  $\Delta\text{MS}$ , it appears that many of the systems with high

rotational support  $v/\sigma_0 > 3$  lie close to the main sequence, particularly for the gold sample. An object-by-object analysis is needed to study the link between migrations around the MS and kinematics, but this is beyond the scope of this work.

The observed  $\sigma_0 - \text{SFR}_{10}$  correlation ( $\rho = 0.40$  and  $p < 0.001$ ) appears more significant than the one between  $\sigma_0$  and  $M_\star$  ( $\rho = 0.24$  and  $p = 0.036$ ), which suggests the latter is mainly driven by the SFMS. This is supported by predictions from theoretical models (Pillepich et al. 2019). Nonetheless, the weak correlation between  $\sigma_0$  and  $M_\star$ , and the overall distribution of the gold sample points (as seen on Fig. 9) suggests that higher mass galaxies appear to have higher velocity dispersions in our sample. Although this is somewhat physically motivated by the SFMS, it could also be due, in part, to selection effects. The less massive galaxies are typically smaller, so we could be bias to low- $\sigma_0$  systems at lower masses because the higher  $\sigma_0$  systems are too faint (see Sec. 5.3.1 for further discussion).

Finally, we find that  $\sigma_0$  correlates with  $\Sigma_{\text{SFR}_{10}}$  ( $\rho = 0.38$  and  $p = 0.001$ ), although we probe a relatively small range of parameter space. This correlation supports the idea that more compact star-forming systems have increased turbulence, but it is most likely driven by the  $\sigma_0 - \text{SFR}$  relation as we find no strong correlation between size  $r_e$  and  $\sigma_0$ .

The trends for  $v/\sigma_0$  with  $M_\star$  and SFR are weaker, suggesting they are driven by the existing relations for  $\sigma_0$ . This is supported by the fact that the rotational velocities do not strongly correlate with either of these properties (see Fig. C4). As discussed in Sec. 4.1.1, at fixed stellar masses, galaxies probe a range of kinematic states depending on external influences such as gas accretion and mergers, which can either promote or completely disrupt the formation of the disk. These



processes leave imprints on the rotational velocities and can create the observed scatter within galaxies sharing similar masses and star-forming properties. Hence, the measured rotational support  $v/\sigma_0$  in our sample at  $z \sim 4 - 6$  is mainly driven by the state of turbulence of the gas at the time of observation. As such, we expect that the kinematics of the ionised gas in these galaxies are, on average, not dominated by undisturbed circular motions, as can be seen by the low values of  $v/\sigma_0$ .

Although the correlation between  $v/\sigma_0$  and  $M_\star$  is not significant ( $\rho = -0.27$  and  $p = 0.015$ ), measurements from the gold sample show a decrease of  $v/\sigma_0$  with stellar mass, particularly at the high-mass end (Fig. 9). From studies out to cosmic noon, we would expect more massive galaxies to be more stable and hence more rotationally supported, which would result in a positive  $v/\sigma_0 - M_\star$  relation, as found in many observation and simulation-based works (e.g., Wisnioski et al. 2015; Pillepich et al. 2019; Price et al. 2020). At high redshift, this is not necessarily intuitive given some key differences such as the increased occurrence of mergers and the smaller orbital timescales. As we discuss in Sec. 4.2.2, we would, independent of redshifts, expect a flattening in the  $v/\sigma_0 - M_\star$  relation in the lower mass end ( $M_\star < 10^{10} M_\odot$ ) explored in this work. The medians for both the gold and extended samples are consistent with such a flattening. The observed decrease, when looking at the gold sample measurements, of  $v/\sigma_0$  with mass  $M_\star$  could be driven in part by observational biases, since, as previously discussed, we may be biased to low  $\sigma_0$  systems at low masses, which would decrease the number of low  $v/\sigma_0$  objects detected at low masses. However, this trend is also driven by the higher mass ( $\log M_\star [M_\odot] > 9.3$ ) dispersion-dominated systems. These systems have very high velocity dispersions  $\sigma_0 \sim 100 - 200$  km/s, not comparable to the similar-mass galaxies seen in the local Universe. It is possible that the highest-mass systems in our sample are the result of recent major mergers, as they probe the tail end of the stellar mass functions at  $z \sim 4 - 6$ . Such an event would heavily disrupt the disk and could explain the high  $\sigma_0$  values measured. We note that this trend decreases in strength and significance ( $\rho = -0.01$  and  $p = 0.93$ ) when we only include rotationally supported systems  $v/\sigma_0 > 1$  (see Appendix B, including Tab. B1).

Overall, despite a large scatter in our measurements, we find that  $\sigma_0$  correlates with star formation already at  $z \sim 4 - 6$ . The high values of  $\sigma_0$  we find could be explained by gravitational instabilities in the disk caused by radial inflows of gas, as well as a potential increase in the role of stellar feedback in injecting turbulence in the ISM.

#### 4.2.2 Drivers of turbulence across cosmic time

We now put the correlations we find between kinematic parameters and stellar populations in the context of results reported by other works across redshifts, as shown in Fig. 10. We focus on trends with  $M_\star$  and SFR, and compare our running medians to medians from studies of the local Universe (MANGA, Yu et al. 2019; SAMI, Croom et al. 2012; Johnson et al. 2018; MUSE, Bacon et al. 2010; Swinbank et al. 2017; Johnson et al. 2018), cosmic noon (KMOS3D, Wisnioski et al. 2015; MOSDEF, Price et al. (2020), SIGMA, Simons et al. 2016; KROSS, Johnson et al. 2018; SINS/zC-SINF AO, Förster Schreiber et al. 2018), and high redshift  $z \sim 4 - 8$  (Parlanti et al. 2023; de Graaff et al. 2024a). We again note that many of these works restrict their analyses to rotationally supported systems  $v/\sigma_0 > 1$ , which could also reduce the number of systems with high  $\sigma_0$  in their sample. We compute correlations for the  $v/\sigma_0 > 1$  galaxies in our sample and find no qualitative difference, although the significance of the correlations slightly varies (Tab. B1).

As shown by the colour-coding of the points by approximate red-

shift, our values (red) of  $\sigma_0 \approx 50 - 150$  km/s lie on average above values at cosmic noon (green)  $\sigma_0 \approx 30 - 70$  km/s, as well as measurements from the local Universe (blue)  $\sigma_0 \approx 20 - 50$  km/s which have the lowest dispersions on average (see also Fig. 7).

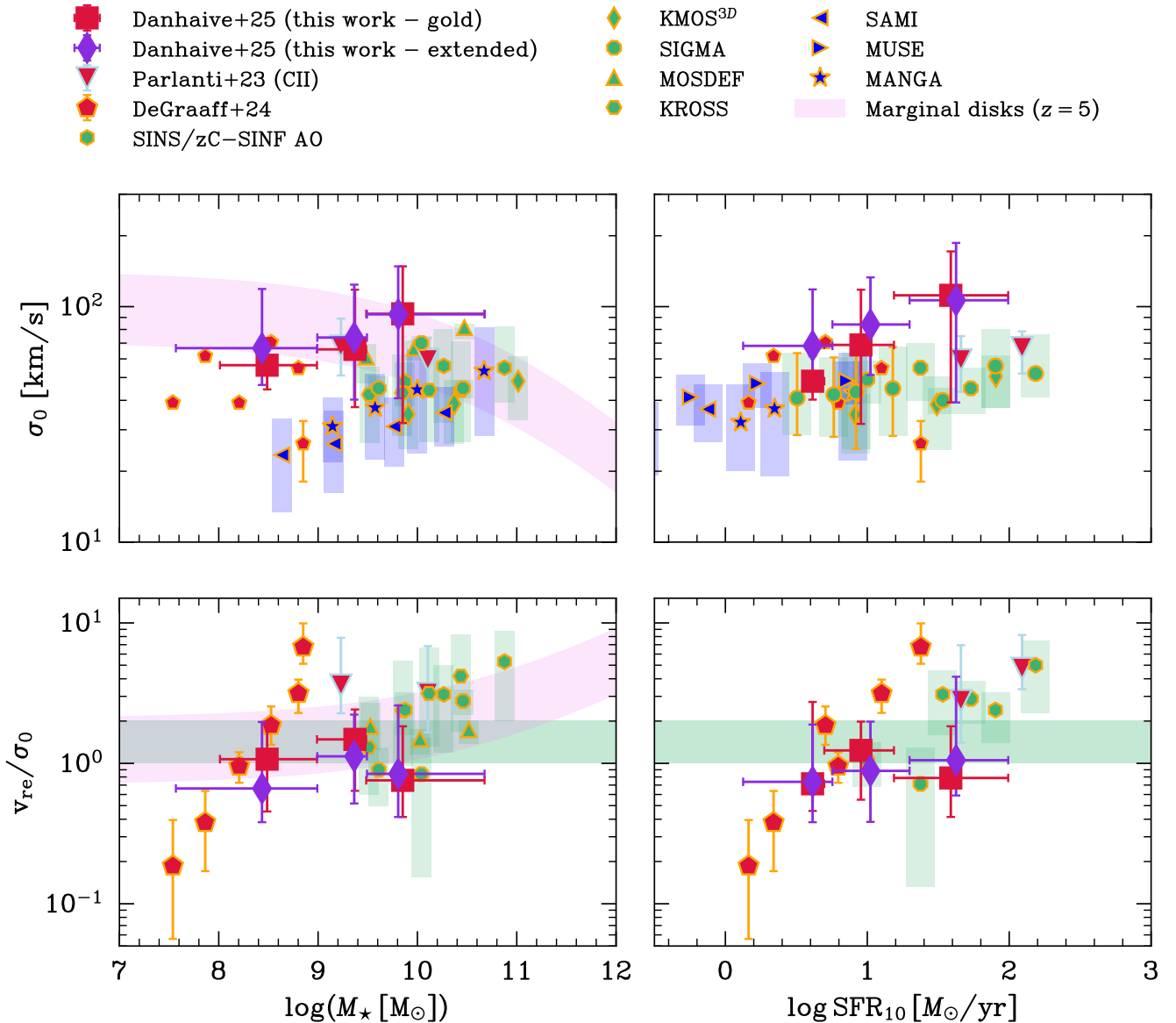
We discussed in Sec. 4.2.1 that the  $\sigma_0 - \text{SFR}$  correlation is predicted by theoretical models in which gravitational instabilities and feedback drive turbulence in the disk. These processes act at all redshifts, and explain why we observe this trend in all the surveys shown in Fig. 10. In the local Universe, several studies find a significant positive correlation of  $\sigma_0$  with SFR and  $\Sigma_{\text{SFR}}$  (Arribas et al. 2014; Yu et al. 2019; Law et al. 2022). These trends seem to hold out to cosmic noon, albeit with higher observed velocity dispersions and weaker correlations, indicative of a turbulent ISM (Förster Schreiber et al. 2009; Genzel et al. 2011; Wisnioski et al. 2015; Simons et al. 2017; Johnson et al. 2018; Übler et al. 2019; Price et al. 2020). In our work, we find that this trend is already in place at  $z \sim 4 - 6$ .

Also, the turbulence induced by these processes is expected to increase with redshift as galaxies are on average less massive, becoming less stable to gravitational instabilities and disruptions from stellar feedback (Nelson et al. 2019; Pelliccia et al. 2020). The overall decrease of gas fractions with cosmic time also promotes the decrease of turbulence in the ISM (van Donkelaar et al. 2022), as studies have shown that at high gas surface densities, and high star formation rate surface densities (Rathjen et al. 2023), the turbulence injected into the ISM from supernovae explosions can rise from  $\sigma \sim 5 - 20$  km/s (Krumholz et al. 2018) to  $\sigma \sim 50 - 60$  km/s due to strong stellar feedback (Hopkins et al. 2011) and high gas fractions (Gatto et al. 2015). All of these factors could explain why the  $\sigma_0 - \text{SFR}$  trend is steeper, and has a higher normalization, at high redshift.

The plotted medians from Parlanti et al. (2023) are from measurements of cold gas, which tend to have factors of 2 - 3 lower velocity dispersions (Übler et al. 2019; Rizzo et al. 2024). We also plot the six galaxies from de Graaff et al. (2024a), which probe the low-mass end.

Our observed mild dependence of  $\sigma_0$  with  $M_\star$  is also in agreement with past works which find a weak positive (Wisnioski et al. 2015; Turner et al. 2017b; Förster Schreiber et al. 2018; Yu et al. 2019; Übler et al. 2019; Price et al. 2020) or non-existent (Simons et al. 2017) correlation. The intrinsic correlation between stellar mass and SFR, i.e. the SFMS, implies that the  $\sigma_0 - \text{SFR}$  relation could explain most of the trend observed with stellar mass. At lower redshifts, many attribute the more fundamental correlation to SFR instead of  $M_\star$  (Wisnioski et al. 2015; Yu et al. 2019). We compare observational measurements to prediction from the marginal disk model at  $z = 5$ , and find this empirical framework predicts a negative relation between  $\sigma_0$  with  $M_\star$ . This is in contrast with findings across cosmic time on Fig. 10, which show a flat or increasing trend. The Toomre marginal disk model (Eq. 9) describes  $\sigma_0$  based on gas fractions, which are expected to decrease with mass. The observed increase of  $\sigma_0$  with  $M_\star$  suggests either higher gas fractions, than predicted by the model, at high masses, or significant contributions from other sources of turbulence.

The results for  $v/\sigma_0$  are more difficult to interpret. Starting with the  $v/\sigma_0 - M_\star$  relation, it is difficult to conclude on an overarching trend that holds at all masses. Our sample of galaxies at  $z \sim 4 - 6$  probes lower masses than lower redshift counterparts, but lies slightly above the masses from de Graaff et al. (2024a). The works from the local Universe to cosmic noon have reported positive correlations, albeit with varying strengths. However, as can be seen on Fig. 10, the trend weakens below  $\log M_\star [M_\odot] \sim 10$ , and the medians appear to flatten. The medians from Parlanti et al. (2023) also show no strong evolution between  $\log M_\star [M_\odot] \sim 9 - 10$ . Overall, the different regimes in



**Figure 10.** Dependence of  $\sigma_0$  (top panels) and  $v/\sigma_0$  (bottom panels) on stellar mass and SFR for our sample (red squares and purple diamonds) in the context of other high-redshift works (in red; Parlanti et al. 2023; de Graaff et al. 2024a), and works at cosmic noon (in green; see Fig. 7) and the local Universe (in blue; MANGA Yu et al. 2019, SAMI (Allen et al. 2015; Johnson et al. 2018; Green et al. 2018), and MUSE (Swinbank et al. 2017)). The errorbars on our plotted medians represent the 16<sup>th</sup> and 84<sup>th</sup> quantiles along the y-axis, and the extent of the bin along the x-axis. The  $\sigma_0$ -SFR relation holds across redshifts, for both ionised (H $\alpha$ ; orange outline) and cold ([CII]; blue outline) gas, although we find higher values of  $\sigma_0$  and a steeper slope. Some works at lower redshift find a similar weak increasing trend for the  $\sigma_0 - M_\star$  relation as our sample (Wisnioski et al. 2015; Förster Schreiber et al. 2018; Yu et al. 2019; Price et al. 2020), while Simons et al. (2017) finds no significant trend. The trends for  $v/\sigma_0$  are less clear, but our results could indicate a flattening in the  $v/\sigma_0 - M_\star$  relation at low masses  $\log M_\star [M_\odot] \lesssim 10$ , which is consistent with other works in this mass range and which is predicted by the marginal disk model (purple shaded regions).

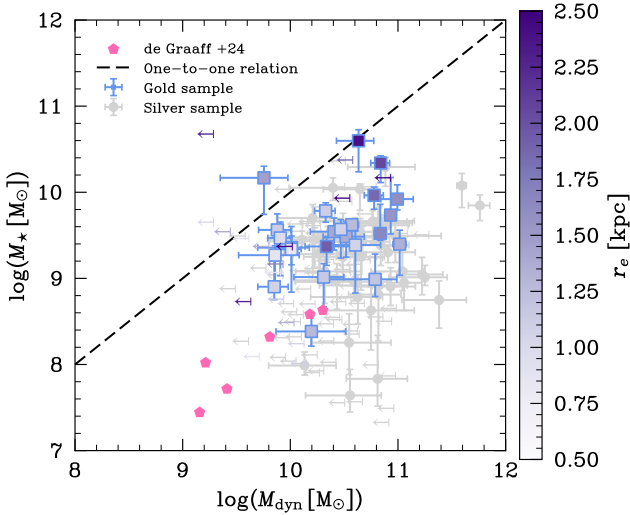
which the positive  $v/\sigma_0 - M_\star$  relations holds remain unclear, but this work provides evidence that the dependence of  $v/\sigma_0$  on  $M_\star$  weakens at lower masses. This is in line with predictions from the marginal disk model (Eq. 9), as is also discussed in Simons et al. (2016).

We do not find a significant correlation between  $v/\sigma_0$  and SFR, but measurements from the gold sample show a decreasing trend, which appears in contrast with measurements from cosmic noon on Fig. 10. However, we probe lower SFRs and overall more turbulent

systems than studies at than cosmic noon, and given the large scatter our measurement, we cannot draw a strong conclusion.

### 4.3 Comparing stellar masses and dynamical masses

Using the results from our kinematic modelling, we are able to compute dynamical masses for the objects in our sample. Dynamical masses offer insights into the dark matter content of galaxies, but for the scope of this work we only discuss them in the context of a comparison with stellar mass. We defer a detailed study of the dark



**Figure 11.** Comparison of the dynamical masses ( $M_{\text{dyn}}$ ) inferred from grism data and the stellar masses ( $M_{\star}$ ) inferred from SED fitting for our gold (blue squares), colour-coded by  $H\alpha$  size, and silver (gray circles) samples. The majority of our systems lie below the one-to-one relation (dashed line), consistent with a significant contribution to the dynamical mass from gas and/or dark matter. Six galaxies lie on the relation, potentially highlighting underestimated uncertainties on  $\sigma_0$  (see Sec. 5.3.1). We compare our values to ionised gas measurements from de Graaff et al. (2024a).

matter and baryonic mass contents of our sample to a follow-up paper (Danhaive et al, in prep).

We use our posteriors inferred with GEKO to compute the posterior distribution of the dynamical mass for each system using Eqs. 6 and 7. Eq. 7 assumes that the system is in virial equilibrium and that the measured velocity gradient is not probing non-circular motions such as outflows. In Fig. 11 we compare the dynamical masses  $M_{\text{dyn}}$  inferred from grism data to the PROSPECTOR stellar masses inferred from spectral energy distribution (SED) modelling. We expect the dynamical masses to lie above the stellar masses, as they should also incorporate the gas and the dark matter. However, both methods of inferring masses suffer from uncertainties (as can be seen from the large error bars) and caveats, so comparing the two offers a good benchmark to understand how reliable both estimates are.

Fig. 11 shows a large scatter in dynamical masses, indicating varied kinematic states and gas (and dark matter) fractions. We plot points from de Graaff et al. (2024a) for comparison, which lie well below the one-to-one relation, indicative of high gas and dark matter fractions.

We find consistent measurements  $M_{\star} < M_{\text{dyn}}$  for the majority of the galaxies in our sample, with the exception of 5 systems which lie above or on the one-to-one relation. It is difficult to evaluate the cause for this discrepancy, as it could be due to the SED fitting, the kinematics fitting, or a mixture of both. We discuss possible sources of error in the stellar mass estimate in Sec. 5.3.2. For systems  $\sigma_0$  is only an upper limits, the measurement of  $M_{\text{dyn}}$  is more uncertain. For example, we could be under-estimating the uncertainties on our  $\sigma_0$  measurements, which has a large impact on the derived upper limits (Sec. 5.3.1). If the velocity dispersions are under-estimated, this would propagate to the dynamical masses and cause the observed discrepancy in these systems.

We find an interesting system (JADES ID: 1082948) that is among the most massive in our sample, with  $\log(M_{\star} [M_{\odot}]) = 10.6^{+0.1}_{-0.2}$ , and yet shows no signs of rotation, resulting in a low dynamical mass of  $\log(M_{\star} [M_{\odot}]) = 8.9^{+0.4}_{-0.6}$ . We investigate possible reasons for this

discrepancy. Regarding the kinematic modelling, although we find a good fit of the model to the data, there could be a faint, broad  $H\alpha$  component that isn't being modelled well due to the overpowering brighter central region. Also, the best-fit results from PROSPECTOR show, despite the large uncertainties, that the galaxy has a declining SFH since the last  $\sim 20$  Myr, after peaking at  $\text{SFR} \sim 270 M_{\odot}/\text{yr}$ . This galaxy could be in a quenching epoch, as it also has a relatively small UV size,  $r_e = 1.5$  kpc, for its mass, lying below the predicted relations at  $z \sim 4$  (Allen et al. 2024; McClymont et al. 2025b). However, it lies close to the SFMS (Fig. 2), so its star formation is decreasing following a burst and it may now be entering a quenching episode. The imaging indicates that this galaxy could be in a post-merger phase. This system passed our visual inspection, where we discarded close pairs as mergers, because the clumps were too close to classify it as a merger.

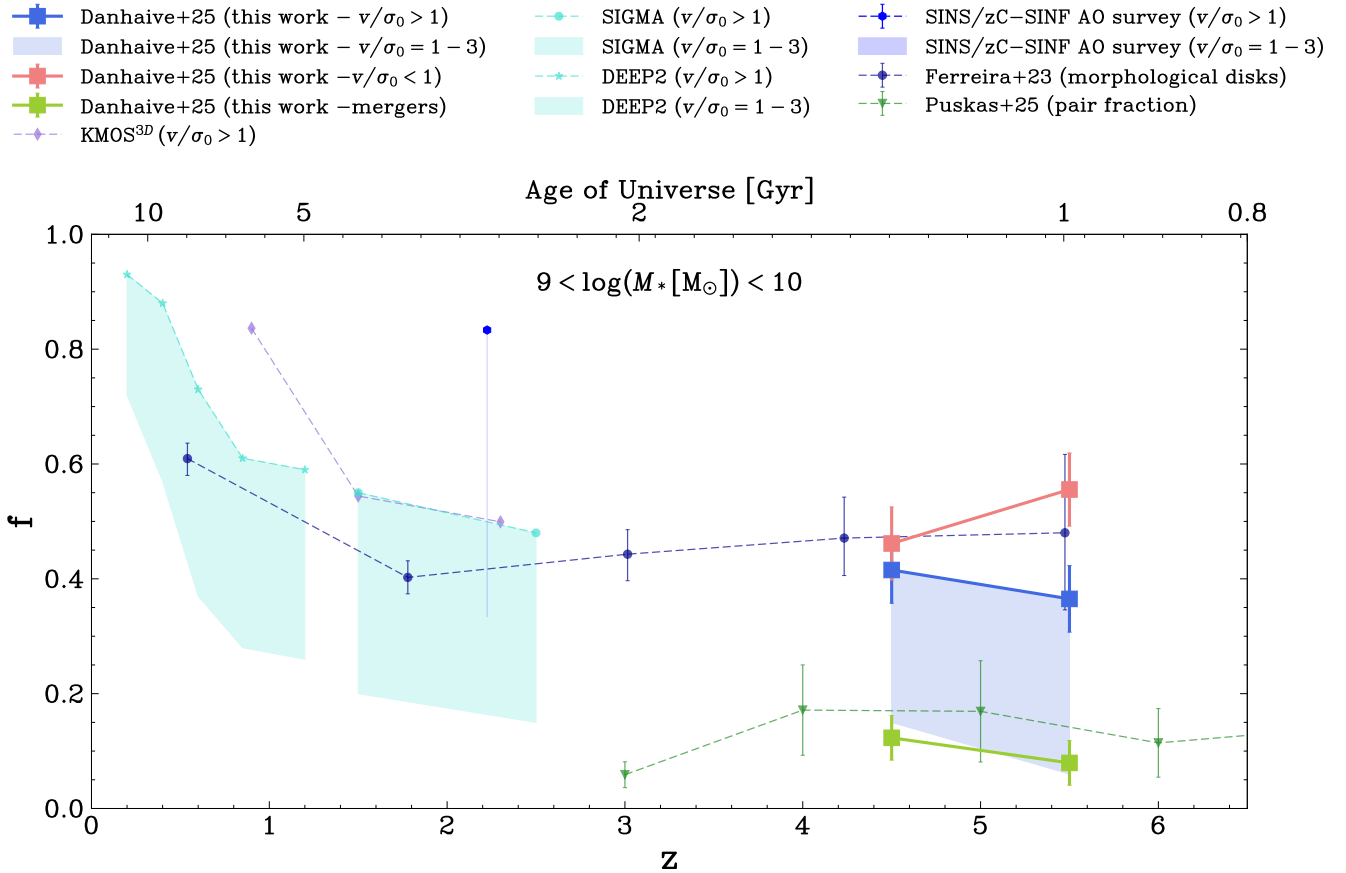
## 5 DISCUSSION

Extensive studies of galaxy kinematics from the local Universe to cosmic noon have shown that the star-forming galaxy population evolves from gas-rich star-forming thick disks at  $z \sim 2 - 3$  to dynamically cold thin disks by  $z \sim 0$ . Despite their increased turbulence (Glazebrook 2013; Wisnioski et al. 2015; Übler et al. 2019; Förster Schreiber & Wuyts 2020; Rizzo et al. 2024), the thick disks at cosmic noon can be described by many of the same key scaling relations, between kinematics and star formation related quantities, that are in place at  $z \sim 0$ , albeit with some offsets and a larger scatter (e.g. Tiley et al. 2016; Price et al. 2020; Übler et al. 2017; Sharma et al. 2024).

Our work at  $z \sim 3.9 - 6.5$  shows that in the earlier stages of galaxy formation, the picture becomes complex. As we attempt to bridge the gap between the Epoch of Reionization (EoR) and cosmic noon, it is important to remember the importance of stellar mass. Studies from  $z \sim 0$  to  $z \sim 3$  predominantly probe galaxies with  $M_{\star} \geq 10^{10} M_{\odot}$ , with the typical sample distribution peaking around  $M_{\star} \sim 10^{11} M_{\odot}$  and  $M_{\star} \sim 10^{10.5} M_{\odot}$ , respectively. At  $z \sim 4 - 6$ , we have a galaxy population dominated by systems in a lower mass slice of the parameter space  $M_{\star} \sim 10^8 - 10^{10} M_{\odot}$ . Careful consideration must therefore be given to separate pure redshift evolution from evolution mainly driven by stellar mass.

Studies have shown that even at high redshifts  $z \sim 4 - 5$ , some galaxies with stellar masses  $\log M_{\star} [M_{\odot}] \geq 10$ , comparable to those probed by the star-forming population at cosmic noon, are already able to settle into stable rotating disks (e.g., Neeleman et al. 2020; Lelli et al. 2021). However, it is not surprising that many of the low-mass systems at high redshift are turbulent and have not settled into a stable rotationally-supported state (Fig. 8). Their ISM is characterized by elevated velocity dispersions (Fig. 7), which are likely driven by increased gravitational instabilities promoted by their lower masses, high gas fractions, and the overall increase of mergers and starbursts in the early Universe. These instabilities, along with a potential contribution from stellar feedback, drive the observed correlations between SFR, and SFR surface density, and  $\sigma_0$  (Fig. 9).

Overall, the picture painted in this work is consistent with galaxies at high redshift being turbulent and changing on short timescales. In this case, we expect the prevalence of disks to be lower at  $z \geq 4$  than in the local Universe and at cosmic noon. We investigate and discuss this in the next section.



**Figure 12.** Evolution of the fraction of rotationally supported systems ( $v/\sigma_0 > 1$ ) with redshift for our sample (blue lines) and for kinematic samples (Simons et al. 2017; Förster Schreiber et al. 2018; Wisnioski et al. 2019) and morphological sample (Ferreira et al. 2023) from the literature (blue dashed lines). We find a decrease in the fraction of systems with rotational support with redshift, consistent with predictions from lower redshifts, with fractions significantly lower if we consider a more conservative cut of  $v/\sigma_0 > 1 - 3$  (blue shaded regions), with the lower edge at  $v/\sigma_0 > 3$ . This result contrasts the (on-average) constant fractions reported by Ferreira et al. (2023). We compare the fraction of pairs (green line), which we discard from our kinematic analysis, to the one reported in Puskás et al. (2025) (green dashed line), and find broadly consistent results.

### 5.1 The prevalence of disks at $z > 4$

With recent JWST and ALMA observations finding disk-like systems in the early Universe ( $z > 4$ ; e.g., Lelli et al. 2021; Pope et al. 2023; Rowland et al. 2024), questions arise as to how these systems are able to form and stabilize in the turbulent, high-redshift environment. To answer the question of how representative these massive rotating disks are of the high redshift star-forming galaxy population, we investigate the fraction of rotationally supported systems  $v/\sigma_0 > 1$  in our sample and place it in the context of lower redshift measurements (Fig. 12). Without spatially resolved velocity maps (such as those obtained with IFUs), it is difficult to classify systems as disks and to compute a disk fraction. This is highlighted by recent IFU studies at high redshift, which find rotationally supported disks that are heavily perturbed by non-circular motions (Arribas et al. 2024; Übler et al. 2024). This motivates our choice of not defining a disk fraction but instead focusing solely on the evolution of the fraction of rotationally supported systems  $v/\sigma_0 > 1$  across cosmic time. However, we require systems to have kinematic and morphological position angles that are relatively aligned  $|\text{PA}_{\text{kin}} - \text{PA}_{\text{morph}}| < 30^\circ$ . From our original full sample of H $\alpha$  emitters in the FRESCO and CONGRESS surveys, we remove all low S/N galaxies ( $S/N < 10$ ), all galaxies with a position angle too close to the grism dispersion direction, and all

galaxies which are spatially and/or rotationally unresolved. This cut excludes all galaxies that are not in our gold or silver samples (Sec. 2.3). We focus on the stellar mass range  $9 < \log M_\star [M_\odot] < 10$  where our sample is most representative of the star-forming galaxy population (Fig. 2).

We also need to quantify a fraction of merging systems, which cannot be modelled with our single-component approach (see Sec. 3.3). This includes both minor and major mergers, and could include clumpy systems that resemble mergers. We select systems with small separations  $r_{\text{max}} \sim 10$  kpc ( $r \lesssim 1.5''$ ) as mergers, since the single component modelling would not be contaminated by pairs with larger separations. This differs from in-depth studies of merger fractions, which include much larger separations  $r_{\text{max}} \sim 30 - 50$  kpc (Duncan et al. 2019; Duan et al. 2024a; Puskás et al. 2025). In order to consistently measure the pair fraction in our sample, we exclude galaxies which would have not made the cut for kinematic modelling, i.e., galaxies with a low S/N and galaxies with  $|\text{PA}_{\text{morph}}| > 75^\circ$  (Sec. 2.3).

Our results are consistent with an increase of rotationally supported ( $v/\sigma_0 > 1$ ) systems with cosmic time. In our sample, we find that this fraction increases slightly from  $f = 0.36 \pm 0.06$  to  $f = 0.41 \pm 0.06$  from  $z \sim 5.5$  to  $z \sim 4.5$ . This measured increase is consistent with the slow build-up of disks over the  $\approx 600$  Myr probed by

our sample. These fractions drop significantly, to  $f = 0.06 \pm 0.03$  and  $f = 0.15 \pm 0.04$  at  $z \sim 5.5$  and  $z \sim 4.5$ , when considering systems with  $v/\sigma_0 > 3$ . This highlights that although a considerable fraction of the galaxies in our sample are rotationally supported, the majority of these systems are found in the transitional region of  $v/\sigma_0 = 1 - 3$ . These systems could be starting to build rotational support through co-planar accretion of gas, or conversely could have just undergone a merger or radial accretion event, which has disrupted the formation of a rotating disk. Only a small fraction  $f \lesssim 0.1$  of systems has significant rotational support, indicating that disk-like galaxies do not dominate the galaxy population at  $z > 4$  at stellar masses  $9 < \log M_\star [M_\odot] < 10$ , but that dispersion-supported systems are common.

The increase of rotationally supported systems with cosmic time found in this work is consistent with works at lower redshift  $z < 4$  (Simons et al. 2017; Förster Schreiber et al. 2018; Wisnioski et al. 2019). In fact, both Wisnioski et al. (2019) and Simons et al. (2019) find a decrease from  $f \approx 0.8 - 0.9$  at  $z < 1$  to  $f \approx 0.5$  by cosmic noon ( $z \sim 2-3$ ). This is also consistent with Pandya et al. (2024) who classify systems from  $z = 0.5 - 8$  based on their 3D geometry and find an increase of oblate (disky) systems with cosmic time. In their highest redshift bin  $z = 3 - 8$ , they find that the fraction of oblate systems is  $f \sim 0.2 - 0.4$  (depending on the modelling technique chosen) for galaxies with stellar masses  $\log(M_\star [M_\odot]) \sim 9.25-9.75$ .

When compared to the morphological analysis of disk fractions conducted in Ferreira et al. (2022, 2023), we find lower fractions across both redshift bins. However, their work does not apply an upper mass cut-off, as we do here, so this could introduce a bias. More importantly, our fraction of rotationally supported systems is not equivalent to a disk fraction, as shown in part by the significant decrease when considering a higher threshold for rotational support. We also find that only a fraction of  $\sim 0.33$  of our rotationally supported sample has an H $\alpha$  morphology with a Sérsic index  $0.5 < n < 1.5$ , consistent with the exponential profiles we see in local disks. Although systems with  $0.5 < n < 1.5$  represent the peak of the  $n$  distribution, we find a long tail with rotationally supported systems having Sérsic indices  $n \sim 2 - 7$ . The wide range of  $n$  values offers insight into the perturbed morphologies of galaxies at  $z \gtrsim 4$ , making it more difficult to identify rotating disks akin to those seen in the local Universe. This is further supported by the predominantly low values of  $v/\sigma_0$  we find, with  $\approx 65\%$  of the rotationally supported systems having  $v/\sigma_0 < 3$ . These galaxies could drop out of  $v/\sigma_0 > 1$  disk criterion on short timescales if enough momentum is injected in their ISM, for instance through a merger, a starburst, or a disruptive accretion event.

Alongside the fraction of disks, we also plot in Fig. 12 our merger fraction obtained from the visual inspection of images of the galaxies in our sample, and compare it to the major merger pair fractions derived in Puskás et al. (2025) (see also Duan et al. 2024a). We find relatively consistent results, which offers a sanity check for our visual inspection. However, we note that our merger fraction selection differs from that of Puskás et al. (2025). As mentioned above, we probe significantly smaller separations, which can in part explain the lower fractions we find. In terms of merger timescales, which quantify how long galaxies appear as pairs, we find that our separation  $r_{\max} \sim 10$  kpc implies timescales of  $T_{\text{mg}} \sim 0.3 - 0.5$  Gyr for  $\log(M_\star [M_\odot]) = 9 - 10$  at  $z = 5$ , whereas the separation  $r_{\max} \sim 30$  kpc from Puskás et al. (2025) probes timescales of  $T_{\text{mg}} \sim 1.4 - 2.2$  Gyr for the same masses and redshift. These values are derived from a fitting formula based on cosmological dark matter simulations (Huško et al. 2022). Also, Puskás et al. (2025) only select major mergers (mass ratio  $> 1/4$ ), whereas we include systems

with smaller mass ratios as well. We note that our fraction of mergers is low  $f \lesssim 0.15$ , so discarding these systems does not strongly affect our inferred fractions or the main conclusions of this work.

Overall, the strong decrease of the fraction of disk-like systems from  $z < 1$  to  $z = 6$  suggests that the majority of the galaxy population only settles into cold disks during and after cosmic noon, when the bulk of the stellar mass is formed. The fraction of rotationally supported systems increases smoothly from  $z \sim 6$  until the start of cosmic noon  $z \sim 2.5 - 3$ , where this fraction becomes  $f \gtrsim 0.5$ , and disk-like galaxies begin to dominate the galaxy population.

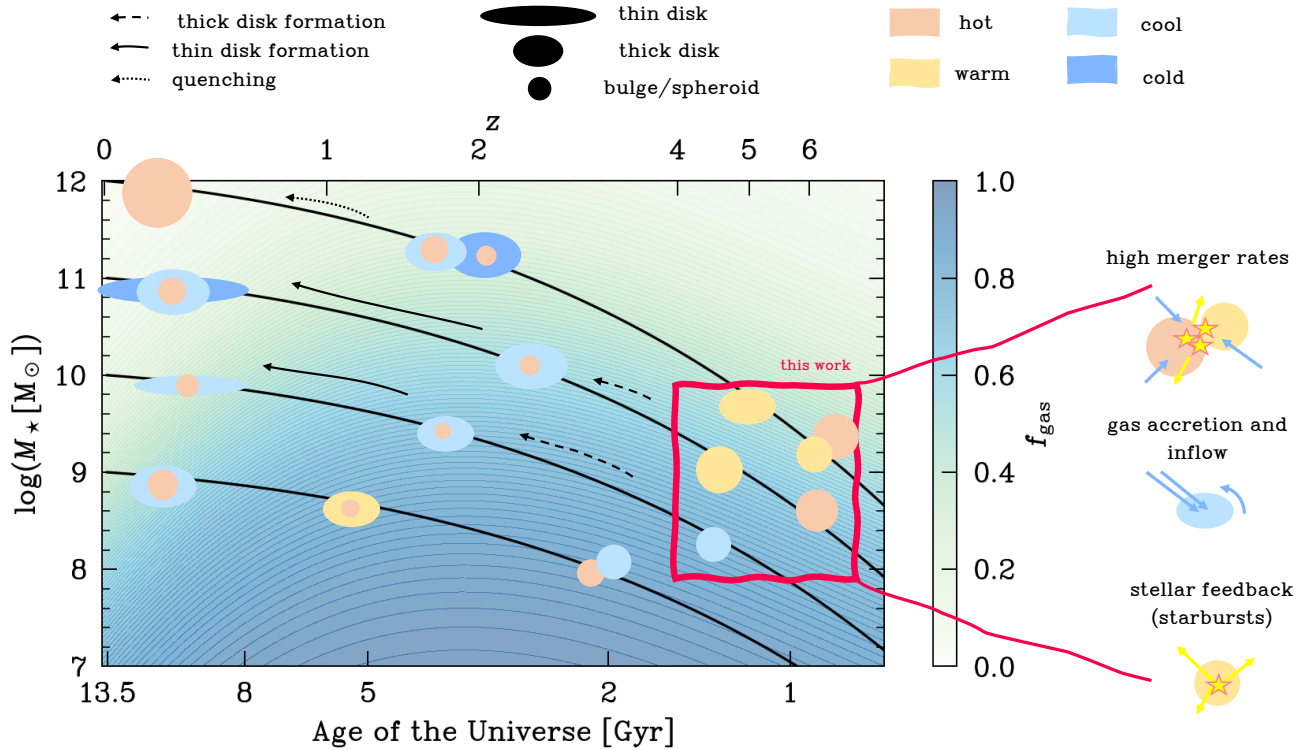
## 5.2 Implications for galaxy evolution across cosmic time

We will now discuss how this work fits into the more global evolution of galaxies and propose explanations for the observed turbulence at high redshift. In Fig. 13, we show a schematic view of our understanding of galaxy evolution from a dynamical point of view, tracing the evolution of local Universe galaxies with  $\log M_\star [M_\odot] = 9, 10, 11$  and 12 back in time by integrating the main sequence from Simmonds et al. (in prep.), which is consistent with predictions from simulations (Tacchella et al. 2016a; McClymont et al. 2025a). We then colour the  $M_\star - z$  plane by gas fraction  $f_{\text{gas}}$  following the relation from Tacconi et al. (2020).

In the local Universe, most star-forming galaxies have settled into disks, which are increasingly thin at higher masses, as highlighted by stellar kinematics (van der Wel et al. 2014; Cappellari 2016). On the higher-mass end, some galaxies have quenched, and their rotational support decreases as they compress and their sizes decrease. At cosmic noon, the star-forming population is predominantly made up of gas-rich thick disks, with the fraction of rotationally supported systems, based on ionised gas measurements, dropping by  $\sim 30\%$  from  $z \sim 0$  for galaxies with stellar masses  $9 < \log M_\star [M_\odot] < 10$  (Fig. 12). As drawn in Fig. 13, these thick disks only settle in dynamically cold disks below  $z \sim 1$ , which also coincides with a decrease in gas fractions to below  $f_{\text{gas}} \lesssim 0.5$ . Because of the dependence of gas fractions on stellar mass, this happens sooner for higher-mass systems, which could promote the formation of thin disks with  $M_\star \sim 10^{11} M_\odot$  at cosmic noon (Wisnioski et al. 2015; Price et al. 2020). However, mass itself is a key factor in disk formation, as more massive galaxies are more stable to gravitational instabilities, especially when the mass profile becomes centrally concentrated (Hopkins et al. 2023). Even at high gas fractions, massive galaxies can settle into disks if the gas accretion is somewhat smooth.

With the arrival of JWST, we are now able to further constrain the kinematics of galaxies beyond  $z \sim 4$  and complement the view of cold gas kinematics from ALMA. The picture that has been constructed in this work, and is supported by other works at high redshift (Parlanti et al. 2023; Arribas et al. 2024), is one of a turbulent epoch of early galaxy formation. Galaxies at masses below  $M_\star \sim 10^{10} M_\odot$  are characterized by high gas fractions  $f_{\text{gas}} \gtrsim 0.7 - 0.8$ , which increase at low masses (Danhaive et al., in prep.). Although the gas fractions are mildly lower at higher masses, it is likely that the highest-mass systems in our sample have recently undergone mergers. In fact, Puskás et al. (2025) shows that merger fractions at  $z \sim 4 - 6$  are high, with 2 - 10 major mergers per Gyr, and it is therefore reasonable to expect that the higher-mass systems were able to form quickly through major or minor mergers. This would justify why we find many dispersion-dominated systems on the massive end, as mergers can increase turbulence in the ISM and also boost star formation through gas inflows.

At lower masses,  $\log M_\star [M_\odot] \lesssim 9.5 - 10$ , galaxies become more unstable to disruptions from gravitational instabilities and star for-



**Figure 13.** Schematic view of the dynamical evolution of galaxies from  $z \sim 8$  to the local Universe, placing the results of our work (red square) in this broader picture. Galaxies are color-coded by dynamical state, from cold ( $v/\sigma_0 \gtrsim 1$ ; blue) to hot ( $v/\sigma_0 \lesssim 1$ ; orange), and shaped according to their thickness/diskiness. We show that as galaxies evolve along the main sequence (black curves), they settle into disk-like systems once they reach small enough gas fractions (inferred by the [Tacconi et al. 2020](#) relation), which depend on both mass and redshift. In the redshift and mass range probed by this work, galaxies are gas-rich and have a turbulent ISM, with high velocity dispersions driven by instabilities caused by mergers, gas inflows, and feedback from star formation.

mation. Specifically, as also discussed in [de Graaff et al. \(2024b\)](#), simulations predict that stellar feedback starts to play an important role in this mass range, with mass loading factors for stellar winds and supernovae reaching values  $\sim 30$  times larger for low-mass ( $\log M_\star [M_\odot] \sim 8$ ) galaxies than for high-mass ( $\log M_\star [M_\odot] \sim 11$ ) galaxies ([Nelson et al. 2019](#)). The shallow potential wells of low mass galaxies, compared to high mass galaxies, promote outflows as they need less energy to be driven out of the galaxy ([Bassini et al. 2023](#)). Recent observational works are consistent with this view, detecting strong outflows in low mass galaxies out to  $z \sim 9$  ([Zhang et al. 2024](#); [Carniani et al. 2024](#)). The shallow potential wells of low mass galaxies also promote inflows of gas that reach the central regions of the galaxy ([Dekel & Burkert 2014](#); [Tacchella et al. 2016b](#); [El-Badry et al. 2016](#); [Hopkins et al. 2023](#); [McClymont et al. 2025a](#)). As the gas compacts, it triggers bursts of star formation, whose strong feedback can expel a lot of the remaining gas. These bursts are hence regulated by inflows and outflows which disrupt disk formation and inject turbulence in the ISM, sustaining high velocity dispersions. Such processes perturb disk formation through misaligned accretion and spin flips ([Dekel et al. 2020](#); [Sales et al. 2012](#)).

Many galaxies in our sample have rotational support  $v/\sigma_0 \sim 2$  akin to massive quiescent galaxies at  $z \sim 1 - 2$  ([Newman et al. 2018](#); [Ji & Giavalisco 2024](#)), found from studies of stellar kinematics, which show slow rotation. This population is distinct from quiescent galaxies which appear to be still sustaining rapid rotation ([D’Eugenio et al. 2024](#)). Some of the galaxies we present here could be progenitors of these slow rotators, without having to undergo much dynamical transformation. However, it is also likely that many of

them will evolve around the main sequence, build up their mass, and build rotational support through accretion of cold gas, becoming the star-forming disks we observe at cosmic noon. Because of the high merger rate at these redshifts, many of these galaxies will undergo numerous major mergers before being able to settle into disks.

Overall, the systems we study in this work are turbulent galaxies in their early stages of formation. Although disk settling is promoted through the smooth accretion of gas with conserved angular momentum, the low masses, high gas fractions, and high merger rates characteristic of the high redshift Universe ( $z > 4$ ) favour bursty and clumpy star formation. Simulations predict that bursty star formation in the early universe hinders disk formation, and the transition from bursty to smooth star formation coincides well with the transition from dispersion-dominated systems to disks ([Hopkins et al. 2023](#); [Semenov et al. 2024b](#)).

### 5.3 Caveats

#### 5.3.1 Modelling and observational biases

In the development of `GEKO`, we have performed recovery tests to understand how robust the constraints are that can be placed on the kinematics in different scenarios, mainly focusing on the orientation of the galaxy with respect to the dispersion direction (position angle), the intrinsic kinematics of the galaxy, and the S/N. The key results from these tests are summarized in the Appendix D, but the full description of the code and the tests will be done in [Danhaive et al. \(in prep\)](#). Specifically, Figs. D1 and D2 highlight the uncertainties in

the velocity dispersion measurement. It is important to note that grism observations inherently provides a weaker constraints on kinematics than IFU observations, which have been used for measurements in the local Universe (e.g., Law et al. 2022), at cosmic noon (e.g., Genzel et al. 2011; Wisnioski et al. 2015; Stott et al. 2016; Förster Schreiber et al. 2018), and out to  $z \approx 11$  with the JWST/NIRSpec IFU (e.g., Marconcini et al. 2024; Scholtz et al. 2024; Venturi et al. 2024). This is firstly due to the line spread function, which in the F444W band is  $R \sim 1600$ , meaning a kinematic resolution of about  $\Delta v \sim 80$  km/s. Even though we are able to constrain the velocity dispersion below  $\Delta v$  in certain favoured scenarios (e.g., high S/N, see Fig. D1), we still suffer from large uncertainties, especially at the low- $\sigma_0$  end, where we can often only place upper limits. Finally, the LSF is calibrated from JWST Cycle 0, 1, and 2 observations, and has an average uncertainty of 10%. We do not marginalize over this uncertainty in the inference framework, which could boost errors by a factor of up to 1.5 (for the lowest values of  $\sigma_0$ ). The boost is minimal for dispersions larger than the LSF. This is particularly important when the velocity dispersion is only measured as an upper limit, since increasing the errors would automatically increase the value of the inferred upper limit.

Our choice of an arctangent velocity curve model instead of other common functions such as the exponential disk model (Freeman 1970; Wisnioski et al. 2011; Genzel et al. 2017) should not strongly affect our measurements since the grism data does not probe the large radii where these curves differ (Price et al. 2020, see also discussion in ). Furthermore, the nature of the grism data is the morphology-kinematics degeneracy along the dispersion direction, which is the entire motivation behind GECO. This means that our constraints are inferred from modelling, which comes with its own assumptions, and are not “directly” measured. Instruments like IFUs benefit from two spatial axes, where grism only has one<sup>8</sup>, which allows them to have better constraints on the spatially resolved kinematics without strong priors on the emission-line maps or dynamical models.

While it is important to keep all of this in mind, the grism remains a crucial tool for studying the statistical properties of high-redshift galaxies. The power of Bayesian inference is in fully tracking uncertainties using the posterior distributions, which allows us to be realistic about the constraints we are making and the conclusions we are drawing for them.

There are additional caveats which we discuss in terms of the biases they could introduce. The first is related to spatial resolution, as it is difficult to distinguish tightly merging galaxies from disks, and the former are hence often misclassified as disks (Simons et al. 2019). This is one of the reasons why strict criteria need to be applied to define disks. It is also important to note that most of the galaxies in our sample are relatively low mass  $M_* < 10^{10} M_\odot$ , and we could be sensitive to non-circular motions. Their low masses and high gas fractions make them much more sensitive to stellar feedback, and combined with their turbulence and low rotational support, it is possible we are probing outflows alongside rotational velocities. This could bias our sample to high  $v/\sigma_0$  at low masses, especially since the low masses systems are typically smaller and have less resolution elements. In general, if the thin-ish disk assumption underlying our models does not hold, it becomes difficult to interpret our measurements, especially the correlations. However, the main conclusion of turbulent ionized gas kinematics at  $z \gtrsim 4$  would still hold, since high

enough rotational support would dominate any contribution from these effects. Overall, caution must be exercised when trying to categorise such systems as disks, even if rotationally-supported, and this is why we do not draw conclusions about the fraction of disks but only that of rotationally-supported systems. This fraction could however be overestimated if the measured velocities do not come from rotation.

In our kinematic modelling, we assume that the velocity dispersion is isotropic and radially constant. However, some spatially resolved studies at lower redshift find a correlation between the local  $\sigma_0$  and the local  $\Sigma_{\text{SFR}}$  (Yu et al. 2019; Law et al. 2022). In cases of clumpy star formation, which are predicted to be more common at higher redshift (Tan et al. 2024; Nakazato et al. 2024), the constant  $\sigma_0$  assumption may not hold as well. However, other works report no correlation in systems with highly star-forming clumps (e.g., Übler et al. 2019). Finally, although many studies show central peaks of velocity dispersion, an intrinsically flat  $\sigma_0$  profile is often recovered when beam smearing effects are accounted for in the kinematic modelling (e.g., De Breuck et al. 2014). A centrally peaked  $\sigma_0$  could bias our measurements to higher values when compare to studies that measure the intrinsic  $\sigma_0$  in the outskirts (e.g., Wisnioski et al. 2015)

Furthermore, our calculation of the rotational velocity is based on inclination corrections to the observed velocity, for which we need to assume an intrinsic thickness of the disk (we assume  $q_0 = 0.2$ ). If the value of  $q_0$  is over (under)-estimated, the inferred dynamical masses could be up to  $\sim 0.02$  dex higher (lower) than the fiducial ones. This does not affect our conclusions, but could help reconcile some of the unphysical measurements in Fig. 7. We also note that the inclination of the galaxy is expected to affect the velocity and velocity dispersion measurements. For  $\sigma_0$ , this is because the line-of-sight dispersion we measure is a mixture of its radial  $\sigma_R$  and vertical  $\sigma_z$  component, and as the galaxy becomes inclined we go from measuring predominantly  $\sigma_z$  in face-on systems to measuring predominantly dispersion  $\sigma_R$  in edge-on systems. Because we expect  $\sigma_z < \sigma_R$  (van der Kruit & Freeman 2011), we could be biased towards higher dispersions at higher inclinations (Leroy et al. 2008; Genzel et al. 2011). We have investigated this and see no trend of  $\sigma_0$  with inclination  $i$ . This is probably due to the limited resolution of our data, as was reported in various studies at cosmic noon (Wisnioski et al. 2015; Übler et al. 2019). Mock observations of simulations can help test these various assumptions (Kohandel et al. 2020; Übler et al. 2021).

### 5.3.2 Uncertainties in the stellar and dynamical masses

In order to estimate the mass content of galaxies, we often need to rely on scaling relations linking photometry and kinematics to the underlying baryons and dark matter, and make assumptions on the galaxy’s shape and size. We will now discuss the choices made in this work and how they affect our results. We infer stellar masses through SED modelling with PROSPECTOR, a method with many advantages but also many degeneracies. We attempt to break some of the degeneracies by fixing the redshift to the grism spectroscopic redshift, and by simultaneously fitting the photometry with the line fluxes of the available emission lines (see 3.1). Although we are not fitting spectra and only have access to some of the brighter emission lines, PROSPECTOR has been shown to successfully recover emission line fluxes, when compared to NIRCcam grism data, even when fitting with photometry only (Simmonds et al., in prep.). Furthermore, our S/N cut implies selecting higher equivalent width galaxies, meaning galaxies whose young stellar population and nebular emission is dominating the SEDs (Boyet et al. 2024; Endsley et al. 2024). This can make it difficult to detect the underlying population of older stars,

<sup>8</sup> If both grism R and C are available (e.g. SAPPHIRES; Sun et al. 2025a, and see an example therein) or if observations are taken with varying PAs (e.g. ALT; Naidu et al. 2024), more spatial information can be obtained.

and hence to constrain the full SFH. This effect is called “outshining” and can cause an underestimate of the stellar masses, effectively only attributing the stellar mass to the more visible young stellar population (Tacchella et al. 2022; Papovich et al. 2023; Tacchella et al. 2023; Whitler et al. 2023).

Moving to the dynamical masses, the circular velocities needed to compute them are inferred assuming a virialised rotating disk with an exponential light profile. For galaxies with larger Sérsic indices, this assumption can lead to biased results. Furthermore, for pressure-dominated systems, the choice of the pressure support term multiplying the  $\sigma_0$  in Eq. 6 can lead to over- or under-estimations of the circular velocity (see Price et al. 2022, for detailed analysis). Also, any uncertainties (and caveats) from the kinematic modelling (Sec. 5.3.1) are propagated to the dynamical masses through the circular velocity. Finally, due to the increased merger rates at high redshift, it is possible we are probing velocity offsets between two systems or velocity gradients induced by the gravitational interaction in a pre- or post-merger phase (see de Graaff et al. 2024a, for an in-depth discussion).

### 5.3.3 The impact of dust on kinematics

An important caveat in this work is that we do not directly measure dust attenuation. Although the early Universe was initially believed to be essentially dust free, recent works have revealed a rapid build-up of dust with detections out to  $z \sim 7$  with both JWST and ALMA (Pallottini & Ferrara 2023; Witstok et al. 2023; Sawant et al. 2025), although these galaxies are typically more massive than the galaxies probed in this work. Furthermore, numerous works have indicated that a significant fraction of the star formation activity in the early Universe is actually occurring in dusty galaxies (Laporte et al. 2017; Sugahara et al. 2021; Inami et al. 2022), with Algera et al. (2023) finding a  $\sim 30\%$  contribution at  $z \sim 7$  and  $\sim 66\%$  contribution at  $z \sim 5$  (Sun et al. 2025b). Still, other works find results consistent with a low dust content at high redshift (Sandles et al. 2024).

In our sample, we infer dust attenuation using SED modelling with PROSPECTOR. Because of the inherent degeneracies in SED fitting, this could bias the SFRs we infer. Our fits show that the amount of dust attenuation increases with stellar mass, and that the relation between S/N and stellar mass has a large scatter, meaning that there are numerous massive galaxies, which also have higher dust content, with low S/N  $H\alpha$  detections. This can however also be caused by low SFRs. An example of such a galaxy is the well-known HST dark galaxy HDF850.1 (Sun et al. 2024; Herard-Demanche et al. 2025), where the  $H\alpha$  from the main component is heavily ( $>99\%$ ) dust-obscured. Because we are studying the kinematics of ionised gas through  $H\alpha$ , we may be missing galaxies on the massive end due to their high dust content, and this could bias our correlations. However, studies at lower redshift suffer from the same biases, so our comparisons should be self-consistent.

## 6 SUMMARY & CONCLUSIONS

In this work, we focus on a sample of 272  $H\alpha$  emitters in GOODS-S and GOODS-N at redshift  $z \approx 3.9 - 6.5$  detected using JWST NIRCcam slitless spectroscopy from the FRESCO and CONGRESS surveys. We select galaxies with high S/N (integrated S/N  $> 10$ ) and a large enough PA offset from the dispersion direction ( $|PA_{\text{morph}}| < 75^\circ$ ) in order to study their ionised gas kinematics and the properties of their stellar populations. Our final sample probes two orders of magnitude in stellar mass ( $M_\star \approx 10^{8-10} M_\odot$ ) and star formation

rate ( $\text{SFR}_{10} \approx 0.3 - 100 M_\odot/\text{yr}$ ), and representative of the galaxy population down to  $M_\star \approx 10^9 M_\odot$ .

We use the SED-inference tool PROSPECTOR, with the redshift and  $H\alpha$  emission line fluxes obtained from the grism observations and photometry from JADES, to infer SFRs and stellar masses for our galaxies. We use a novel grism forward-modelling tool GEKO to infer the  $H\alpha$  morphology and kinematics and measure rotational velocities, velocity dispersions, and dynamical masses. We use morphological priors from NIRCcam imaging from the JADES survey to alleviate the morphology-kinematics degeneracy of the grism data. This method fully forward models the instrument, accounting for LSF, PSF, and pixelisation.

We summarize our key results below:

- The star-forming galaxies in our sample at  $z \approx 3.9 - 6.5$  are characterized by a highly turbulent ISM, with median ionised gas velocity dispersions of  $\sigma_0 \approx 100$  km/s, but also a large scatter with velocity dispersions ranging from  $\sigma_0 = 30 - 200$  km/s. These systems also have an average rotational support  $v/\sigma_0 \approx 2$ , with  $> 50\%$  of the galaxies being dispersion dominated ( $v/\sigma_0 < 1$ ). Comparing to measurements at lower redshifts ( $z < 4$ ), we find that the  $\sigma_0$  ( $v/\sigma_0$ ) increases (decreases) with redshift, broadly consistent with predictions from the Toomre model for marginal disks and from cosmological simulations.

- We analyse the correlations between  $v/\sigma_0$  and  $\sigma_0$  with  $M_\star$ , SFR, sSFR, and SFR surface density, and find that the strongest correlations are between  $\sigma_0$  and SFR ( $\rho = 0.40$ ,  $p < 0.001$ ) and  $\sigma_0$  and SFR surface density ( $\rho = 0.38$ ,  $p = 0.001$ ). This is consistent with gravitational instabilities and feedback from star formation which perturb the build-up of rotational support and inject energy into the ISM. Although it is difficult to distinguish between these two main sources of turbulence, we find no strong evidence for a dominant role of feedback-driven turbulence. The  $\sigma_0$ -SFR correlation is in agreement with results from the literature at  $z < 4$ , albeit with an offset towards higher  $\sigma_0$ . In comparison to works at lower redshifts, we find that the relations show more scatter and weaker correlations on average, which we attribute to the large diversity of the galaxy population.

- We find a weak, decreasing trend of  $v/\sigma_0$  with  $\log M_\star$ , which is likely driven by observational biases at the low-mass end. However, a flattening of the  $v/\sigma_0$ - $\log M_\star$  relation below  $M_\star \sim 10^{10} M_\odot$  is not in tension with results from studies at  $z < 4$  and is predicted by the marginal disk framework.

- The fraction of rotationally-supported ( $v/\sigma_0 > 1$ ) systems in our sample increases with cosmic time, from  $f = 0.36 \pm 0.06$  to  $f = 0.41 \pm 0.06$  from  $z \sim 5.5$  to  $z \sim 4.5$  for galaxies with stellar masses  $9 < \log M_\star [M_\odot] < 10$ . This increase is consistent with trends from  $z < 4$ , which suggest that stable cold disks only form below  $z < 1$ , with a smooth increase of rotational support with cosmic time.

Overall, our work describes a turbulent phase in the evolution of galaxies in the early Universe. This epoch constitutes the dawn of disks, where galaxies start to be sustained by rotation but will go through several episodes of instability, caused by internal (feedback, radial inflows, bursty star formation) and external effects (non-smooth accretion, mergers), before settling into the cold disks we observe in the local Universe.

Our work has demonstrated that grism data is a powerful tool for population analyses of galaxy kinematics at high redshifts. Using this dataset in harmony with a novel Bayesian inference forward-modelling tool, we were able to paint the first statistically significant picture of ionised gas kinematics at  $z > 4$  on a large sample of



galaxies. It however remains important to complement our work and future grism kinematics works with high-redshift multi-wavelength interferometric and IFU observations from ALMA and NIRSPEC IFU to study the complete 2D kinematics structure in more detail and place stronger constraints on the formation of stable disks in the early Universe.

## ACKNOWLEDGEMENTS

We thank Emily Wisnioski and Trevor Mendel for the insightful discussions. ALD thanks the University of Cambridge Harding Distinguished Postgraduate Scholars Programme and Technology Facilities Council (STFC) Center for Doctoral Training (CDT) in Data intensive science at the University of Cambridge (STFC grant number 2742605) for a PhD studentship. ALD and ST acknowledge support by the Royal Society Research Grant G125142. HÜ acknowledges funding by the European Union (ERC APEX, 101164796). Views and opinions expressed are however those of the authors only and do not necessarily reflect those of the European Union or the European Research Council Executive Agency. Neither the European Union nor the granting authority can be held responsible for them. EE, FS, ZJ, MR, and CNAW acknowledge support from the JWST/NIRCam contract to the University of Arizona NAS5-02015. SA acknowledges grant PID2021-127718NB-I00 funded by the Spanish Ministry of Science and Innovation/State Agency of Research (MICIN/AEI/ 10.13039/501100011033). AJB acknowledges funding from the "FirstGalaxies" Advanced Grant from the European Research Council (ERC) under the European Union's Horizon 2020 research and innovation programme (Grant agreement No. 789056). SC acknowledges support by European Union's HE ERC Starting Grant No. 101040227 - WINGS. GCJ acknowledges support by the Science and Technology Facilities Council (STFC), ERC Advanced Grant 695671 "QUENCH". RM, CS, and JS acknowledge support by the Science and Technology Facilities Council (STFC), and by the ERC through Advanced Grant 695671 "QUENCH". RM and CS are also supported by the UKRI Frontier Research grant RISEandFALL. RM also acknowledges funding from a research professorship from the Royal Society. WM thanks the Science and Technology Facilities Council (STFC) Center for Doctoral Training (CDT) in Data Intensive Science at the University of Cambridge (STFC grant number 2742968) for a PhD studentship. NCV acknowledges support from the Charles and Julia Henry Fund through the Henry Fellowship. WMB gratefully acknowledges support from DARK via the DARK fellowship. This work was supported by a research grant (VIL54489) from VILLUM FONDEN. DJE is supported as a Simons Investigator and by JWST/NIRCam contract to the University of Arizona, NAS5-02015. DP acknowledges support by the Huo Family Foundation through a P.C. Ho PhD Studentship. BER acknowledges support from the NIRCam Science Team contract to the University of Arizona, NAS5-02015, and JWST Program 3215. The research of CCW is supported by NOIRLab, which is managed by the Association of Universities for Research in Astronomy (AURA) under a cooperative agreement with the National Science Foundation.

This work is based on observations made with the NASA/ESA Hubble Space Telescope and NASA/ESA/CSA James Webb Space Telescope. The data were obtained from the Mikulski Archive for Space Telescopes at the Space Telescope Science Institute, which is operated by the Association of Universities for Research in Astronomy, Inc., under NASA contract NAS 5-03127 for JWST. These observations are associated with program #1180, 1181, 1210 (JADES), #1895 (FRESCO), # 1963 (JEMS) and #3577 (CONGRESS). Sup-

port for program #3577 was provided by NASA through a grant from the Space Telescope Science Institute, which is operated by the Association of Universities for Research in Astronomy, Inc., under NASA contract NAS 5-03127. The authors acknowledge the FRESCO team for developing their observing program with a zero-exclusive-access period. The authors acknowledge use of the lux supercomputer at UC Santa Cruz, funded by NSF MRI grant AST 1828315.

## REFERENCES

- Algera H. S. B., et al., 2023, *MNRAS*, **518**, 6142  
 Allen J. T., et al., 2015, *MNRAS*, **446**, 1567  
 Allen N., et al., 2024, *arXiv e-prints*, p. [arXiv:2410.16354](https://arxiv.org/abs/2410.16354)  
 Arribas S., Colina L., Bellocchi E., Maiolino R., Villar-Martín M., 2014, *A&A*, **568**, A14  
 Arribas S., et al., 2024, *A&A*, **688**, A146  
 Bacon R., et al., 2010, in McLean I. S., Ramsay S. K., Takami H., eds, *Society of Photo-Optical Instrumentation Engineers (SPIE) Conference Series Vol. 7735, Ground-based and Airborne Instrumentation for Astronomy III*, p. 773508 ([arXiv:2211.16795](https://arxiv.org/abs/2211.16795)), doi:[10.1117/12.856027](https://doi.org/10.1117/12.856027)  
 Baker W. M., et al., 2025a, *arXiv e-prints*, p. [arXiv:2501.09070](https://arxiv.org/abs/2501.09070)  
 Baker W. M., et al., 2025b, *Nature Astronomy*, **9**, 141  
 Barišić I., et al., 2024, *arXiv e-prints*, p. [arXiv:2408.08350](https://arxiv.org/abs/2408.08350)  
 Bassini L., Feldmann R., Gensior J., Hayward C. C., Faucher-Giguère C.-A., Cenci E., Liang L., Bernardini M., 2023, *MNRAS*, **525**, 5388  
 Bezanson R., et al., 2018, *ApJ*, **858**, 60  
 Boardman N., Wild V., Heckman T., Sanchez S. F., Riffel R., Riffel R. A., Zasowski G., 2023, *MNRAS*, **520**, 4301  
 Bolatto A. D., et al., 2017, *ApJ*, **846**, 159  
 Bouché N. F., et al., 2022, *A&A*, **658**, A76  
 Bournaud F., Elmegreen B. G., Elmegreen D. M., 2007, *ApJ*, **670**, 237  
 Boyett K., et al., 2024, *MNRAS*, **535**, 1796  
 Brammer G. B., van Dokkum P. G., Coppi P., 2008, *ApJ*, **686**, 1503  
 Brook C. B., Stinson G., Gibson B. K., Roškar R., Wadsley J., Quinn T., 2012, *MNRAS*, **419**, 771  
 Bundy K., et al., 2015, *ApJ*, **798**, 7  
 Bunker A. J., NIRSPEC Instrument Science Team JAESs Collaboration 2020, in da Cunha E., Hodge J., Afonso J., Pentericci L., Sobral D., eds, *IAU Symposium Vol. 352, Uncovering Early Galaxy Evolution in the ALMA and JWST Era*, pp 342–346 ([arXiv:2112.15207](https://arxiv.org/abs/2112.15207)), doi:[10.1017/S1743921319009463](https://doi.org/10.1017/S1743921319009463)  
 Burkert A., et al., 2010, *ApJ*, **725**, 2324  
 Byler N., Dalcanton J. J., Conroy C., Johnson B. D., 2017, *ApJ*, **840**, 44  
 Calzetti D., Armus L., Bohlin R. C., Kinney A. L., Koornneef J., Storchi-Bergmann T., 2000, *ApJ*, **533**, 682  
 Cappellari M., 2016, *ARA&A*, **54**, 597  
 Cappellari M., et al., 2007, *MNRAS*, **379**, 418  
 Cappellari M., et al., 2011, *MNRAS*, **416**, 1680  
 Carniani S., et al., 2024, *A&A*, **685**, A99  
 Cattaneo A., et al., 2009, *Nature*, **460**, 213  
 Charlot S., Fall S. M., 2000, *ApJ*, **539**, 718  
 Ciotti L., Bertin G., 1999, *A&A*, **352**, 447  
 Conroy C., Gunn J. E., White M., 2009, *ApJ*, **699**, 486  
 Courteau S., 1997, *AJ*, **114**, 2402  
 Croom S. M., et al., 2012, *MNRAS*, **421**, 872  
 D'Eugenio F., et al., 2024, *Nature Astronomy*, **8**, 1443  
 De Breuck C., et al., 2014, *A&A*, **565**, A59  
 Dekel A., Burkert A., 2014, *MNRAS*, **438**, 1870  
 Dekel A., et al., 2009, *Nature*, **457**, 451  
 Dekel A., Ginzburg O., Jiang F., Freundlich J., Lapiner S., Ceverino D., Primack J., 2020, *MNRAS*, **493**, 4126  
 Della Bruna L., et al., 2020, *A&A*, **635**, A134  
 Dib S., Bell E., Burkert A., 2006, *ApJ*, **638**, 797  
 Dickinson M., et al., 2004, *ApJ*, **600**, L99  
 Duan Q., et al., 2024a, *arXiv e-prints*, p. [arXiv:2407.09472](https://arxiv.org/abs/2407.09472)  
 Duan Q., et al., 2024b, *arXiv e-prints*, p. [arXiv:2411.04944](https://arxiv.org/abs/2411.04944)

- Dubois Y., Peirani S., Pichon C., Devriendt J., Gavazzi R., Welker C., Volonteri M., 2016, *MNRAS*, **463**, 3948
- Duncan K., et al., 2019, *ApJ*, **876**, 110
- Eisenstein D. J., et al., 2023, *arXiv e-prints*, p. [arXiv:2306.02465](https://arxiv.org/abs/2306.02465)
- Ejdetjärn T., Agertz O., Östlin G., Rey M. P., Renaud F., 2024, *MNRAS*, **534**, 135
- El-Badry K., Wetzel A., Geha M., Hopkins P. F., Kereš D., Chan T. K., Faucher-Giguère C.-A., 2016, *ApJ*, **820**, 131
- El-Badry K., et al., 2018, *MNRAS*, **473**, 1930
- Emsellem E., et al., 2007, *MNRAS*, **379**, 401
- Endsley R., et al., 2024, *MNRAS*, **533**, 1111
- Epinat B., Amram P., Marcelin M., 2008, *MNRAS*, **390**, 466
- Epinat B., Amram P., Balkowski C., Marcelin M., 2010, *MNRAS*, **401**, 2113
- Fall S. M., Efstathiou G., 1980, *MNRAS*, **193**, 189
- Feng Y., Di Matteo T., Croft R., Tenneti A., Bird S., Battaglia N., Wilkins S., 2015, *ApJ*, **808**, L17
- Ferreira L., et al., 2022, *ApJ*, **938**, L2
- Ferreira L., et al., 2023, *ApJ*, **955**, 94
- Florian J., Ziegler B., Hirschmann M., Papaderos P., Choi E., Frigo M., Gomes J.-M., Somerville R. S., 2020, *A&A*, **635**, A41
- Forbes J. C., et al., 2023, *ApJ*, **948**, 107
- Förster Schreiber N. M., Wuyts S., 2020, *ARA&A*, **58**, 661
- Förster Schreiber N. M., et al., 2006, *The Messenger*, **125**, 11
- Förster Schreiber N. M., et al., 2009, *ApJ*, **706**, 1364
- Förster Schreiber N. M., et al., 2018, *ApJS*, **238**, 21
- Freeman K. C., 1970, *ApJ*, **160**, 811
- Gabor J. M., Bournaud F., 2014, *MNRAS*, **437**, L56
- Gatto A., et al., 2015, *MNRAS*, **449**, 1057
- Genzel R., et al., 2008, *ApJ*, **687**, 59
- Genzel R., et al., 2011, *ApJ*, **733**, 101
- Genzel R., et al., 2017, *Nature*, **543**, 397
- Genzel R., et al., 2020, *ApJ*, **902**, 98
- Giavalisco M., et al., 2004, *ApJ*, **600**, L93
- Glazebrook K., 2013, *Publ. Astron. Soc. Australia*, **30**, e056
- Graham A. W., Driver S. P., 2005, *Publ. Astron. Soc. Australia*, **22**, 118
- Green A. W., et al., 2014, *MNRAS*, **437**, 1070
- Green A. W., et al., 2018, *MNRAS*, **475**, 716
- Greene T. P., et al., 2017, *Journal of Astronomical Telescopes, Instruments, and Systems*, **3**, 035001
- Hainline K. N., et al., 2024, *ApJ*, **964**, 71
- Harrison C. M., 2017, *Nature Astronomy*, **1**, 0165
- Harvey T., et al., 2025, *ApJ*, **978**, 89
- Hasheminia M., Mosleh M., Hosseini-ShahiSavandi S. Z., Tacchella S., 2024, *ApJ*, **975**, 252
- Helton J. M., et al., 2024a, *ApJ*, **962**, 124
- Helton J. M., et al., 2024b, *ApJ*, **974**, 41
- Herard-Demanche T., et al., 2025, *MNRAS*, **537**, 788
- Hoffman M. D., Gelman A., 2011, *arXiv e-prints*, p. [arXiv:1111.4246](https://arxiv.org/abs/1111.4246)
- Hopkins P. F., Quataert E., Murray N., 2011, *MNRAS*, **417**, 950
- Hopkins P. F., et al., 2023, *MNRAS*, **525**, 2241
- Hubble E. P., 1926, *ApJ*, **64**, 321
- Huško F., Lacey C. G., Baugh C. M., 2022, *MNRAS*, **509**, 5918
- Inami H., et al., 2022, *MNRAS*, **515**, 3126
- Inoue A. K., 2011, *Earth, Planets and Space*, **63**, 1027
- Jain S., Tacchella S., Mosleh M., 2024, *The Open Journal of Astrophysics*, **7**, 113
- Ji Z., Giavalisco M., 2023, *ApJ*, **943**, 54
- Ji Z., Giavalisco M., 2024, *arXiv e-prints*, p. [arXiv:2410.00099](https://arxiv.org/abs/2410.00099)
- Ji Z., et al., 2024, *arXiv e-prints*, p. [arXiv:2401.00934](https://arxiv.org/abs/2401.00934)
- Johnson H. L., et al., 2018, *MNRAS*, **474**, 5076
- Johnson B. D., Leja J., Conroy C., Speagle J. S., 2021, *ApJS*, **254**, 22
- Jones O. C., et al., 2023, *MNRAS*, **523**, 2519
- Jones G. C., et al., 2024, *A&A*, **682**, A122
- Ju M., et al., 2025, *ApJ*, **978**, L39
- Kannan R., et al., 2025, *arXiv e-prints*, p. [arXiv:2502.20437](https://arxiv.org/abs/2502.20437)
- Kashino D., Lilly S. J., Matthee J., Eilers A.-C., Mackenzie R., Bordoloi R., Simcoe R. A., 2023, *ApJ*, **950**, 66
- Klessen R. S., Hennebelle P., 2010, *A&A*, **520**, A17
- Kohandel M., Pallottini A., Ferrara A., Carniani S., Gallerani S., Vallini L., Zanella A., Behrens C., 2020, *MNRAS*, **499**, 1250
- Kohandel M., Pallottini A., Ferrara A., Zanella A., Rizzo F., Carniani S., 2024, *A&A*, **685**, A72
- Kormendy J., Ho L. C., 2013, *ARA&A*, **51**, 511
- Kormendy J., Kennicutt Jr. R. C., 2004, *ARA&A*, **42**, 603
- Krajnović D., et al., 2011, *MNRAS*, **414**, 2923
- Kretschmer M., Agertz O., Teyssier R., 2020, *MNRAS*, **497**, 4346
- Kretschmer M., Dekel A., Teyssier R., 2022, *MNRAS*, **510**, 3266
- Kriek M., Conroy C., 2013, *ApJ*, **775**, L16
- Krumholz M. R., Burkhard B., 2016, *MNRAS*, **458**, 1671
- Krumholz M. R., Burkhard B., Forbes J. C., Crocker R. M., 2018, *MNRAS*, **477**, 2716
- Lapiner S., et al., 2023, *MNRAS*, **522**, 4515
- Laporte N., et al., 2017, *ApJ*, **837**, L21
- Law D. R., et al., 2022, *ApJ*, **928**, 58
- Le Bail A., et al., 2024, *A&A*, **688**, A53
- Leja J., Carnall A. C., Johnson B. D., Conroy C., Speagle J. S., 2019, *ApJ*, **876**, 3
- Lelli F., Di Teodoro E. M., Fraternali F., Man A. W. S., Zhang Z.-Y., De Breuck C., Davis T. A., Maiolino R., 2021, *Science*, **371**, 713
- Leroy A. K., Walter F., Brinks E., Bigiel F., de Blok W. J. G., Madore B., Thornley M. D., 2008, *AJ*, **136**, 2782
- Leroy A. K., et al., 2009, *AJ*, **137**, 4670
- Li Z., et al., 2023, *arXiv e-prints*, p. [arXiv:2310.09327](https://arxiv.org/abs/2310.09327)
- Li J., et al., 2024, *ApJ*, **976**, 70
- Lilly S. J., Carollo C. M., Pipino A., Renzini A., Peng Y., 2013, *ApJ*, **772**, 119
- Looser T. J., et al., 2024, *Nature*, **629**, 53
- Madau P., Dickinson M., 2014, *ARA&A*, **52**, 415
- Mandelker N., Dekel A., Ceverino D., DeGraf C., Guo Y., Primack J., 2017, *MNRAS*, **464**, 635
- Mannucci F., Cresci G., Maiolino R., Marconi A., Gnerucci A., 2010, *MNRAS*, **408**, 2115
- Marconcin C., et al., 2024, *MNRAS*, **533**, 2488
- Marshall M. A., Wilkins S., Di Matteo T., Roper W. J., Vijayan A. P., Ni Y., Feng Y., Croft R. A. C., 2022, *MNRAS*, **511**, 5475
- Matharu J., et al., 2023, *ApJ*, **949**, L11
- Matharu J., et al., 2024, *arXiv e-prints*, p. [arXiv:2404.17629](https://arxiv.org/abs/2404.17629)
- Matthee J., et al., 2024, *ApJ*, **963**, 129
- McClymont W., et al., 2025a, *arXiv e-prints*, p. [arXiv:2503.00106](https://arxiv.org/abs/2503.00106)
- McClymont W., et al., 2025b, *arXiv e-prints*, p. [arXiv:2503.04894](https://arxiv.org/abs/2503.04894)
- Miller S. H., Bundy K., Sullivan M., Ellis R. S., Treu T., 2011, *ApJ*, **741**, 115
- Mo H. J., Mao S., White S. D. M., 1998, *MNRAS*, **295**, 319
- Mosleh M., Hosseinnejad S., Hosseini-ShahiSavandi S. Z., Tacchella S., 2020, *ApJ*, **905**, 170
- Muñoz-Mateos J. C., Gil de Paz A., Boissier S., Zamorano J., Jarrett T., Gallego J., Madore B. F., 2007, *ApJ*, **658**, 1006
- Naab T., et al., 2014, *MNRAS*, **444**, 3357
- Naidu R. P., et al., 2024, *arXiv e-prints*, p. [arXiv:2410.01874](https://arxiv.org/abs/2410.01874)
- Nakazato Y., Ceverino D., Yoshida N., 2024, *ApJ*, **975**, 238
- Neeleman M., Prochaska J. X., Kanekar N., Rafelski M., 2020, *Nature*, **581**, 269
- Nelson E. J., et al., 2016, *ApJ*, **828**, 27
- Nelson D., et al., 2019, *MNRAS*, **490**, 3234
- Nelson E. J., et al., 2023, *ApJ*, **948**, L18
- Nelson E., et al., 2024, *ApJ*, **976**, L27
- Nestor Shachar A., et al., 2023, *ApJ*, **944**, 78
- Newman S. F., et al., 2012, *ApJ*, **761**, 43
- Newman S. F., et al., 2013, *ApJ*, **767**, 104
- Newman A. B., Belli S., Ellis R. S., 2015, *ApJ*, **813**, L7
- Newman A. B., Belli S., Ellis R. S., Patel S. G., 2018, *ApJ*, **862**, 126
- Oesch P. A., et al., 2023, *MNRAS*, **525**, 2864
- Oklopčić A., Hopkins P. F., Feldmann R., Kereš D., Faucher-Giguère C.-A., Murray N., 2017, *MNRAS*, **465**, 952
- Oppenheimer B. D., Davé R., 2008, *MNRAS*, **387**, 577
- Oppenheimer B. D., Davé R., Kereš D., Fardal M., Katz N., Kollmeier J. A., Weinberg D. H., 2010, *MNRAS*, **406**, 2325

- Ostriker E. C., Shetty R., 2011, *ApJ*, 731, 41
- Pallottini A., Ferrara A., 2023, *A&A*, 677, L4
- Pandya V., et al., 2024, *ApJ*, 963, 54
- Papovich C., et al., 2023, *ApJ*, 949, L18
- Parlanti E., Carniani S., Pallottini A., Cignoni M., Cresci G., Kohandel M., Mannucci F., Marconi A., 2023, *A&A*, 673, A153
- Parlanti E., et al., 2024, *A&A*, 684, A24
- Pasha I., Miller T. B., 2023, *The Journal of Open Source Software*, 8, 5703
- Pelliccia D., et al., 2020, *ApJ*, 896, L26
- Phan D., Pradhan N., Jankowiak M., 2019, *arXiv e-prints*, p. [arXiv:1912.11554](https://arxiv.org/abs/1912.11554)
- Pillepich A., et al., 2019, *MNRAS*, 490, 3196
- Planck Collaboration et al., 2020, *A&A*, 641, A6
- Pope A., et al., 2023, *ApJ*, 951, L46
- Price S. H., et al., 2016, *ApJ*, 819, 80
- Price S. H., et al., 2020, *ApJ*, 894, 91
- Price S. H., et al., 2022, *A&A*, 665, A159
- Puskás D., et al., 2025, *arXiv e-prints*, p. [arXiv:2502.01721](https://arxiv.org/abs/2502.01721)
- Qu Y., Di Matteo P., Lehnert M., van Driel W., Jog C. J., 2010, *A&A*, 515, A11
- Rathjen T.-E., Naab T., Walch S., Seifried D., Girichidis P., Wünsch R., 2023, *MNRAS*, 522, 1843
- Reines A. E., Volonteri M., 2015, *ApJ*, 813, 82
- Rieke M., 2020, in da Cunha E., Hodge J., Afonso J., Pentericci L., Sobral D., eds, *IAU Symposium Vol. 352, Uncovering Early Galaxy Evolution in the ALMA and JWST Era*. pp 337–341, [doi:10.1017/S1743921319008950](https://doi.org/10.1017/S1743921319008950)
- Rieke M. J., et al., 2023, *ApJS*, 269, 16
- Rigamonti F., Cortese L., Bollati F., Covino S., Dotti M., Fraser-McKelvie A., Haardt F., 2024, *A&A*, 686, A98
- Rizzo F., Vegetti S., Powell D., Fraternali F., McKean J. P., Stacey H. R., White S. D. M., 2020, *Nature*, 584, 201
- Rizzo F., et al., 2024, *A&A*, 689, A273
- Robertson B. E., et al., 2023, *ApJ*, 942, L42
- Robertson B., et al., 2024, *ApJ*, 970, 31
- Rowland L. E., et al., 2024, *MNRAS*, 535, 2068
- Saldana-Lopez A., et al., 2025, *arXiv e-prints*, p. [arXiv:2501.17145](https://arxiv.org/abs/2501.17145)
- Sales L. V., Navarro J. F., Theuns T., Schaye J., White S. D. M., Frenk C. S., Crain R. A., Dalla Vecchia C., 2012, *MNRAS*, 423, 1544
- Sandles L., et al., 2024, *A&A*, 691, A305
- Sawant P., et al., 2025, *A&A*, 694, A82
- Schneider R., Maiolino R., 2024, *A&ARv*, 32, 2
- Scholtz J., et al., 2024, *A&A*, 687, A283
- Semenov V. A., Conroy C., Smith A., Puchwein E., Hernquist L., 2024a, *arXiv e-prints*, p. [arXiv:2409.18173](https://arxiv.org/abs/2409.18173)
- Semenov V. A., Conroy C., Hernquist L., 2024b, *arXiv e-prints*, p. [arXiv:2410.09205](https://arxiv.org/abs/2410.09205)
- Semenov V. A., Conroy C., Chandra V., Hernquist L., Nelson D., 2024c, *ApJ*, 972, 73
- Sersic J. L., 1968, *Atlas de Galaxias Australes*
- Sharda P., Krumholz M. R., Wisnioski E., Forbes J. C., Federrath C., Acharyya A., 2021, *MNRAS*, 502, 5935
- Sharma G., Upadhyaya V., Salucci P., Desai S., 2024, *A&A*, 689, A318
- Shetty R., Ostriker E. C., 2012, *ApJ*, 754, 2
- Shuntov M., et al., 2025, *A&A*, 695, A20
- Silk J., Rees M. J., 1998, *A&A*, 331, L1
- Simard L., Mendel J. T., Patton D. R., Ellison S. L., McConnachie A. W., 2011, *ApJS*, 196, 11
- Simmonds C., et al., 2024, *MNRAS*, 535, 2998
- Simons R. C., et al., 2016, *ApJ*, 830, 14
- Simons R. C., et al., 2017, *ApJ*, 843, 46
- Simons R. C., et al., 2019, *ApJ*, 874, 59
- Simons R. C., et al., 2021, *ApJ*, 923, 203
- Stott J. P., et al., 2016, *MNRAS*, 457, 1888
- Sugahara Y., et al., 2021, *ApJ*, 923, 5
- Sun F., et al., 2022, *ApJ*, 936, L8
- Sun F., et al., 2023a, *ApJ*, 953, 53
- Sun G., Faucher-Giguère C.-A., Hayward C. C., Shen X., Wetzel A., Cochrane R. K., 2023b, *ApJ*, 955, L35
- Sun F., et al., 2024, *ApJ*, 961, 69
- Sun F., et al., 2025a, *arXiv e-prints*, p. [arXiv:2503.15587](https://arxiv.org/abs/2503.15587)
- Sun F., et al., 2025b, *ApJ*, 980, 12
- Swinbank A. M., et al., 2011, *ApJ*, 742, 11
- Swinbank A. M., et al., 2017, *MNRAS*, 467, 3140
- Tacchella S., et al., 2015, *Science*, 348, 314
- Tacchella S., Dekel A., Carollo C. M., Ceverino D., DeGraf C., Lapiner S., Mandelker N., Primack Joel R., 2016a, *MNRAS*, 457, 2790
- Tacchella S., Dekel A., Carollo C. M., Ceverino D., DeGraf C., Lapiner S., Mandelker N., Primack J. R., 2016b, *MNRAS*, 458, 242
- Tacchella S., et al., 2019, *MNRAS*, 487, 5416
- Tacchella S., Forbes J. C., Caplar N., 2020, *MNRAS*, 497, 698
- Tacchella S., et al., 2022, *ApJ*, 927, 170
- Tacchella S., et al., 2023, *MNRAS*, 522, 6236
- Tacconi L. J., et al., 2013, *ApJ*, 768, 74
- Tacconi L. J., et al., 2018, *ApJ*, 853, 179
- Tacconi L. J., Genzel R., Sternberg A., 2020, *ARA&A*, 58, 157
- Tan V. Y. Y., et al., 2024, *arXiv e-prints*, p. [arXiv:2412.07829](https://arxiv.org/abs/2412.07829)
- Tiley A. L., et al., 2016, *MNRAS*, 460, 103
- Tohill C., Bamford S. P., Conselice C. J., Ferreira L., Harvey T., Adams N., Austin D., 2024, *ApJ*, 962, 164
- Toomre A., 1964, *ApJ*, 139, 1217
- Turner O. J., Harrison C. M., Cirasuolo M., McLure R. J., Dunlop J., Swinbank A. M., Tiley A. L., 2017a, *arXiv e-prints*, p. [arXiv:1711.03604](https://arxiv.org/abs/1711.03604)
- Turner O. J., et al., 2017b, *MNRAS*, 471, 1280
- Übler H., Naab T., Oser L., Aumer M., Sales L. V., White S. D. M., 2014, *MNRAS*, 443, 2092
- Übler H., et al., 2017, *ApJ*, 842, 121
- Übler H., et al., 2019, *ApJ*, 880, 48
- Übler H., et al., 2021, *MNRAS*, 500, 4597
- Übler H., et al., 2024, *MNRAS*, 533, 4287
- Varidel M. R., et al., 2020, *MNRAS*, 495, 2265
- Venturi G., et al., 2024, *A&A*, 691, A19
- Walter F., Brinks E., de Blok W. J. G., Bigiel F., Kennicutt Jr. R. C., Thornley M. D., Leroy A., 2008, *AJ*, 136, 2563
- Wang B., Cappellari M., Peng Y., Graham M., 2020, *MNRAS*, 495, 1958
- Weibel A., et al., 2024, *MNRAS*, 533, 1808
- Whitler L., Stark D. P., Endsley R., Leja J., Charlot S., Chevallard J., 2023, *MNRAS*, 519, 5859
- Williams C. C., et al., 2023, *ApJS*, 268, 64
- Wisnioski E., et al., 2011, *MNRAS*, 417, 2601
- Wisnioski E., et al., 2015, *ApJ*, 799, 209
- Wisnioski E., et al., 2019, *ApJ*, 886, 124
- Witstok J., et al., 2023, *Nature*, 621, 267
- Witten C., et al., 2025, *MNRAS*, 537, 112
- Wright S. A., Larkin J. E., Law D. R., Steidel C. C., Shapley A. E., Erb D. K., 2009, *ApJ*, 699, 421
- Wuyts S., et al., 2011, *ApJ*, 742, 96
- Wuyts E., et al., 2016a, *ApJ*, 827, 74
- Wuyts S., et al., 2016b, *ApJ*, 831, 149
- Yu X., et al., 2019, *MNRAS*, 486, 4463
- Zhang Y., Ouchi M., Nakajima K., Harikane Y., Isobe Y., Xu Y., Ono Y., Umeda H., 2024, *ApJ*, 970, 19
- Zhu L., et al., 2018, *Nature Astronomy*, 2, 233
- Zhu Y., et al., 2024, *arXiv e-prints*, p. [arXiv:2409.11464](https://arxiv.org/abs/2409.11464)
- Zolotov A., et al., 2015, *MNRAS*, 450, 2327
- de Graaff A., et al., 2024a, *A&A*, 684, A87
- de Graaff A., Pillepich A., Rix H.-W., 2024b, *ApJ*, 967, L40
- van Donkelaar F., Agertz O., Renaud F., 2022, *MNRAS*, 512, 3806
- van de Sande J., et al., 2018, *Nature Astronomy*, 2, 483
- van den Bosch F. C., 2001, *MNRAS*, 327, 1334
- van der Kruit P. C., Freeman K. C., 2011, *ARA&A*, 49, 301
- van der Wel A., et al., 2014, *ApJ*, 792, L6

## AFFILIATIONS

<sup>1</sup>*Kavli Institute for Cosmology, University of Cambridge, Madingley Road, Cambridge, CB3 0HA, UK*

<sup>2</sup>*Cavendish Laboratory, University of Cambridge, 19 JJ Thomson Avenue, Cambridge, CB3 0HE, UK*

<sup>3</sup>*Max-Planck-Institut für extraterrestrische Physik (MPE), Gießenbachstraße 1, 85748 Garching, Germany*

<sup>4</sup>*Max-Planck-Institut für Astronomie, Königstuhl 17, D-69117, Heidelberg, Germany*

<sup>5</sup>*Steward Observatory, University of Arizona, 933 N. Cherry Avenue, Tucson, AZ 85721, USA*

<sup>6</sup>*Center for Astrophysics | Harvard & Smithsonian, 60 Garden St., Cambridge MA 02138 USA*

<sup>7</sup>*Centro de Astrobiología (CAB), CSIC-INTA, Cra. de Ajalvir Km. 4, 28850- Torrejón de Ardoz, Madrid, Spain*

<sup>8</sup>*Department of Physics, University of Oxford, Denys Wilkinson Building, Keble Road, Oxford OX1 3RH, UK*

<sup>9</sup>*Scuola Normale Superiore, Piazza dei Cavalieri 7, I-56126 Pisa, Italy*

<sup>10</sup>*The University of Texas at Austin, Department of Astronomy, 2515 Speedway, Stop C1400, Austin, TX 78712-1205, USA*

<sup>11</sup>*DARK, Niels Bohr Institute, University of Copenhagen, Jagtvej 128, DK-2200 Copenhagen, Denmark*

<sup>12</sup>*Department of Astronomy, Tsinghua University, Beijing 100084, China*

<sup>13</sup>*Department of Astronomy and Astrophysics, University of California, Santa Cruz, 1156 High Street, Santa Cruz, CA 95064, USA*

<sup>14</sup>*NSF National Optical-Infrared Astronomy Research Laboratory, 950 North Cherry Avenue, Tucson, AZ 85719, USA*

## APPENDIX A: SAMPLE STATISTICS

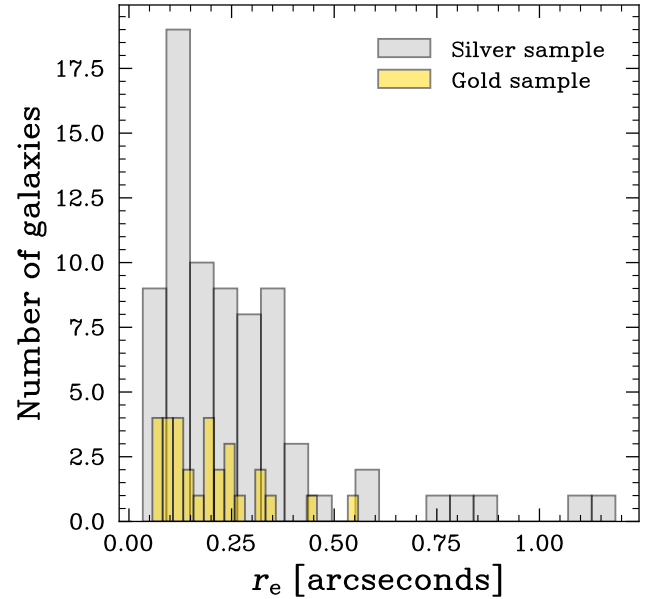
In this section, we present some summary tables for the key measurements of this work, as well as provide further insight into the physical distribution of our various sub-samples.

In Tabs. A1 and A2, we summarize the median values, for our extended and gold samples, of  $\sigma_0$  and  $v/\sigma_0$  in bins of redshift (Figs. 6, 7, and 8), and stellar mass, SFR, sSFR, and SFR surface density (Figs. 9 and 10). For each bin, we specify the range probed by the bin, the median value of the binned quantity, the number of galaxies  $N$  contained in the bin, and the average stellar mass  $\langle \log(M_\star [M_\odot]) \rangle$ . For completeness, we also include the average value of the rotational support when computed using the maximum observed velocity  $v_{\text{obs,max}}$  instead of the velocity at the effective radius  $v_{\text{re}}$ . We find consistent values, within the uncertainties, for the two measures of rotational support/ However we note that  $v_{\text{obs,max}}/\sigma_0$  is on average higher than  $v_{\text{re}}/\sigma_0$ .

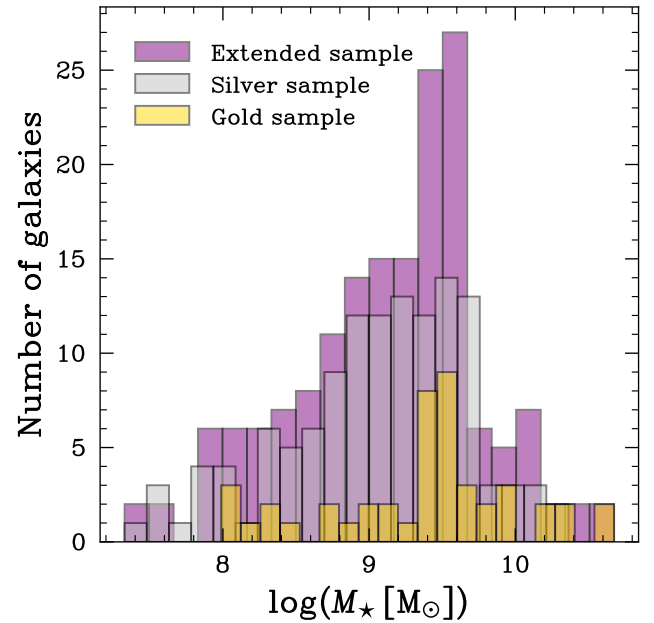
In Tab. A3, we summarize the physical properties of the galaxies in the gold sample, along with their best-fit kinematic measurements.

In order to study possible biases in the sizes probed by galaxies in our sub-samples, we plot the distribution of the best-fit H $\alpha$  effective radius  $r_e$  in arcseconds, for the gold and samples, on Fig. A1. We find that the two sample follow similar distributions, with the silver sample probing some larger systems at the tail end of the distribution. The cuts made to obtain the gold sample to not bias it in size compared to the silver one.

We further investigate the stellar mass distribution of galaxies in the gold, silver, and extended samples on Fig. A2. The gold and extended samples, which we use to compute our medians and correlations, have similar distributions, with the resolved sample having a slightly longer tail on the low mass end.



**Figure A1.** Effective radii  $r_e$ , in arcseconds, of the galaxies in our gold and silver sample.



**Figure A2.** Stellar mass distribution of the galaxies in our gold, silver sample, and extended samples.

## APPENDIX B: IMPACT OF SELECTION CUTS ON INFERRED CORRELATIONS

We will now discuss how the correlations presented in Secs. 4.2.1 and 4.2.2 change if we only select rotation-supported galaxies and if we compute the rotational support  $v/\sigma_0$  with  $v_{\text{obs,max}}$  instead of the velocity at the effective radius  $v_{\text{re}}$ . The results are summarized on Tab. B1, for correlations between  $\sigma_0$  and  $v/\sigma_0$  and  $\log(M_\star [M_\odot])$ , SFR, sSFR, and SFR surface density. We find that the quantitative results do not change between scenarios, but the strength ( $\rho$ ) and significance ( $p$ ) of the correlations change. For the  $v/\sigma_0 > 1$  case,

Bin	Bin median	N	$\langle \log(M_\star [M_\odot]) \rangle$	$\langle v/\sigma_0 \rangle$	$\langle v_{\text{obs,max}}/\sigma_0 \rangle$	$\langle \sigma_0 \text{ [km/s]} \rangle$
$3.8 < z < 4.2$	4.03	32	9.43	$1.2^{+1.1}_{-0.7}$	$1.2^{+1.2}_{-0.7}$	$77^{+55}_{-36}$
$4.2 < z < 5.0$	4.55	32	9.07	$1.0^{+1.5}_{-0.5}$	$0.7^{+1.2}_{-0.3}$	$68^{+44}_{23}$
$5.0 < z < 6.1$	5.21	16	9.46	$0.8^{+1.2}_{-0.2}$	$0.9^{+1.3}_{-0.3}$	$98^{+40}_{-30}$
$7.5 < \log(M_\star [M_\odot]) < 9.0$	8.43	22	8.41	$0.6^{+1.3}_{-0.2}$	$0.7^{+1.3}_{-0.3}$	$67^{+52}_{-20}$
$9.0 < \log(M_\star [M_\odot]) < 9.5$	9.36	28	9.32	$1.1^{+1.1}_{-0.6}$	$1.1^{+1.1}_{-0.6}$	$74^{+50}_{-33}$
$9.5 < \log(M_\star [M_\odot]) < 10.5$	9.8	30	9.9	$0.8^{+1.7}_{-0.4}$	$0.8^{+1.7}_{-0.4}$	$93^{+55}_{-52}$
$0 < \log(\text{SFR}_{10} [M_\odot/\text{yr}]) < 0.8$	0.61	35	8.82	$0.7^{+1.1}_{-0.3}$	$0.7^{+1.1}_{-0.3}$	$68^{+50}_{-21}$
$0.8 < \log(\text{SFR}_{10} [M_\odot/\text{yr}]) < 1.3$	1.02	33	9.47	$0.9^{+1.1}_{-0.5}$	$0.9^{+1.0}_{-0.6}$	$84^{+48}_{-33}$
$1.3 < \log(\text{SFR}_{10} [M_\odot/\text{yr}]) < 2.5$	1.62	12	10.16	$1.0^{+3.0}_{-0.5}$	$1.0^{+3.0}_{-0.5}$	$107^{+79}_{-67}$
$0 < \log(\text{sSFR}_{10} [M_\odot/\text{yr}]) < 0.5$	0.29	27	9.61	$0.7^{+0.9}_{-0.3}$	$0.7^{+0.9}_{-0.3}$	$77^{+40}_{-39}$
$0.5 < \log(\text{sSFR}_{10} [M_\odot/\text{yr}]) < 1.0$	0.68	31	9.36	$1.2^{+1.2}_{-0.6}$	$1.2^{+1.0}_{-0.6}$	$79^{+59}_{-39}$
$1.0 < \log(\text{sSFR}_{10} [M_\odot/\text{yr}]) < 2.0$	1.30	16	8.34	$0.7^{+2.0}_{-0.3}$	$0.7^{+2.1}_{-0.3}$	$67^{+39}_{-18}$
$-1 < \log(\Sigma_{\text{SFR}_{10}} [M_\odot/\text{yr}/\text{kpc}^2]) < -0.2$	-0.40	32	8.90	$0.7^{+1.1}_{-0.3}$	$0.7^{+1.1}_{-0.3}$	$69^{+43}_{-31}$
$-0.2 < \log(\Sigma_{\text{SFR}_{10}} [M_\odot/\text{yr}/\text{kpc}^2]) < 0.2$	0.01	37	9.48	$1.1^{+1.5}_{-0.7}$	$1.1^{+1.5}_{-0.7}$	$80^{+58}_{-30}$
$0.2 < \log(\Sigma_{\text{SFR}_{10}} [M_\odot/\text{yr}/\text{kpc}^2]) < 1.0$	0.33	11	9.77	$0.9^{+1.6}_{-0.4}$	$0.9^{+1.7}_{-0.4}$	$100^{+71}_{-73}$

**Table A1.** Summary table of the medians for the extended galaxies in the gold and silver sample, for bins of redshift (Figs. 6, 7, and 8), and stellar mass, SFR, sSFR, and SFR surface density (Figs. 9 and 10). For each bin, we specify the range probed by the bin, the median value of the binned quantity, the number of galaxies  $N$  contained in the bin, and the average stellar mass  $\langle \log(M_\star [M_\odot]) \rangle$ . We also include the average value of the rotational support when computed using the maximum observed velocity  $v_{\text{obs,max}}$  instead of the velocity at the effective radius  $v_{\text{re}}$ .

the correlations typically get weaker, but this is mostly driven by the significant decrease in sample size. For the  $v_{\text{rot}} = v_{\text{obs,max}}$  case, the coefficients  $\rho$  stay consistent within 10%.

### APPENDIX C: FURTHER INVESTIGATION OF THE EFFECT OF SF ON KINEMATICS

We present in this section additional tests done to study the origin of the  $\sigma_0 - \text{SFR}$  correlation shown on Figs. 9 and 10. As discussed in Sec. 4.2.1, this correlation naturally arises from models where gravitational instabilities, driven by radial transport of gas through the disk, and stellar feedback inject turbulence into the ISM. Both of these processes are linked to star-formation, hence producing the observed trend. However, it is unclear which of these processes is the dominant driver at high redshift. The low masses probed  $\log M_\star [M_\odot] \lesssim 10$  make galaxies more unstable to gravitational instabilities, but also increase the impact of stellar feedback on the gas.

On Fig. C1 we show the  $\sigma_0 - \text{SFR}$  relation for the gold and silver sample in three redshift bins, along with the Spearman rank coefficient  $\rho$  and p-value  $p$ , computed for the resolved galaxies only. We see that in each bin, which all probe  $\approx 0.2$  Gyr, we do not find significant correlations. This implies that the  $\sigma_0 - \text{SFR}$  relation shown in Fig. 9, which is calculated for the extended sample across the full redshift range  $z \sim 4-6$  probed by the work, could be mainly explained by the redshift evolution of the SFR and the stellar masses. However, we note that these bins suffer from reduced sample sizes compared

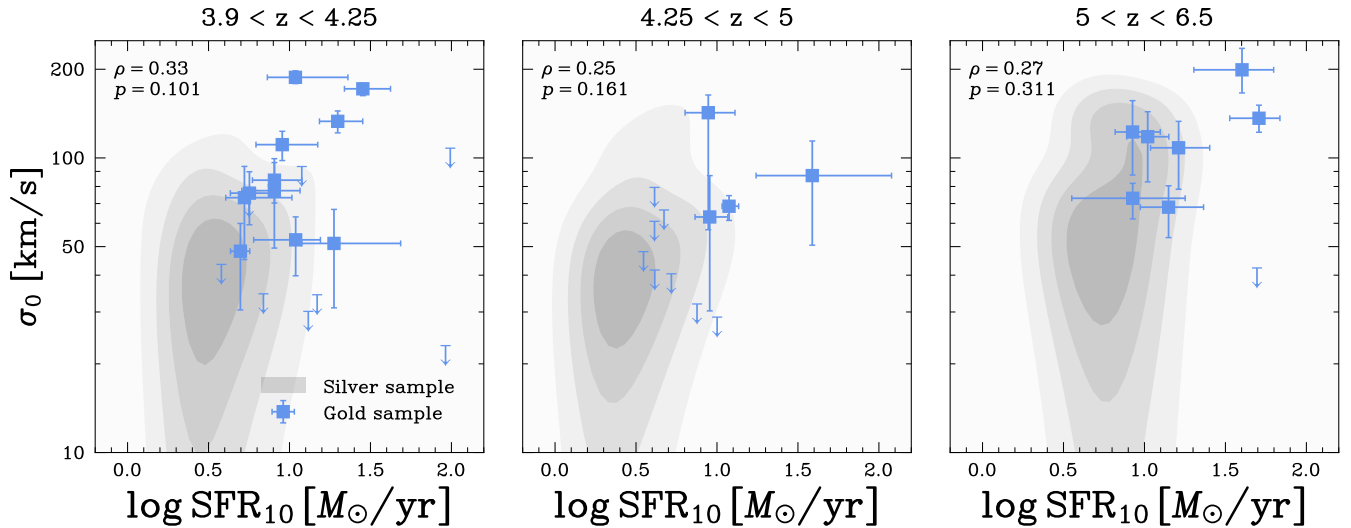
to the full sample, so this naturally decreases the significance of any correlations.

We further investigate the role of stellar feedback and gravitational instabilities by exploring trends with the offset from the main sequence  $\Delta\text{MS} = \text{SFR}/\text{SFR}_{\text{MS}}$ , as shown on Fig. C2 for our gold and silver samples. We use the SFMS prescription from Simmonds et al., in prep (Fig. 2). Although we find no correlation between  $\sigma_0$  and  $\Delta\text{MS}$ , we find a slight positive correlation between  $\sigma_0$  and  $\Delta\text{MS}$  ( $\rho = 0.19$ ), although the significance  $p = 0.094$  is low. However, the trend is not significant enough to draw conclusions. This is overall consistent with findings from Übler et al. (2019).

Finally, we explore the distribution of  $\sigma_0$  and  $v/\sigma_0$  on the  $M_\star - \text{SFR}$  plane and plot our results on Fig. C3. There is no clear trend relating the kinematics to this plane, it appears that on average, galaxies with high rotational support  $v/\sigma_0 > 3$  lie close to the SFMS. An in-depth study of these results would require the study of individual galaxies on this plane in order to try to uncover the drivers of rotational support in each case, but this is beyond the scope of this work.

When studying correlations between  $v/\sigma_0$  and physical properties such as SFR and stellar masses, it is interesting to study the role of both  $v = v_{\text{rot}}$  and  $\sigma_0$  in driving the observed trends. On Fig. C4 we show the relations between the rotational velocity and  $\log M_\star [M_\odot]$  and SFRs. We find no correlation in both cases, meaning that at these redshifts  $z \gtrsim 4$  and stellar masses  $\log M_\star [M_\odot] \lesssim 10$ , rotational velocity does not strongly depend on stellar mass. This implies that

Bin	Mean value	N	$\langle \log(M_\star [M_\odot]) \rangle$	$\langle v_{\text{re}}/\sigma_0 \rangle$	$\langle v_{\text{obs,max}}/\sigma_0 \rangle$	$\langle \sigma_0 \text{ [km/s]} \rangle$
$3.8 < z < 4.2$	4.04	21	9.46	$1.1^{+0.8}_{-0.6}$	$1.1^{+0.8}_{-0.6}$	$74^{+60}_{-41}$
$4.2 < z < 5.0$	4.41	12	9.14	$1.0^{+1.5}_{-0.5}$	$1.0^{+1.5}_{-0.5}$	$52^{+35}_{-22}$
$5.0 < z < 6.1$	5.29	8	9.69	$0.8^{+1.1}_{-0.2}$	$0.8^{+1.2}_{-0.2}$	$103^{+33}_{-35}$
$7.5 < \log(M_\star [M_\odot]) < 9.0$	8.49	22	8.51	$1.2^{+0.8}_{-0.7}$	$0.7^{+1.3}_{-0.3}$	$56^{+17}_{-11}$
$9.0 < \log(M_\star [M_\odot]) < 9.5$	9.37	28	9.32	$1.5^{+0.9}_{-0.8}$	$1.1^{+1.1}_{-0.6}$	$66^{+52}_{-28}$
$9.5 < \log(M_\star [M_\odot]) < 10.5$	9.85	30	9.93	$0.8^{+1.1}_{-0.8}$	$0.8^{+1.7}_{-0.4}$	$93^{+55}_{-61}$
$0 < \log(\text{SFR}_{10} [M_\odot/\text{yr}]) < 0.8$	0.61	35	8.60	$0.7^{+2.0}_{-0.2}$	$1.1^{+0.8}_{-0.6}$	$49^{+12}_{-8}$
$0.8 < \log(\text{SFR}_{10} [M_\odot/\text{yr}]) < 1.3$	0.95	33	9.33	$1.2^{+0.7}_{-0.6}$	$1.2^{+0.7}_{-0.7}$	$68^{+49}_{-36}$
$1.3 < \log(\text{SFR}_{10} [M_\odot/\text{yr}]) < 2.5$	1.59	12	10.01	$0.8^{+1.0}_{-0.3}$	$0.8^{+1.0}_{-0.4}$	$112^{+59}_{-72}$
$0 < \log(\text{sSFR}_{10} [M_\odot/\text{yr}]) < 0.5$	0.32	27	9.69	$0.7^{+0.8}_{-0.1}$	$0.7^{+0.8}_{-0.3}$	$56^{+54}_{-26}$
$0.5 < \log(\text{sSFR}_{10} [M_\odot/\text{yr}]) < 1.0$	0.65	31	9.49	$1.3^{+1.1}_{-0.7}$	$1.3^{+1.1}_{-0.7}$	$92^{+46}_{-51}$
$1.0 < \log(\text{sSFR}_{10} [M_\odot/\text{yr}]) < 2.0$	1.37	16	8.41	$0.7^{+1.2}_{-0.2}$	$0.7^{+1.3}_{-0.2}$	$57^{+11}_{-8}$
$-1 < \log(\Sigma_{\text{SFR}_{10}} [M_\odot/\text{yr}/\text{kpc}^2]) < -0.2$	-0.34	32	9.03	$1.0^{+1.5}_{-0.5}$	$1.0^{+1.4}_{-0.5}$	$44^{+31}_{-12}$
$-0.2 < \log(\Sigma_{\text{SFR}_{10}} [M_\odot/\text{yr}/\text{kpc}^2]) < 0.2$	0.06	37	9.45	$1.2^{+0.7}_{-0.6}$	$1.2^{+0.7}_{-0.6}$	$73^{+60}_{-22}$
$0.2 < \log(\Sigma_{\text{SFR}_{10}} [M_\odot/\text{yr}/\text{kpc}^2]) < 1.0$	0.30	11	9.79	$0.8^{+0.8}_{-0.4}$	$0.8^{+0.8}_{-0.4}$	$93^{+78}_{-66}$

**Table A2.** Summary table of the medians for the gold sample, following the same format as Tab. A1.**Figure C1.**  $\sigma_0$  – SFR relation for our gold (blue squares) and silver (gray contours) samples in three redshift bins spanning  $\approx 0.2$  Gyr each. We show the Spearman rank correlation coefficients ( $\rho$ ) and p-values ( $p$ ) computed from the extended galaxies only, and find no significant correlations in the individual bins.

the correlations measured on Fig. 9 are mainly driven by the evolution of  $\sigma_0$ .

#### APPENDIX D: GEKO RECOVERY TESTS

In this section, we present the key recovery tests done for our tool GEKO. The full presentation of the code and the tests will be done in an upcoming dedicated paper (Danhaive et al., in prep). On Fig. D1 we show the results for the recovery of the key model-derived

JADES ID	$z$	$\log(M_\star [M_\odot])$	$\log(\text{SFR} [M_\odot/\text{yr}])$	$r_e$ [kpc]	$v/\sigma_0$	$\sigma_0$ [km/s]	$\log(M_{\text{dyn}} [M_\odot])$
1028887	5.19	$9.56^{+0.19}_{-0.19}$	$1.15^{+0.22}_{-0.17}$	$1.12^{+0.11}_{-0.10}$	$0.3^{+0.3}_{-0.2}$	$68^{+12}_{-14}$	$9.88^{+0.13}_{-0.17}$
1002030	5.18	$9.48^{+0.18}_{-0.24}$	$0.93^{+0.17}_{-0.11}$	$1.37^{+0.19}_{-0.18}$	$0.6^{+0.4}_{-0.3}$	$122^{+34}_{-35}$	$10.5^{+0.17}_{-0.21}$
191250	5.39	$10.17^{+0.30}_{-0.09}$	$1.69^{+0.24}_{-0.17}$	$2.45^{+0.06}_{-0.06}$	$13.9^{+5.0}_{-5.0}$	< 39	$10.8^{+0.07}_{-0.08}$
1002222	5.29	$9.47^{+0.18}_{-0.44}$	$0.93^{+0.32}_{-0.38}$	$0.98^{+0.17}_{-0.13}$	$0.5^{+0.4}_{-0.3}$	$73^{+9}_{-11}$	$9.91^{+0.10}_{-0.12}$
214966	5.54	$9.54^{+0.16}_{-0.21}$	$1.21^{+0.19}_{-0.17}$	$1.41^{+0.10}_{-0.10}$	$0.5^{+0.3}_{-0.3}$	$108^{+25}_{-30}$	$10.4^{+0.15}_{-0.22}$
1025527	5.3	$9.39^{+0.16}_{-0.56}$	$1.02^{+0.13}_{-0.13}$	$1.06^{+0.18}_{-0.14}$	$1.9^{+1.1}_{-0.6}$	$118^{+25}_{-35}$	$10.6^{+0.24}_{-0.23}$
1001674	5.18	$9.92^{+0.17}_{-0.13}$	$1.60^{+0.20}_{-0.30}$	$1.60^{+0.18}_{-0.17}$	$0.5^{+0.4}_{-0.4}$	$199^{+36}_{-33}$	$11.0^{+0.15}_{-0.15}$
201125	5.82	$9.96^{+0.10}_{-0.16}$	$1.71^{+0.13}_{-0.18}$	$1.86^{+0.16}_{-0.15}$	$0.8^{+0.3}_{-0.3}$	$136^{+15}_{-14}$	$10.8^{+0.09}_{-0.09}$
1094616	4.06	$9.40^{+0.16}_{-0.36}$	$1.04^{+0.32}_{-0.17}$	$1.35^{+0.12}_{-0.10}$	$1.3^{+0.2}_{-0.2}$	$187^{+9}_{-8}$	$11.0^{+0.06}_{-0.06}$
1000989	3.97	$9.07^{+0.11}_{-0.24}$	$0.58^{+0.23}_{-0.12}$	$0.87^{+0.07}_{-0.06}$	$5.4^{+5.0}_{-2.6}$	< 39	$9.76^{+0.14}_{-0.16}$
1088814	4.41	$10.60^{+0.13}_{-0.36}$	$1.59^{+0.49}_{-0.35}$	$2.39^{+0.08}_{-0.08}$	$1.5^{+1.2}_{-0.4}$	$87^{+27}_{-36}$	$10.6^{+0.14}_{-0.21}$
1087148	4.38	$8.24^{+0.28}_{-0.33}$	$0.61^{+0.14}_{-0.11}$	$1.05^{+0.24}_{-0.19}$	$2.4^{+3.3}_{-1.6}$	< 63	$9.82^{+0.72}_{-0.62}$
1015956	4.02	$9.54^{+0.12}_{-0.35}$	$0.84^{+0.20}_{-0.20}$	$1.40^{+0.15}_{-0.14}$	$1.7^{+4.6}_{-1.3}$	< 32	$9.08^{+0.43}_{-0.64}$
1085659	4.06	$10.17^{+0.13}_{-0.42}$	$1.27^{+0.41}_{-0.20}$	$1.47^{+0.11}_{-0.10}$	$0.3^{+0.4}_{-0.2}$	$51^{+16}_{-21}$	$9.76^{+0.22}_{-0.41}$
1083165	4.15	$9.78^{+0.09}_{-0.13}$	$0.96^{+0.22}_{-0.16}$	$1.12^{+0.07}_{-0.07}$	$0.6^{+0.2}_{-0.2}$	$111^{+12}_{-13}$	$10.3^{+0.09}_{-0.01}$
1065488	4.15	$8.01^{+0.42}_{-0.15}$	$0.75^{+0.08}_{-0.08}$	$1.10^{+0.14}_{-0.14}$	$2.1^{+1.5}_{-0.6}$	< 68	$9.94^{+0.20}_{-0.26}$
1025101	4.91	$8.99^{+0.29}_{-0.20}$	$0.95^{+0.17}_{-0.14}$	$1.19^{+0.16}_{-0.13}$	$1.9^{+1.3}_{-0.4}$	$142^{+21}_{-85}$	$10.8^{+0.20}_{-0.45}$
1090526	3.96	$9.93^{+0.12}_{-0.24}$	$1.08^{+0.38}_{-0.23}$	$2.47^{+0.13}_{-0.13}$	$1.4^{+3.1}_{-0.9}$	< 86	$10.1^{+0.37}_{-0.39}$
1077545	4.42	$9.27^{+0.11}_{-0.36}$	$0.96^{+0.11}_{-0.09}$	$0.87^{+0.09}_{-0.09}$	$1.1^{+1.4}_{-0.7}$	$63^{+24}_{-33}$	$9.86^{+0.22}_{-0.34}$
1089583	3.93	$9.01^{+0.16}_{-0.35}$	$0.72^{+0.29}_{-0.12}$	$1.16^{+0.15}_{-0.13}$	$2.2^{+0.8}_{-0.5}$	$73^{+20}_{-28}$	$10.3^{+0.19}_{-0.28}$
1077261	3.92	$9.36^{+0.24}_{-0.20}$	$0.91^{+0.16}_{-0.20}$	$1.12^{+0.19}_{-0.16}$	$0.5^{+0.5}_{-0.3}$	$77^{+22}_{-28}$	$10.0^{+0.17}_{-0.31}$
1095186	4.02	$9.37^{+0.10}_{-0.22}$	$0.75^{+0.17}_{-0.12}$	$1.92^{+0.30}_{-0.27}$	$1.1^{+0.8}_{-0.6}$	$76^{+14}_{-17}$	$10.3^{+0.22}_{-0.20}$
1091580	4.8	$8.09^{+0.31}_{-0.29}$	$0.61^{+0.11}_{-0.09}$	$0.88^{+0.18}_{-0.16}$	$1.0^{+3.4}_{-0.8}$	< 56	$9.45^{+0.32}_{-0.53}$
1086992	4.04	$9.37^{+0.23}_{-0.46}$	$1.12^{+0.26}_{-0.27}$	$3.42^{+0.20}_{-0.20}$	$4.7^{+5.0}_{-2.9}$	< 28	$9.84^{+0.34}_{-0.36}$
1090054	4.82	$9.62^{+0.04}_{-0.06}$	$1.07^{+0.06}_{-0.04}$	$1.27^{+0.06}_{-0.06}$	$3.4^{+0.5}_{-0.4}$	$68^{+6}_{-7}$	$10.6^{+0.06}_{-0.06}$
1014130	4.38	$8.49^{+0.22}_{-0.31}$	$0.67^{+0.08}_{-0.09}$	$1.32^{+0.22}_{-0.20}$	$1.9^{+3.9}_{-1.4}$	< 61	$9.78^{+0.47}_{-0.05}$
1082948	3.91	$10.68^{+0.08}_{-0.20}$	$1.96^{+0.38}_{-0.44}$	$2.25^{+0.13}_{-0.12}$	$1.4^{+4.4}_{-1.0}$	< 22	$8.87^{+0.43}_{-0.60}$
1000110	4.06	$9.52^{+0.34}_{-0.08}$	$1.30^{+0.15}_{-0.11}$	$1.66^{+0.09}_{-0.08}$	$1.5^{+0.2}_{-0.2}$	$133^{+11}_{-11}$	$10.8^{+0.05}_{-0.05}$
1091153	4.07	$10.37^{+0.14}_{-0.14}$	$1.99^{+0.24}_{-0.23}$	$1.85^{+0.09}_{-0.10}$	$1.4^{+2.0}_{-0.5}$	< 98	$10.3^{+0.25}_{-0.34}$
1094903	3.87	$10.34^{+0.08}_{-0.23}$	$1.32^{+0.20}_{-0.20}$	$2.06^{+0.11}_{-0.10}$	$0.5^{+0.2}_{-0.2}$	$148^{+15}_{-16}$	$10.8^{+0.08}_{-0.09}$
1079264	4.05	$8.73^{+0.56}_{-0.30}$	$1.17^{+0.26}_{-0.08}$	$2.24^{+0.17}_{-0.15}$	$1.6^{+4.2}_{-1.2}$	< 32	$9.24^{+0.44}_{-0.65}$

**Table A3.** Kinematic measurements and star formation properties for the galaxies in the gold sample.

JADES ID	$z$	$\log(M_\star [M_\odot])$	$\log(\text{SFR} [M_\odot/\text{yr}])$	$r_e$ [kpc]	$v/\sigma_0$	$\sigma_0$ [km/s]	$\log(M_{\text{dyn}} [M_\odot])$
1086406	4.41	$9.46^{+0.18}_{-0.32}$	$1.00^{+0.27}_{-0.25}$	$0.91^{+0.14}_{-0.12}$	$6.3^{+5.0}_{-3.5}$	< 27	$9.48^{+0.28}_{-0.34}$
1013488	3.8	$9.57^{+0.11}_{-0.33}$	$1.19^{+0.25}_{-0.11}$	$1.07^{+0.07}_{-0.07}$	$1.4^{+0.2}_{-0.2}$	$113^{+10}_{-13}$	$10.5^{+0.09}_{-0.10}$
1028072	4.4	$9.17^{+0.08}_{-0.14}$	$0.62^{+0.12}_{-0.09}$	$1.66^{+0.23}_{-0.20}$	$3.7^{+5.0}_{-2.5}$	< 39	$9.76^{+0.37}_{-0.50}$
1090742	4.62	$9.37^{+0.16}_{-0.26}$	$0.72^{+0.27}_{-0.30}$	$1.34^{+0.16}_{-0.14}$	$3.7^{+5.0}_{-2.3}$	< 37	$9.61^{+0.33}_{-0.46}$
1091236	4.17	$9.34^{+0.15}_{-0.50}$	$0.91^{+0.17}_{-0.14}$	$0.84^{+0.09}_{-0.08}$	$0.9^{+0.3}_{-0.3}$	$84^{+12}_{-14}$	$10.0^{+0.09}_{-0.11}$
1009935	4.89	$9.65^{+0.11}_{-0.25}$	$0.88^{+0.20}_{-0.24}$	$1.02^{+0.12}_{-0.11}$	$2.1^{+5.0}_{-1.5}$	< 29	$8.99^{+0.42}_{-0.59}$
1085494	4.06	$8.90^{+0.39}_{-0.15}$	$1.04^{+0.15}_{-0.26}$	$1.06^{+0.10}_{-0.10}$	$1.6^{+0.6}_{-0.4}$	$53^{+10}_{-13}$	$9.85^{+0.13}_{-0.15}$
1090891	3.92	$9.74^{+0.44}_{-0.22}$	$1.45^{+0.17}_{-0.11}$	$1.55^{+0.07}_{-0.07}$	$1.1^{+0.1}_{-0.1}$	$172^{+8}_{-9}$	$10.9^{+0.05}_{-0.05}$
1008197	4.4	$8.76^{+0.21}_{-0.24}$	$0.55^{+0.15}_{-0.12}$	$1.11^{+0.19}_{-0.16}$	$3.9^{+5.0}_{-2.4}$	< 44	$9.77^{+0.35}_{-0.47}$
1029814	4.16	$8.38^{+0.18}_{-0.17}$	$0.70^{+0.06}_{-0.06}$	$1.28^{+0.26}_{-0.21}$	$3.2^{+2.1}_{-1.1}$	$48^{+12}_{-18}$	$10.2^{+0.32}_{-0.33}$

Table A3. Continued.

Sample	$v/\sigma_0$ (full)	$v/\sigma_0$ ( $v/\sigma_0 > 1$ )	$v/\sigma_0$ ( $v_{\text{rot}} = v_{\text{obs,max}}$ )	$\sigma_0$ (full)	$\sigma_0$ ( $v/\sigma_0 > 1$ )
$\log(M_\star [M_\odot])$	$\rho = -0.27$ $p = 0.015$	$\rho = -0.38$ $p = 0.019$	$\rho = -0.23$ $p = 0.044$	$\rho = 0.24$ $p = 0.036$	$\rho = 0.28$ $p = 0.094$
SFR <sub>10</sub>	$\rho = -0.30$ $p = 0.007$	$\rho = -0.08$ $p = 0.653$	$\rho = -0.27$ $p = 0.016$	$\rho = 0.40$ $p = 0.000$	$\rho = 0.39$ $p = 0.017$
sSFR <sub>10</sub>	$\rho = 0.15$ $p = 0.183$	$\rho = 0.48$ $p = 0.003$	$\rho = 0.11$ $p = 0.326$	$\rho = -0.02$ $p = 0.875$	$\rho = 0.07$ $p = 0.692$
$\Sigma_{\text{SFR}}$	$\rho = -0.29$ $p = 0.010$	$\rho = -0.10$ $p = 0.558$	$\rho = -0.26$ $p = 0.018$	$\rho = 0.38$ $p = 0.001$	$\rho = -0.06$ $p = 0.712$

Table B1. Spearman correlation coefficients ( $\rho$ ) and p-values ( $p$ ) for the four parameters cited in the paper, for  $v/\sigma_0$  and  $\sigma_0$  in the case where the full (extended) sample is used, when only rotationally supported galaxies  $v/\sigma_0 > 1$  are used, and when we use  $v_{\text{rot}} = v_{\text{obs,max}}$  instead of  $v_{\text{rot}} = v_{\text{re}}$ .

parameters  $\sigma_0$  and  $v_{\text{re}}$  (which are used to compute  $v/\sigma_0$ ), for different angles of mock galaxies with respect to the dispersion direction  $\text{PA} = 90^\circ$ . These tests are done on mock data, with an integrated  $\text{S/N} = 40$ , and a range of velocity dispersions  $\sigma_0 = 5 - 500$  km/s and rotational velocities  $v_{\text{re}} = 5 - 250$  km/s. The values plotted on Fig. D1 are averaged over all values of  $v_{\text{re}}$  for the  $\sigma_0$  recovery test and vice-versa. When the galaxy is parallel to the dispersion direction, we are not able to accurately recover  $\sigma_0$ , which is artificially boosted. This unphysical value of  $\sigma_0$  is driven by the degeneracy between morphology, velocity, and velocity dispersion when the galaxy is parallel to the slit. For this reason, we discard galaxies with  $\text{PA} > 75^\circ$ . As shown on Fig. D1, our results converge to the true values, within uncertainties, when  $\text{PA} < 75^\circ$ , which is why we use this cut to define our sample. We obtain the best recovery when galaxies as perpendicular to the dispersion direction,  $\text{PA} = 0^\circ$ . We can further see that, for cases  $\text{PA} < 15^\circ$ , we are able to recover values of  $\sigma_0 \approx 20$  km/s, which is well below the instrument LSF  $\sigma_0 \approx 80$  km/s.

We also test the effect of integrated  $\text{S/N}$  on our ability to recover kinematic parameters for our mock galaxies. We show the results on Fig. D2, for  $\sigma_0 = 100$  km/s and  $v_{\text{re}} = 170$  km/s. Beyond  $\text{S/N} = 10$ , the recovered value of  $\sigma_0$  is consistent with the true input value within the uncertainties. We set  $\text{S/N} > 10$  as our cut for the silver sample,

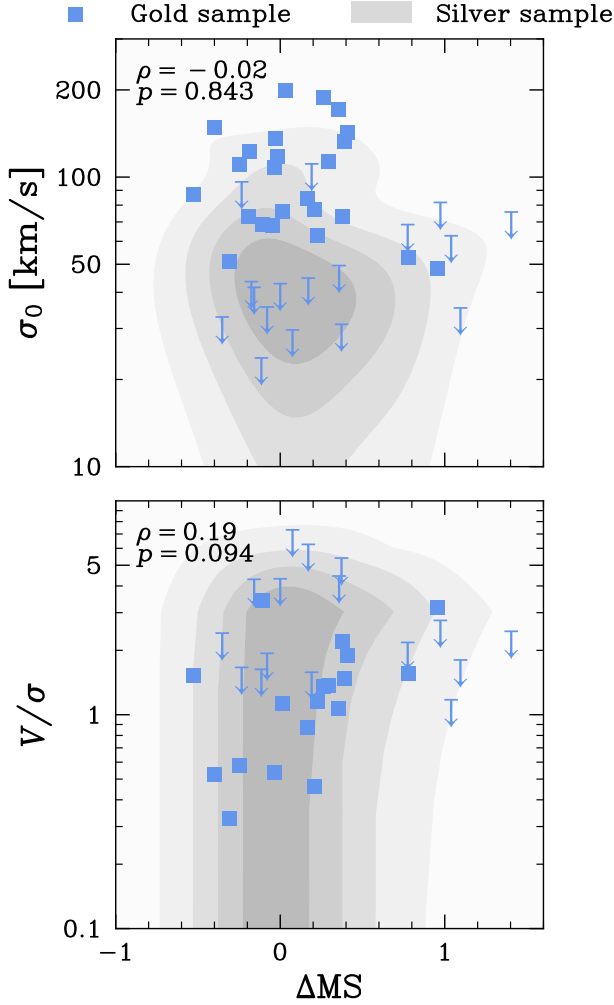
and  $\text{S/N} > 20$  for the gold sample. The uncertainty decreases with increasing  $\text{S/N}$  and decreasing  $\text{PA}$ .

## APPENDIX E: COMPARISON TO $Z < 4$ MEASUREMENTS

In this section, we briefly introduce the studies we compare our measurements to (Figs. 8, 7, and 10) and discuss how their methods differ from those used in this work and how that may affect the direct comparisons we make.

The MOSFIRE Deep Evolution Field (MOSDEF) survey data is described in Price et al. (2020), and is obtained using the MOSFIRE spectrograph on the Keck telescope. This survey is comprised of rest-frame optical 2D moderate-resolution spectra  $R \sim 3000 - 3600$  for galaxies in the CANDELS field at  $z \sim 1.4 - 3.8$ . The kinematic analysis is restricted to galaxies whose major axis is roughly aligned with the slit and that are spatially resolved. Their final sample is made up of  $\sim 700$  galaxies detected in  $\text{H}\alpha$ , [OIII], and  $\text{H}\beta$ , in order of availability. Their kinematic modelling is similar to the one adopted in this paper. They assume an intrinsic axis ratio (i.e., axis ratio for an edge-on view)  $(b/a)_0 = 0.19$ , and model the velocities with an arctangent model and a constant velocity dispersion across the galaxy. Using inferred posterior distributions, they compute  $\sigma_0$



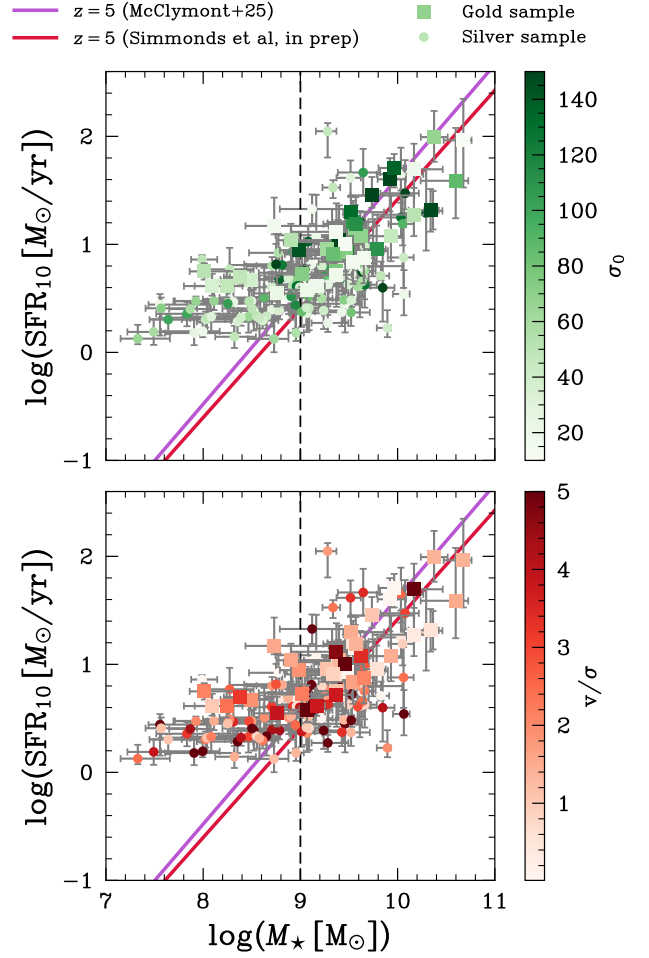


**Figure C2.** Evolution of  $\sigma_0$  (top panel) and  $v/\sigma_0$  (bottom panel) with the offset from the SFMS (Simmonds et al, in prep)  $\Delta MS = SFR/SFR_{MS}$ . We plot our gold (blue squares) and silver (gray contours) samples, and find no significant trends, as highlighted by the Spearman correlation coefficients  $\rho$  and p-values  $p$ , which are computed for the extended sample.

and the rotational support, which they define as  $v_{2.2}/\sigma_0$  where  $v_{2.2} = V(r = 2.2r_s)$ . This is important to note as typically  $v_{2.2} > v_{re}$ , which can boost the  $v/\sigma_0$  measurements compared to those in this work.

The K-band multi-object spectrograph (KMOS)<sup>3D</sup> survey data described in Wisnioski et al. (2015) is obtained using the KMOS integral field spectrograph on Keck. Galaxies are observed in  $H\alpha$  across five deep fields (COSMOS, GOODS-S, GOODS-N, UDS, and AEGIS) and span redshifts  $z \sim 0.7 - 2.7$ . For the kinematic fitting, each spaxel is fit with a 1D Gaussian model including the instrument LSF. The velocity dispersions are computed in the outer regions that are less affected by beam smearing. They define the rotational support  $v/\sigma_0$  with  $v_{rot} = v_{obs}/\sin i$ , where  $v_{obs}$  is an observed velocity difference from the maximal and minimal velocities of the velocity axis profile. This overall velocity gradient is usually greater than the velocity measured at the effective radius, which could bias the measurements high compared to this work.

The SIGMA survey (Simons et al. 2016, 2017) is a Keck/MOSFIRE survey, which targeted 97  $z \sim 2$  star-forming galaxies in the GOODS-S, GOODS-N and UDS fields, detected in  $H\alpha$

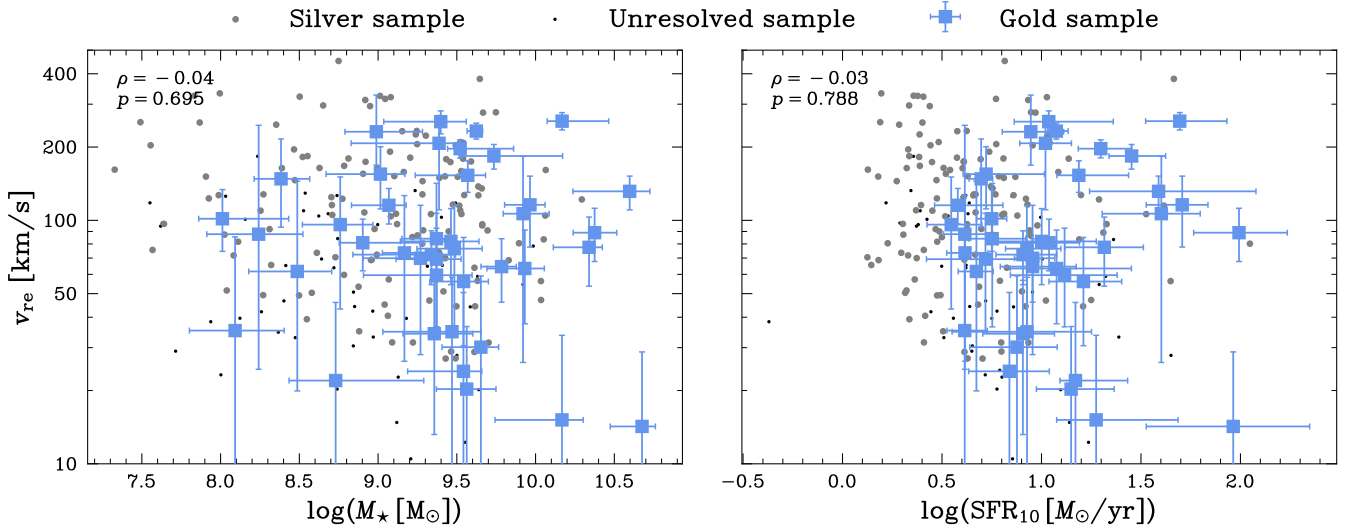


**Figure C3.** Distribution of our gold (squares) and silver (circles) samples on the  $M_\star - SFR$  plane, color-coded by intrinsic velocity dispersion  $\sigma_0$  (top panel) and rotational support  $v/\sigma_0$  (bottom panel). We plot the SFMS prescriptions from McClymont et al. (2025a) and Simmonds et al (in prep).

or [OIII]. The kinematic modelling assumes an arctangent velocity model and  $q_0 = 0.2$ . The velocity used for the rotational support represents the asymptotic velocity measured in the flat outer end of the rotation curve.

The KMOS Deep Survey (KDS) survey is described in (Turner et al. 2017b). Galaxies at  $z \sim 3.5$  are observed through their [OIII] emission, where the ionised gas kinematics are computed using an arctangent model. The rotational velocity is computed as the best-fit velocity at  $r = 2r_e$ , which is comparable to the velocity at the radius enclosing 80% of the total light  $v_{80}$  (Tiley et al. 2016). In the thin disk model, we expect the rotation curve to increase beyond  $r_e$ , where it is measured in this work, so the velocities at  $r = 2r_e$  could be higher. However, the velocities for a thick exponential disk  $n = 1$  would peak at  $r \approx 1.38r_e$ , so the relation between velocities at  $r = r_e$  and  $r = 2r_e$  varies depending on the object.

The KROSS survey (Johnson et al. 2018) is also a KMOS survey which observed  $\sim 800$  star-forming galaxies at  $z \sim 1$  using  $H\alpha$ . The kinematic modelling assumes an intrinsic axis ratio  $q_0 = 0.2$  and computes the velocity for the rotational support as the velocity at  $r = 2r_e$ . Both this velocity and the velocity dispersion are computed along the major kinematic axis. However, different from our work, the velocity curve is modelled as an exponential disk. At the small



**Figure C4.** Evolution of the rotational velocity  $v_{\text{rot}} = v_{\text{re}}$  with stellar mass  $\log M_{\star}$  [ $M_{\odot}$ ] (left panel) and SFR (right panel), for the gold (blue squares), silver (gray circles), and unresolved (black dots) samples.

radii probed by the grism data, this curve is similar to the arctangent curve we use, so this should not affect our comparison.

The Sydney/AAO Multi-object Integral-field spectrograph (SAMI; Croom et al. 2012) Galaxy Survey (Allen et al. 2015; Green et al. 2018) is a census of local Universe galaxies, probing both stellar and gas kinematics. The Multi-Unit Spectroscopic Explorer (MUSE; Bacon et al. 2010) samples is presented in (Swinbank et al. 2017) and covers galaxies at redshifts  $0.28 < z < 1.49$ . Both the SAMI and MUSE measurements shown in this work are those presented in Johnson et al. (2018), and are corrected, when necessary, to match measurements for the KROSS sample and provide an accurate comparison. The kinematics for these two samples are both derived from ionised gas.

The SINS/zC-SINF AO survey (Förster Schreiber et al. 2018) is a survey of 35 galaxies at  $z \sim 2$ , probing kinematics and star-formation with  $H\alpha$  and [NII] lines. The rotational velocity is chosen as the maximum observed velocity difference along the kinematic major axis, similar to Wisnioski et al. (2015). An isotropic velocity dispersion  $\sigma_0$  is assumed. (Förster Schreiber et al. 2018) report kinematic measurements consistent with those from the KMOS survey at similar redshifts (Wisnioski et al. 2015; Wuyts et al. 2016b; Übler et al. 2017), and are hence comparable.

The Gassendi  $H\alpha$  survey of SPirals (GHASP; Epinat et al. 2008, 2010) contains Fabry-Perot observations of  $H\alpha$  in 203 local galaxies. For the kinematic modelling, Epinat et al. (2010) a thin planar disk is assumed, and a variety of rotation curves are used based on how well they fit the observed rotation in each system. However, all remain fairly consistent with our arctangent curve within the radii probed in this work. The nature of the data and the modelling approach make a one-to-one comparison difficult, but nonetheless provide an indication of galaxy kinematics in the local Universe.

The Mapping Nearby Galaxies at Apache Point Observatory (MaNGA; Bundy et al. 2015) survey measurements shown for comparison in this work are from Yu et al. (2019). The sample contains spatially resolved  $H\alpha$  measurements for 2716 galaxies in the local Universe. The velocity dispersion is inferred by staking the 1D  $H\alpha$  line from each spaxel and correcting for the instrument resolution and beam smearing.

The de Graaff et al. (2024a) measurements are obtained using the JWST NIRSpec MSA 2D spectra. The assumptions adopted in the kinematic modelling are the same as the ones used in this work. However, the NIRSpec slits suffer from slit-losses, which are described in the paper and accounted for in the forward-modelling of the instrument.

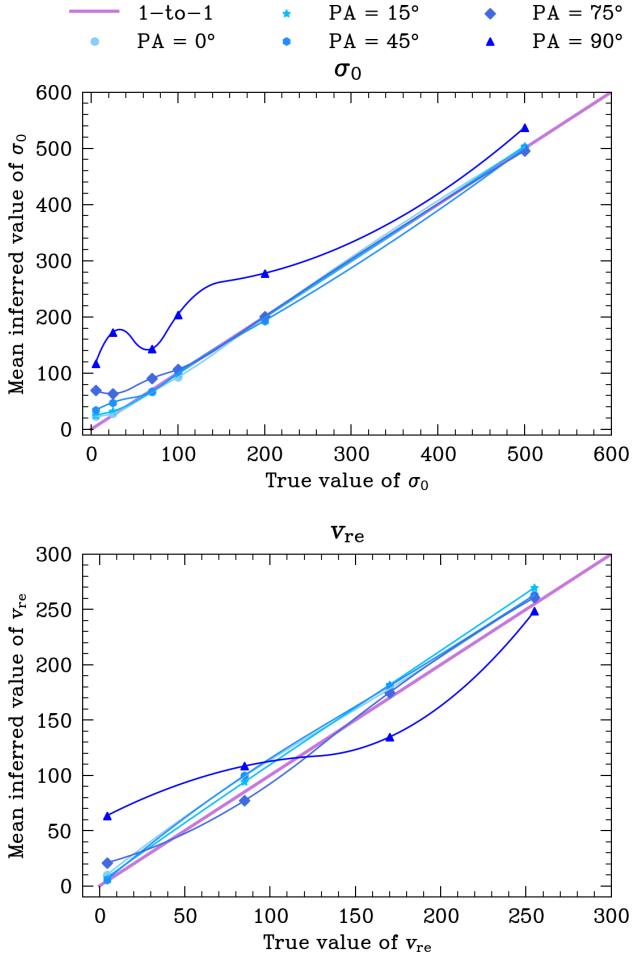
The sample from Parlanti et al. (2023) is selected from the public ALMA data archive and is composed of 22 galaxies at high redshift ( $4.2 < z < 7.6$ ). The galaxies are observed in the [CII] or [OIII] emission lines, or both. The rotational velocity is modelled using a bulge component and an exponential disk component. The rotational velocity is defined as the maximum observed velocity, which is typically higher than the velocity measured at  $r_e$ , as previously discussed. The cold gas measurements from the [CII] emission line have lower velocity dispersions on average, as shown in (Parlanti et al. 2023), than measurements from ionised gas ([OIII] and  $H\alpha$ ).

We also compare our results with predictions from the TNG simulations (Pillepich et al. 2019), where they compute kinematic properties in the following way. The rotational velocity  $v_{\text{rot}}$  is the absolute maximum of a galaxy’s rotation curve along its structural major axis, from its edge-on projection and within twice the stellar half-mass radius. The dispersion  $\sigma_0$  is the value of the velocity dispersion from a face-on projection of a galaxy, averaged in pixels of 0.5 ckpc a side that lie along the structural major axis and between one and two the stellar half-mass radius.

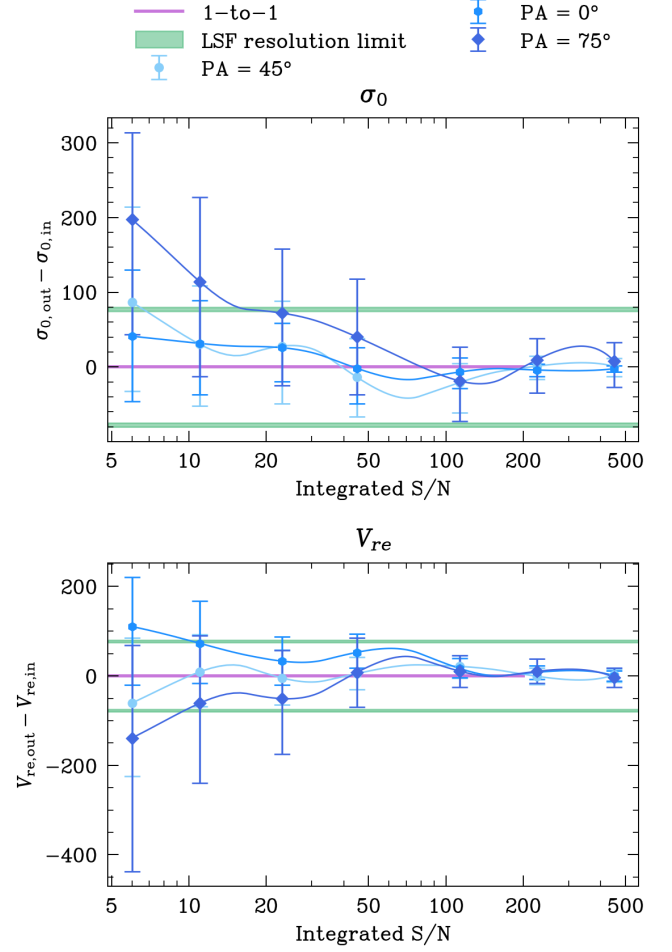
We do not discuss the cold gas local Universe measurements as they are only shown in Fig. 7 to compare to local Universe measurements of ionised gas (for further details, see Übler et al. 2019).

## APPENDIX F: GOLD SAMPLE FITS

Here we present the GEKO summary plot, which shows the best-fit model compared to the grism data, of all of the objects in the gold sample, whose properties are summarized in Tab. A3. For a full description of the structure of this plot see Sec. 3.4 and Fig. 4. We note that hot or dead pixels are masked in the fitting process, but not in the summary plots.

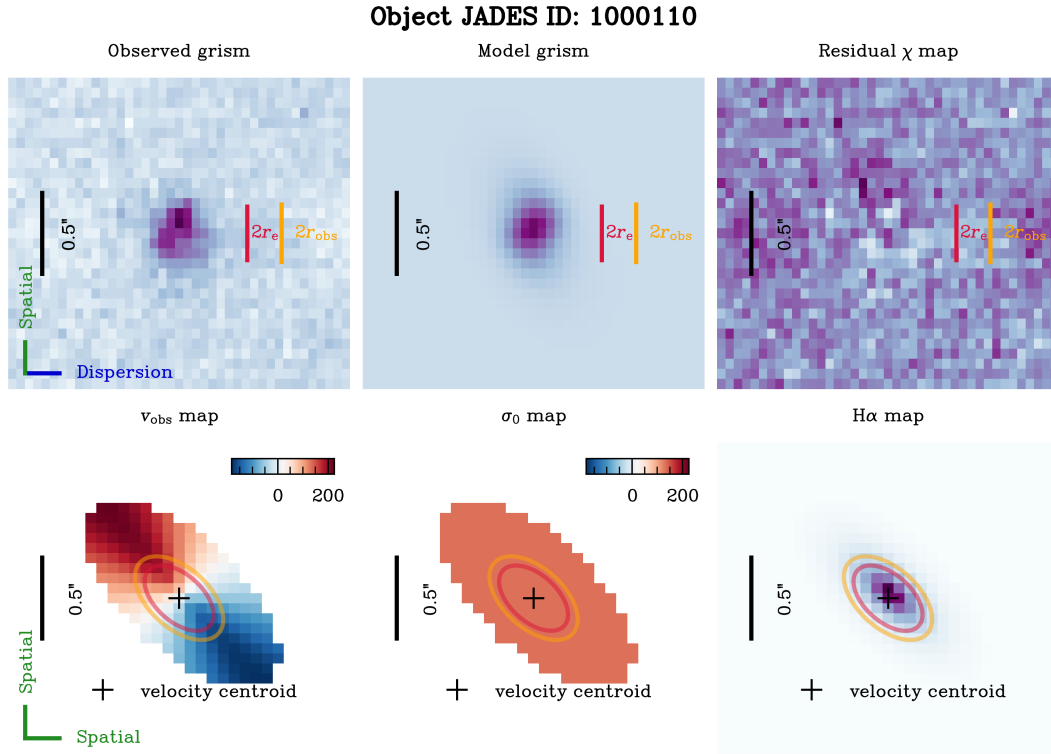


**Figure D1.** Results of recovery tests for  $\sigma_0$  (top panel) and  $v_{re}$  (bottom panel), for mock galaxies with a range of position angles  $PA = 0 - 90^\circ$ . The mean values are computed by averaging over tests done with a range of rotational velocities  $v_{re} = 5 - 250$  km/s, for  $\sigma_0$ , and velocity dispersions  $\sigma_0 = 5 - 500$  km/s, for  $v_{re}$ .

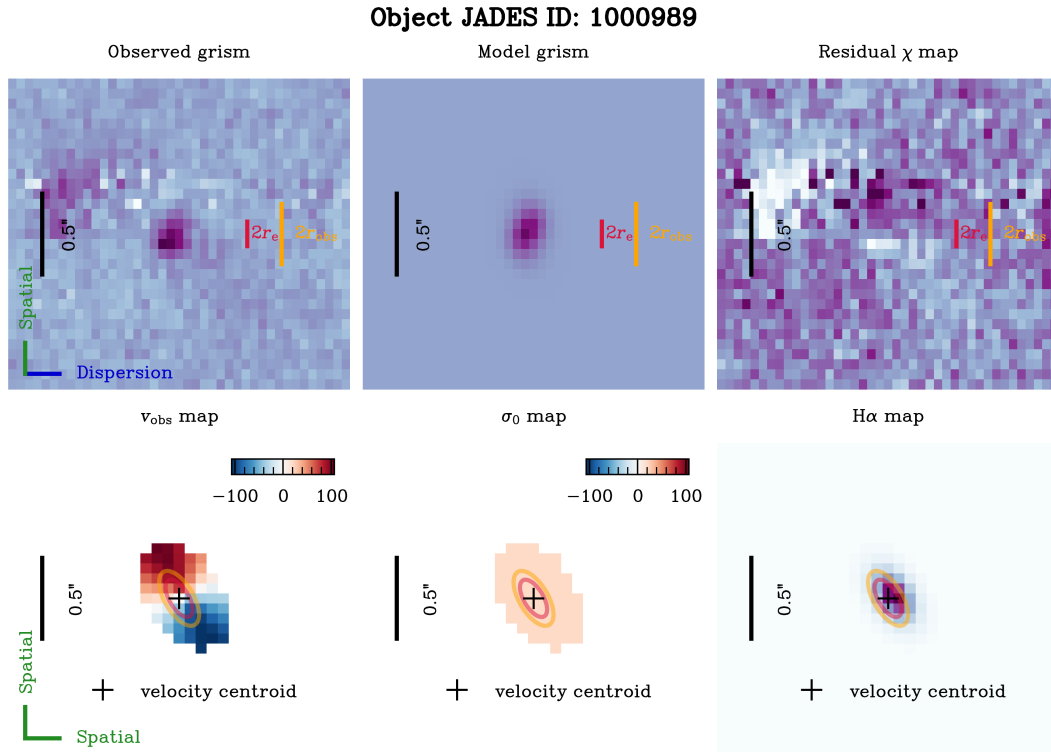


**Figure D2.** Results of recovery tests for  $\sigma_0$  (top panel) and  $v_{re}$  (bottom panel) for integrated  $S/N = 6 - 500$ . The mock galaxy has  $\sigma_0 = 100$  km/s and  $v_{re} \approx 170$  km/s.

This paper has been typeset from a  $\text{\TeX}/\text{\LaTeX}$  file prepared by the author.



**Figure F1.** GEKO summary plots for the objects in the gold sample. The JADES ID for each object is marked at the top. The left-hand panel shows the residuals of the model with respect to the observed grism, along with the best-fit velocity, velocity dispersion, and intrinsic emission maps. For a full description of the structure of this plot see Sec. 3.4 and Figs.4.



**Figure F1.** Continued.

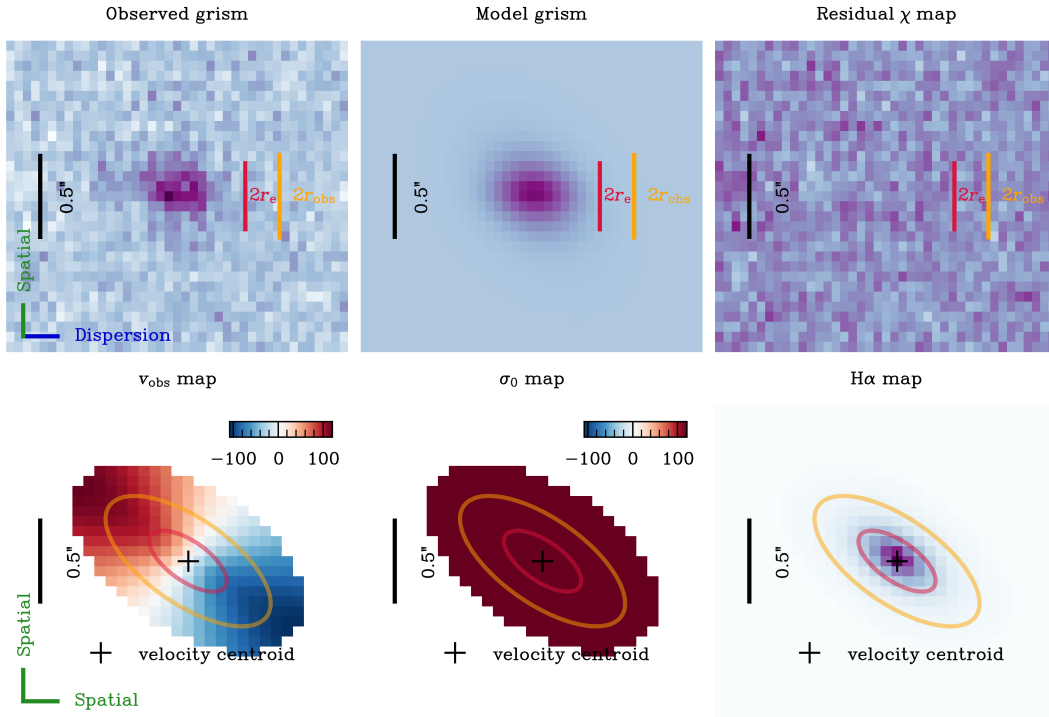
**Object JADES ID: 1001674**


Figure F1. Continued.

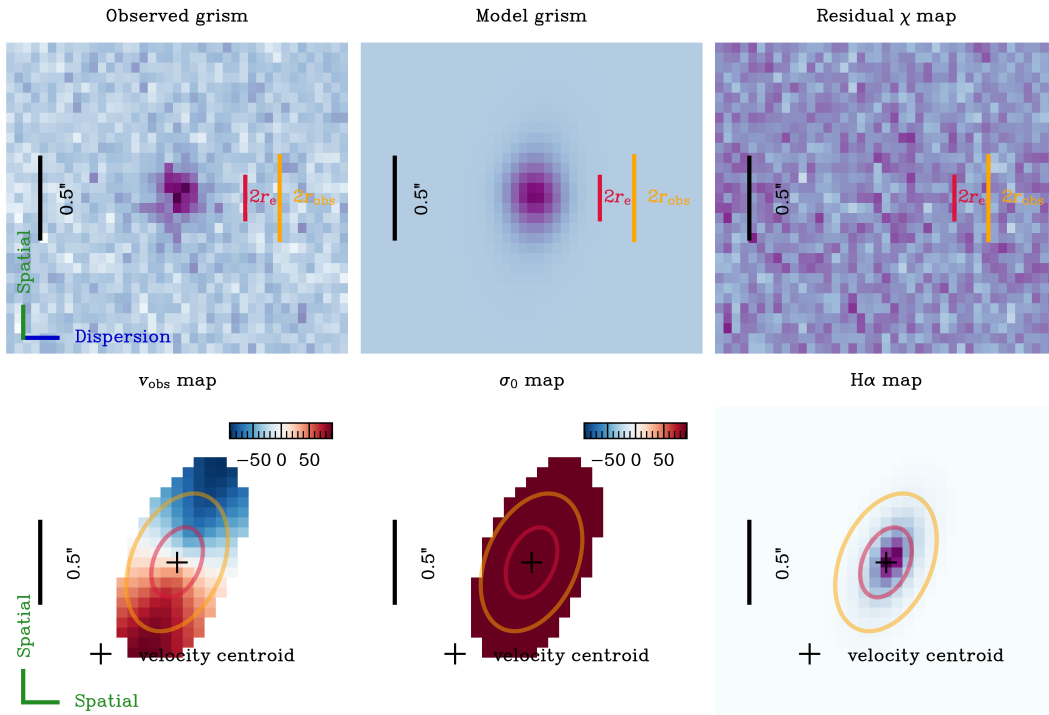
**Object JADES ID: 1002030**


Figure F1. Continued.

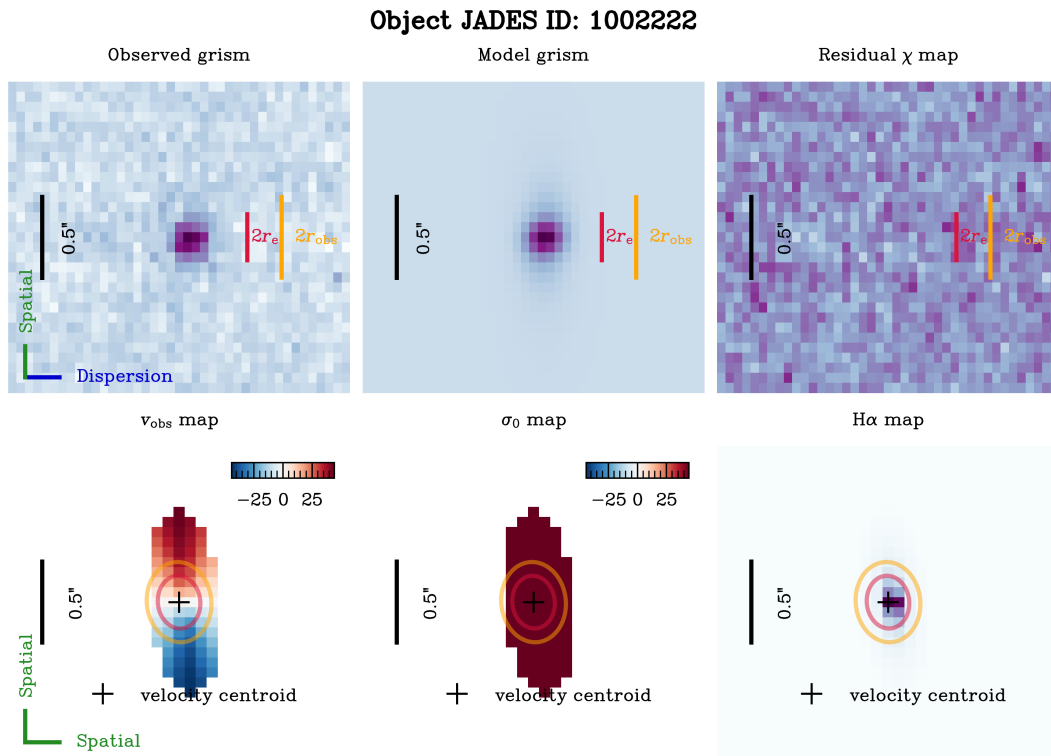


Figure F1. Continued.

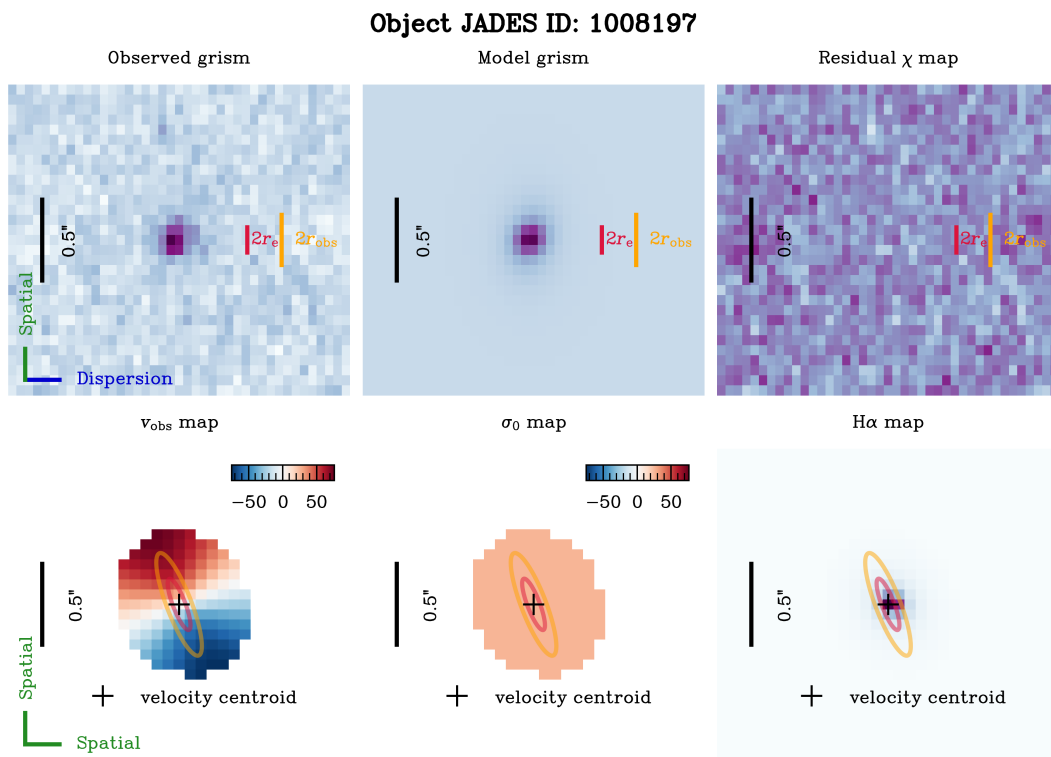


Figure F1. Continued.

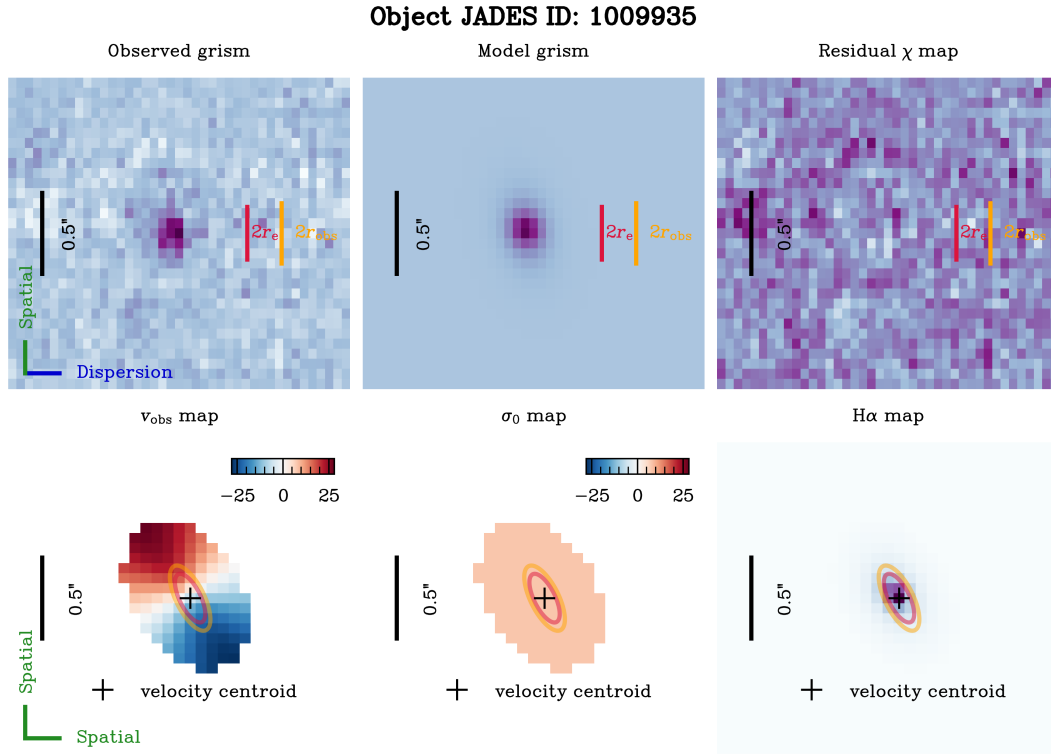


Figure F1. Continued.

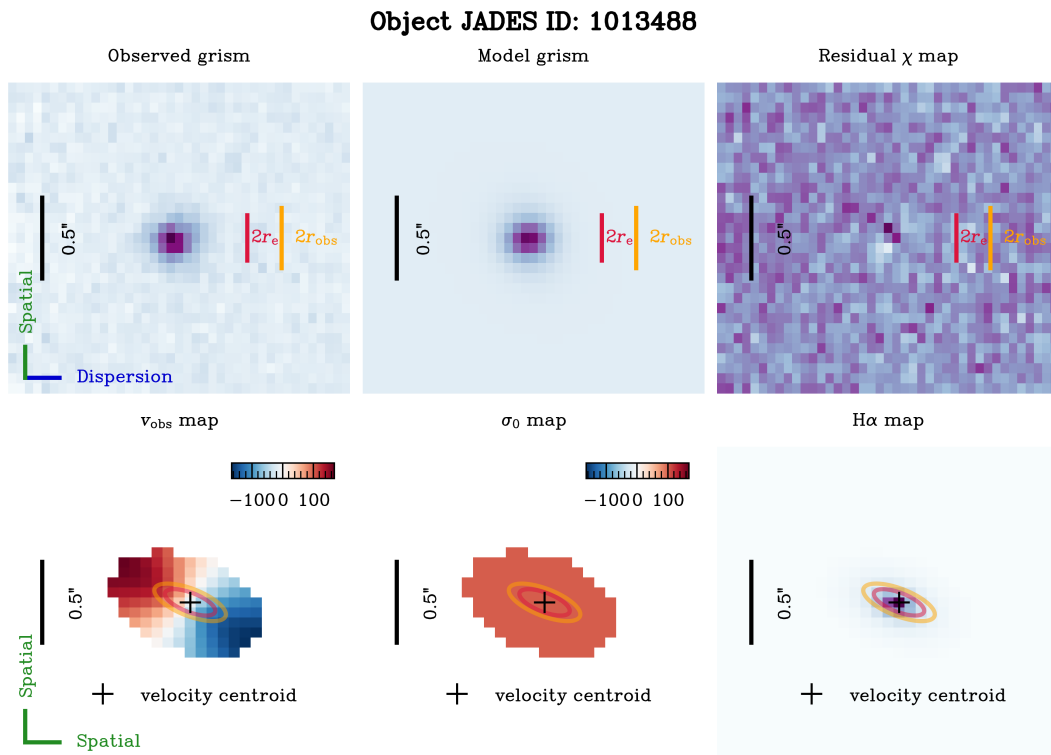


Figure F1. Continued.

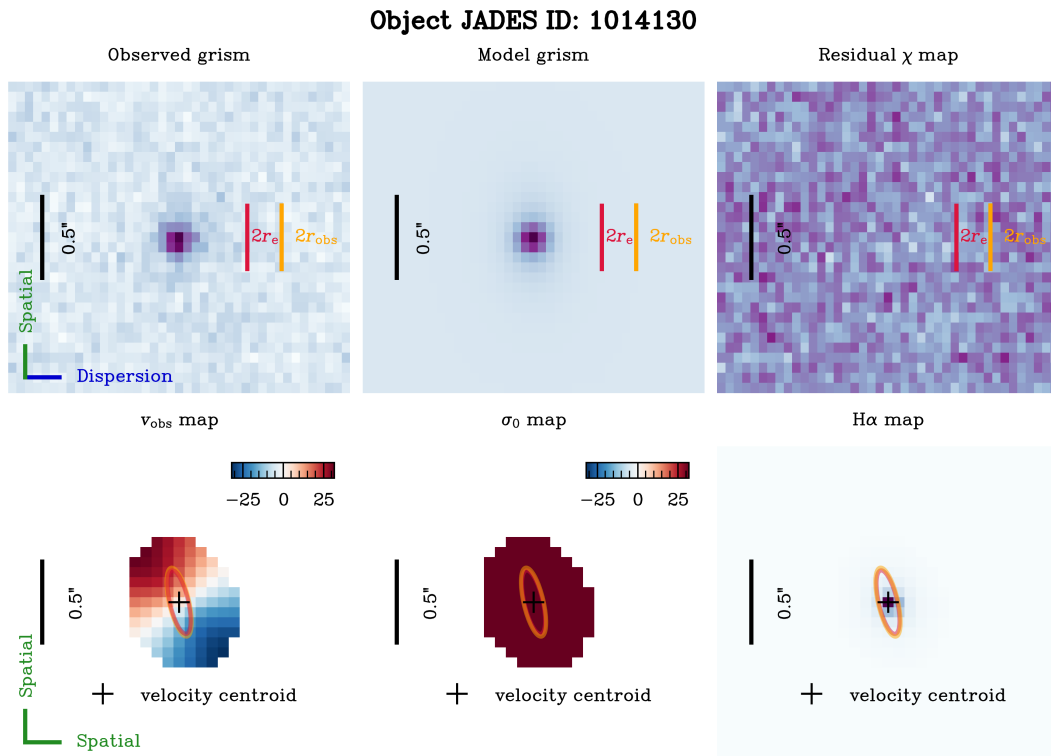


Figure F1. Continued.

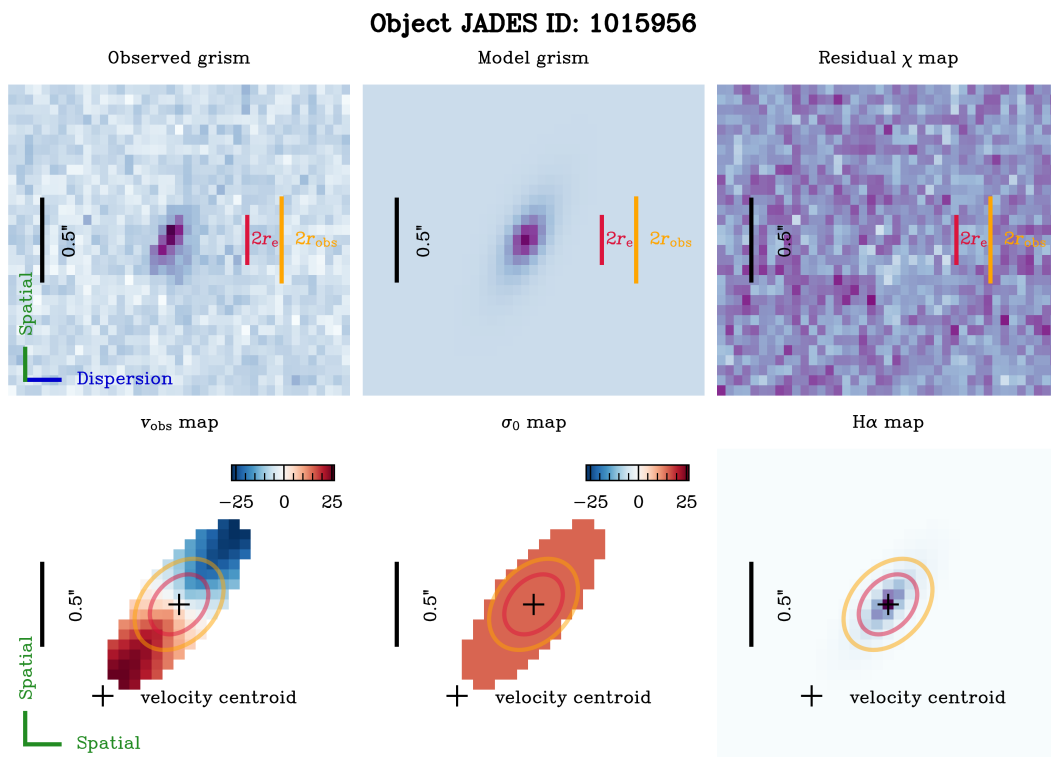


Figure F1. Continued.



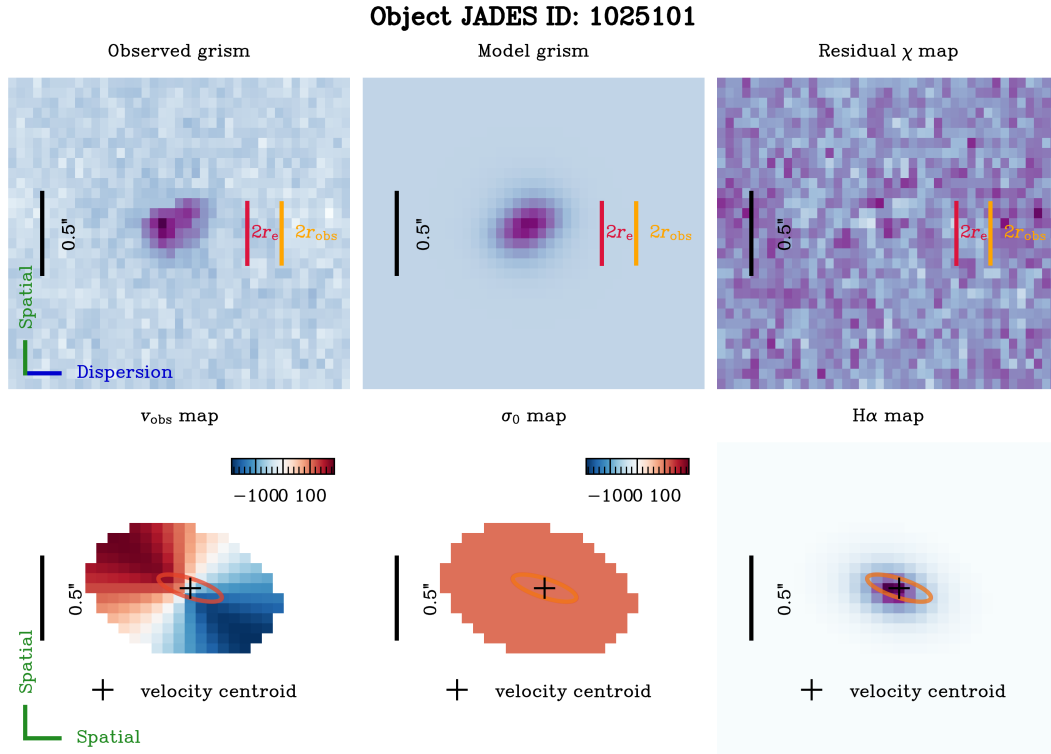


Figure F1. Continued.

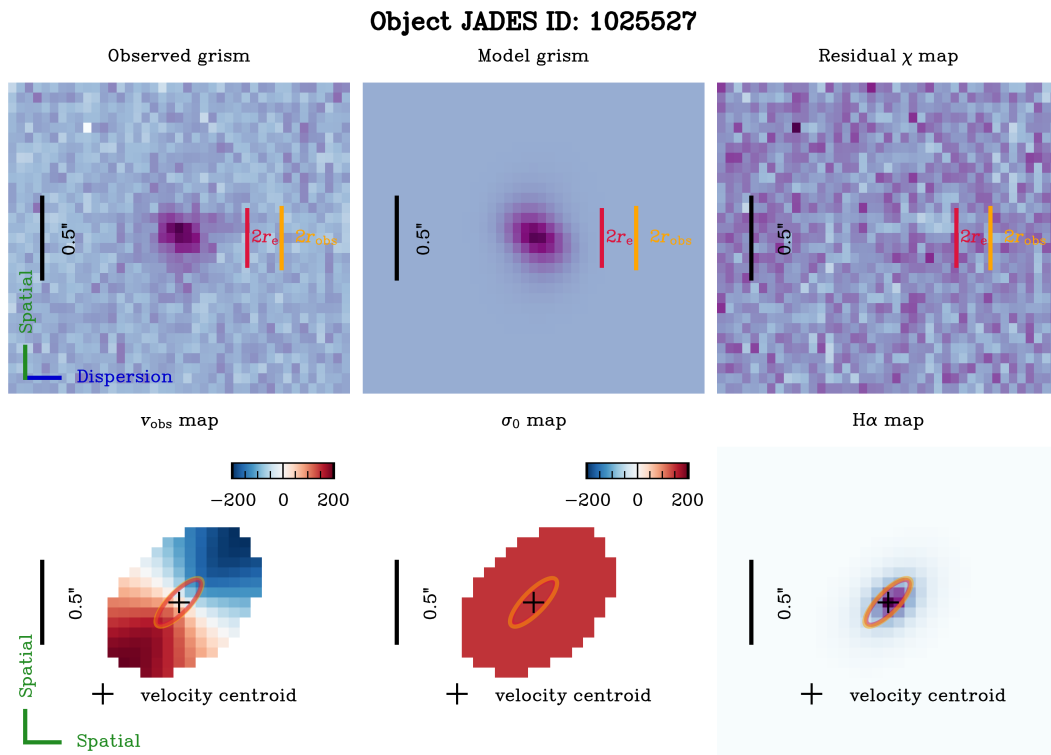


Figure F1. Continued.

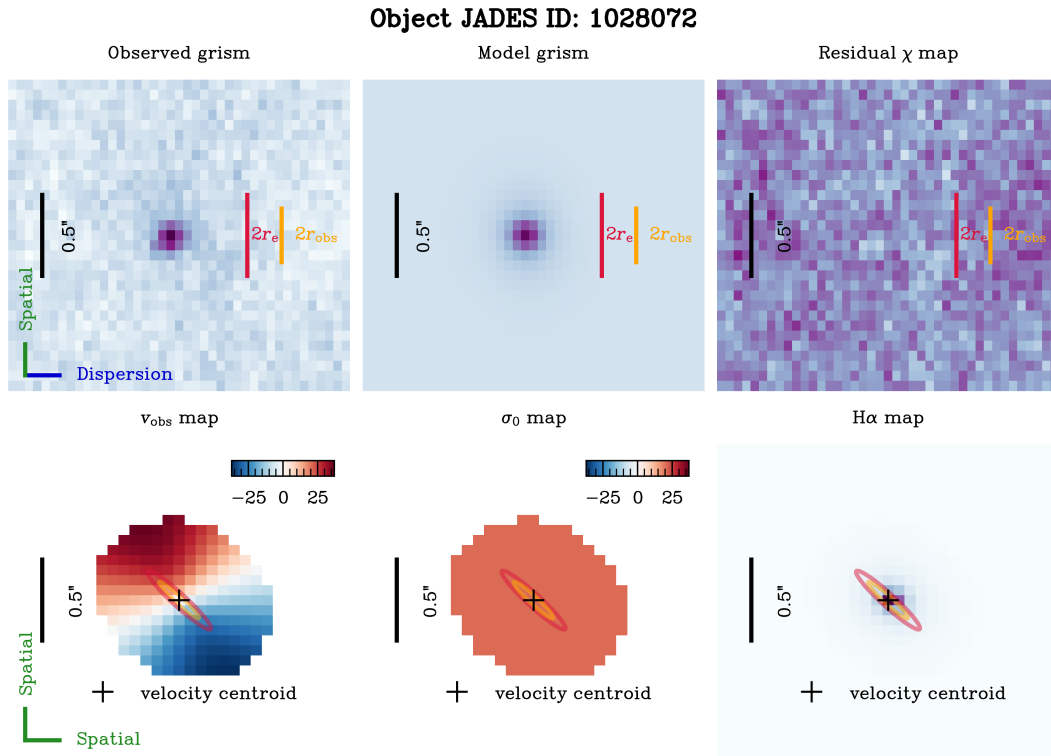


Figure F1. Continued.

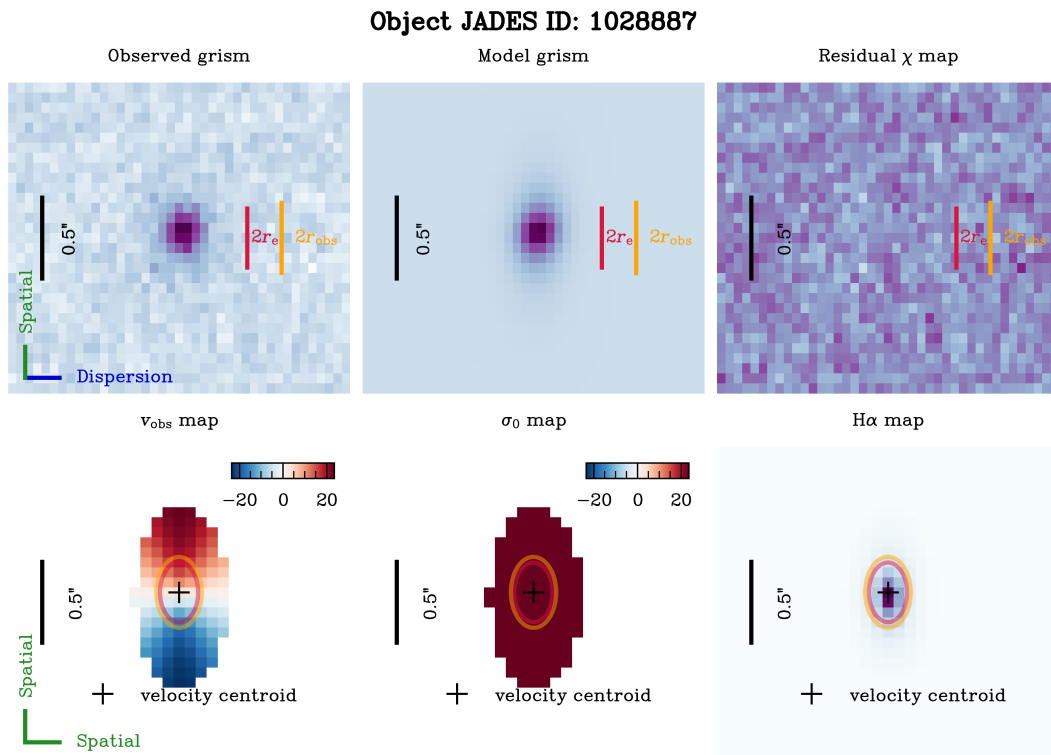
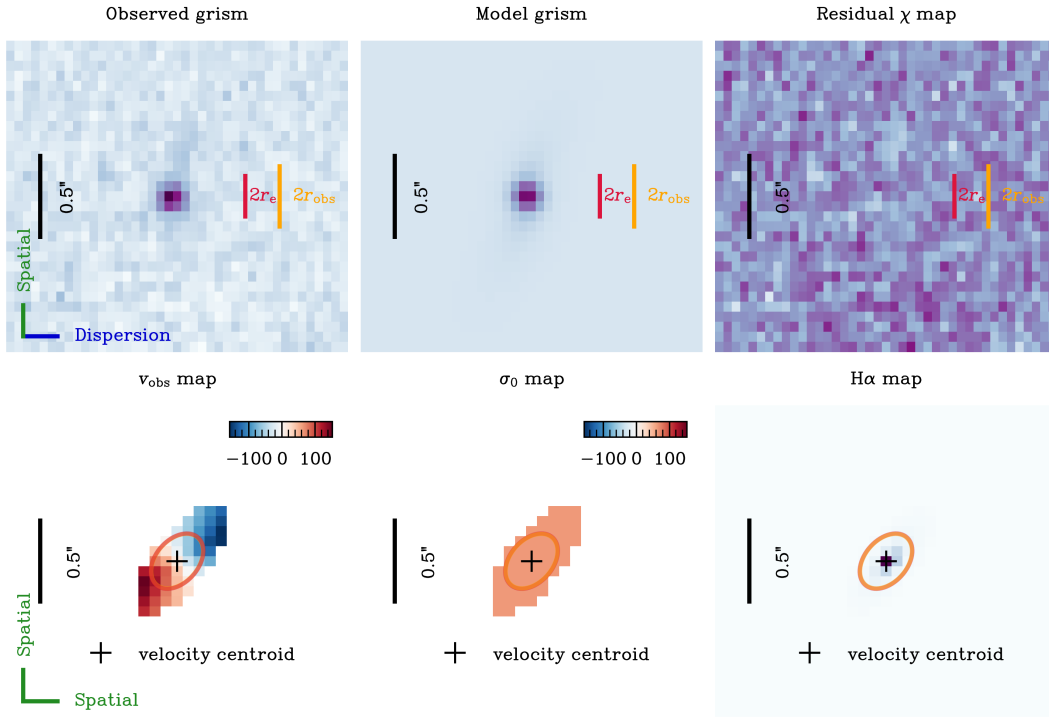
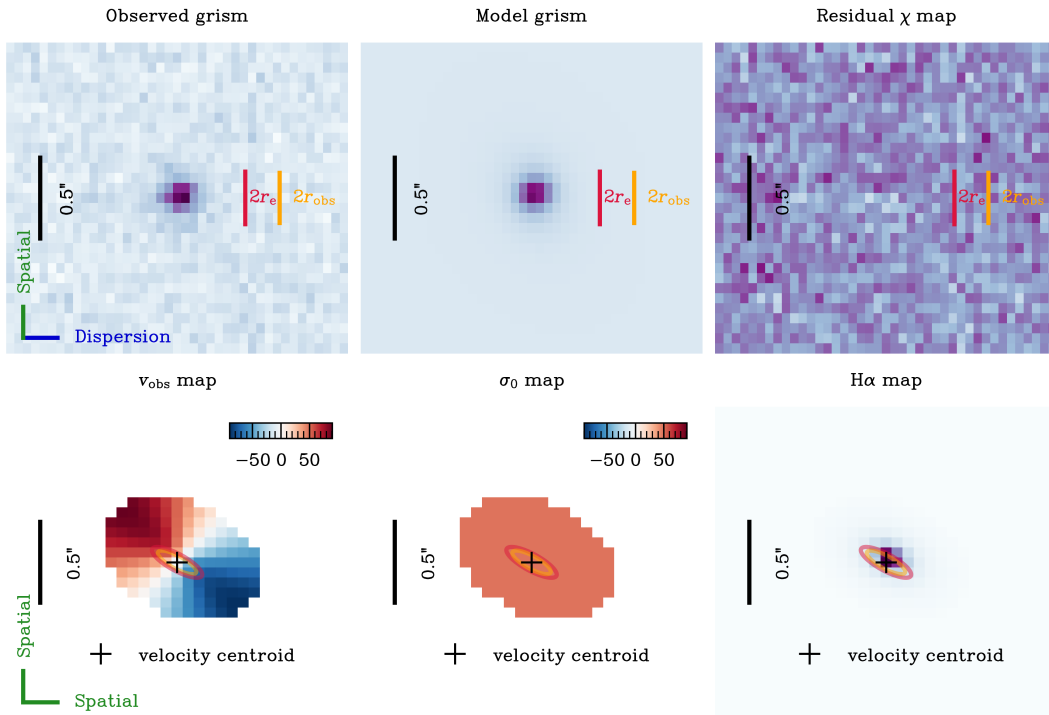
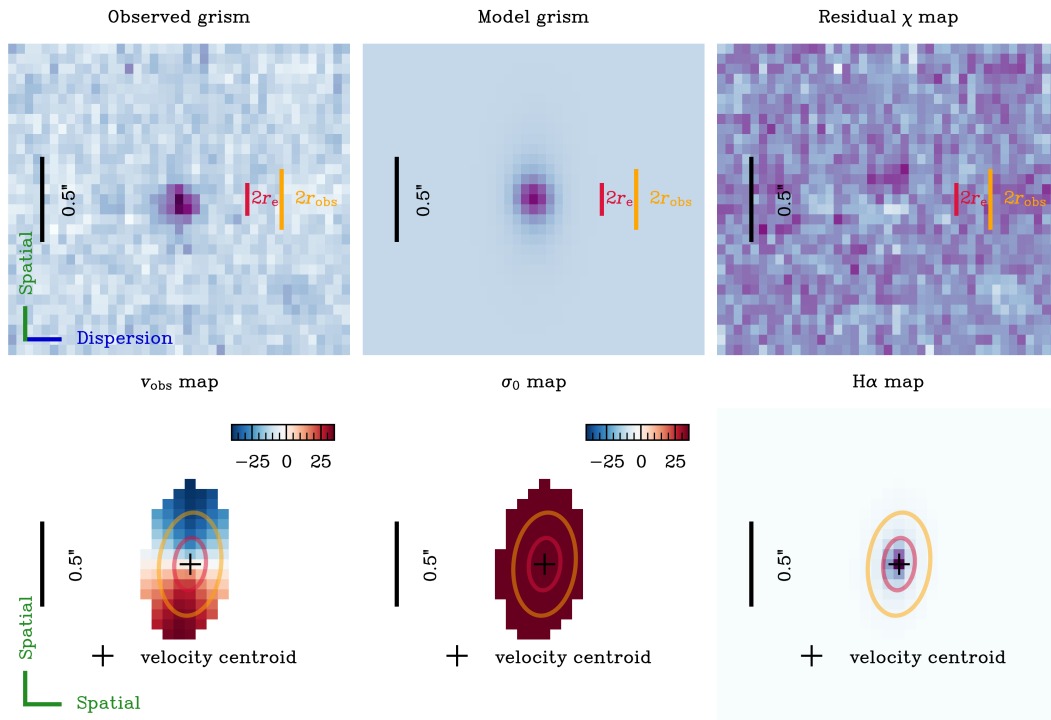


Figure F1. Continued.

**Object JADES ID: 1029814**

**Figure F1.** Continued.

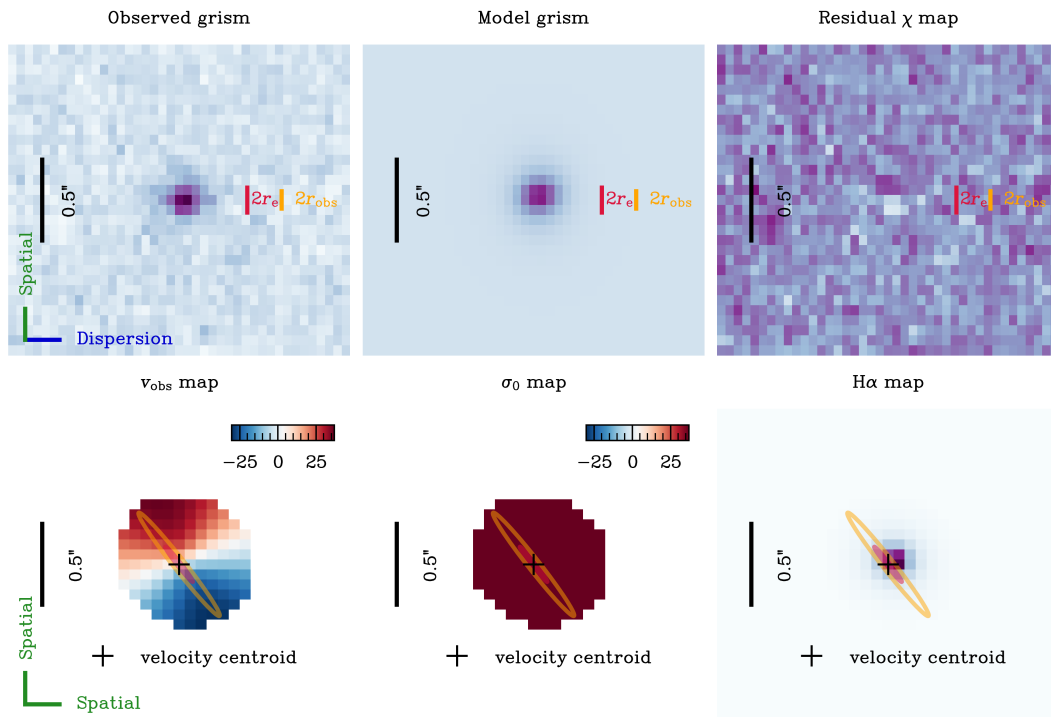
**Object JADES ID: 1065488**

**Figure F1.** Continued.

**Object JADES ID: 1077261**



**Figure F1.** Continued.

**Object JADES ID: 1077545**



**Figure F1.** Continued.

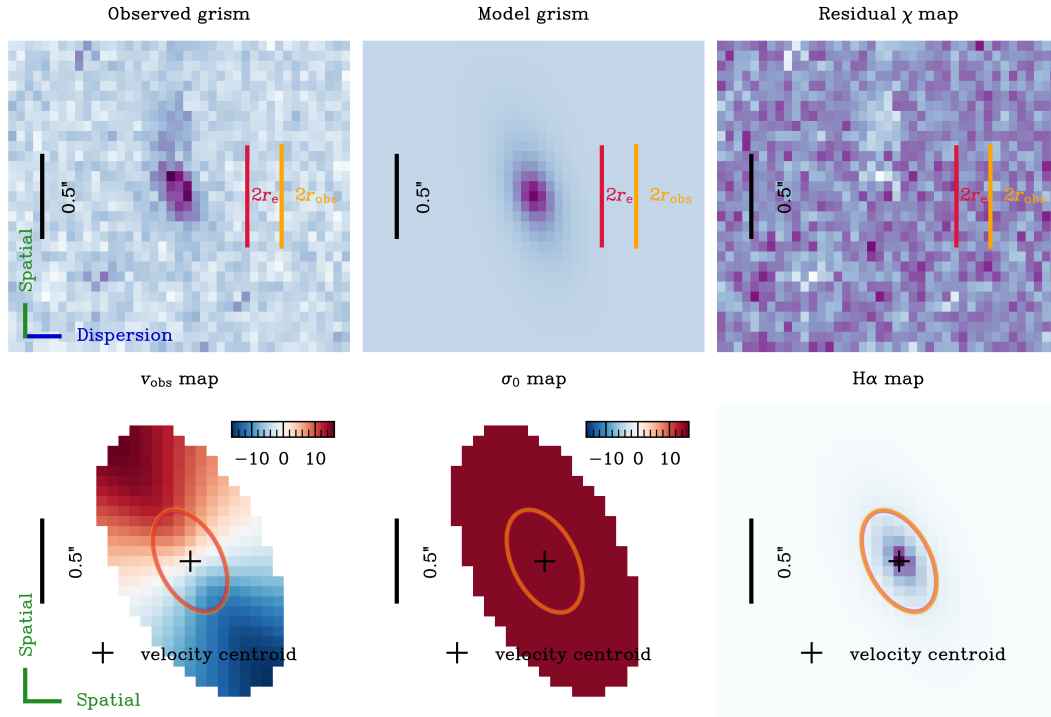
**Object JADES ID: 1079264**


Figure F1. Continued.

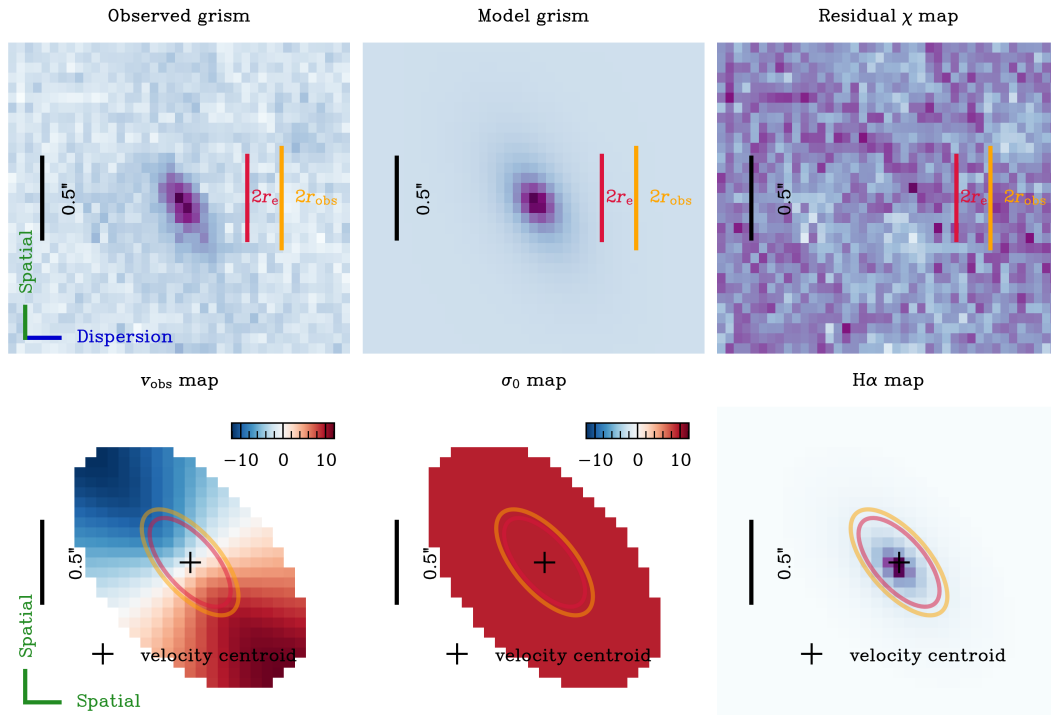
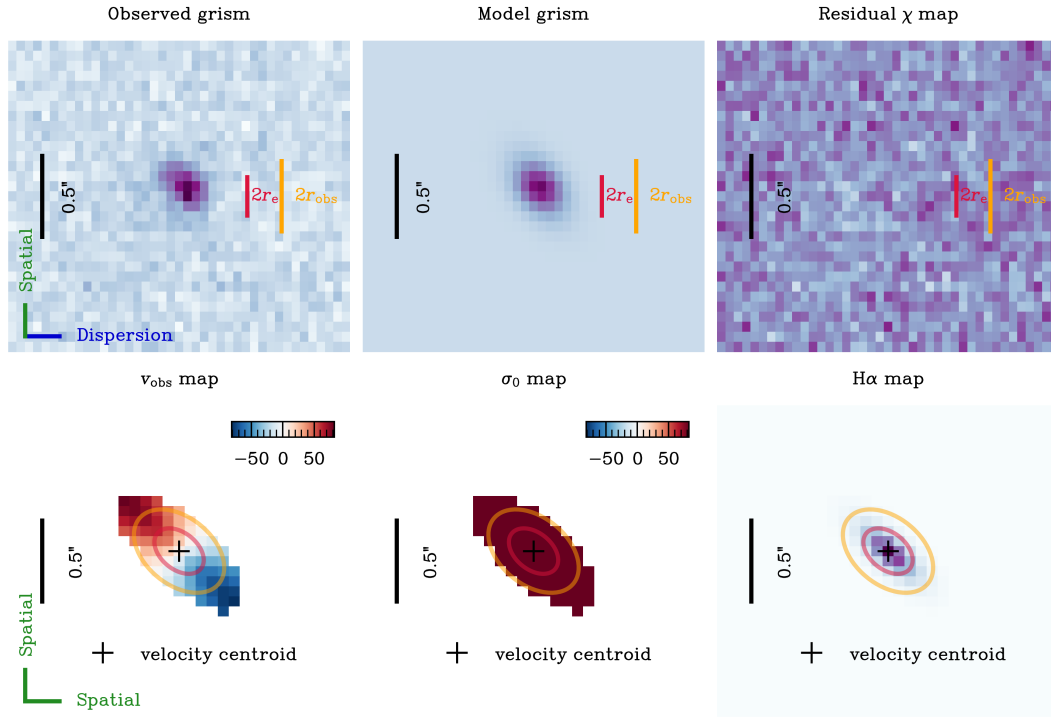
**Object JADES ID: 1082948**


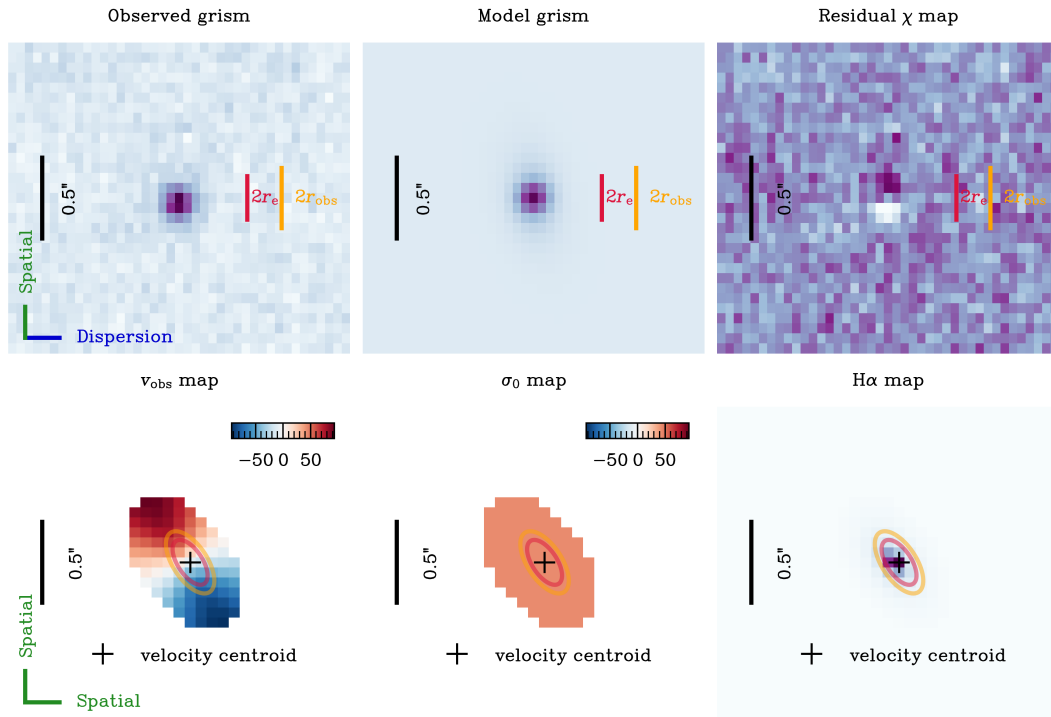
Figure F1. Continued.

**Object JADES ID: 1083165**

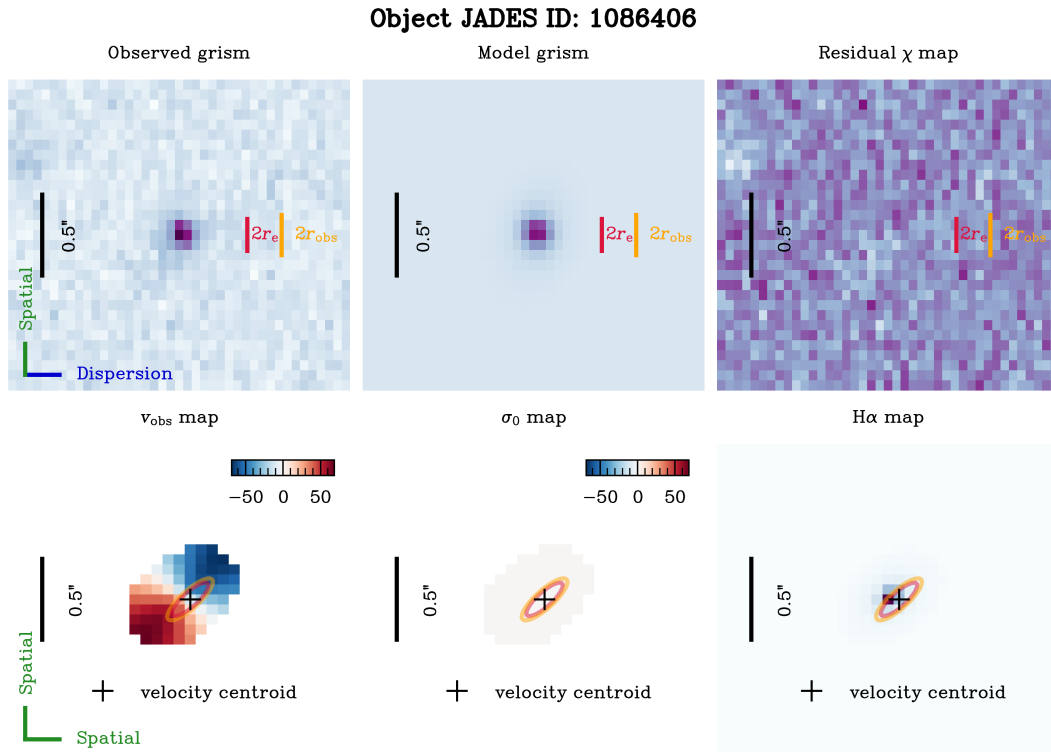
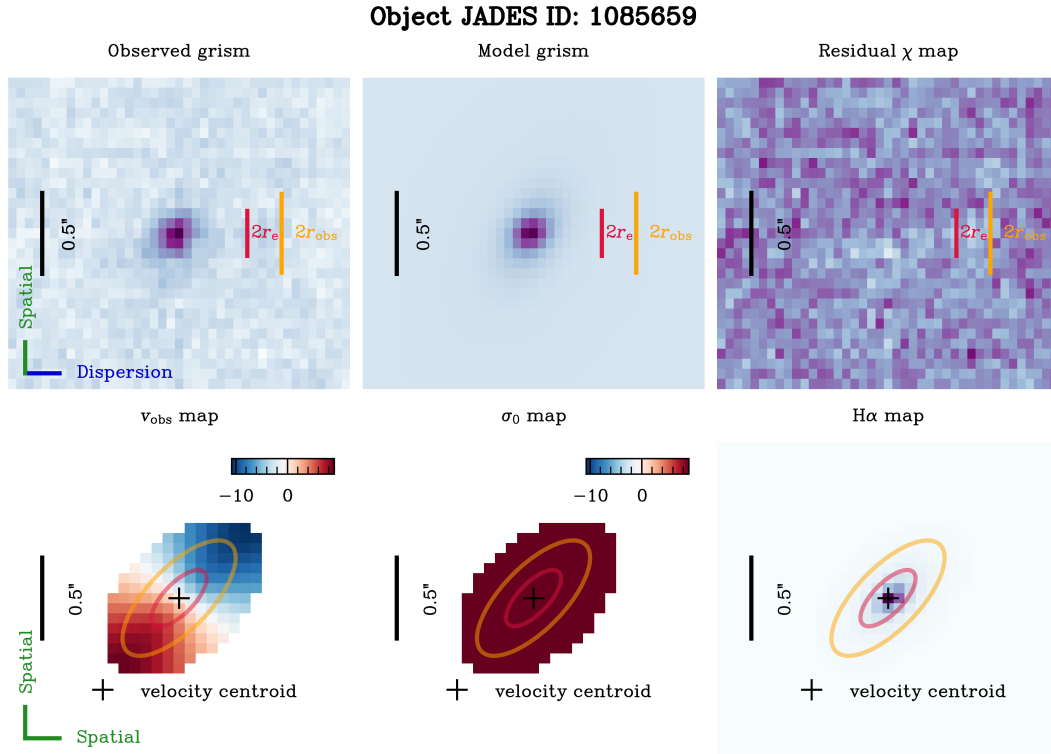


**Figure F1.** Continued.

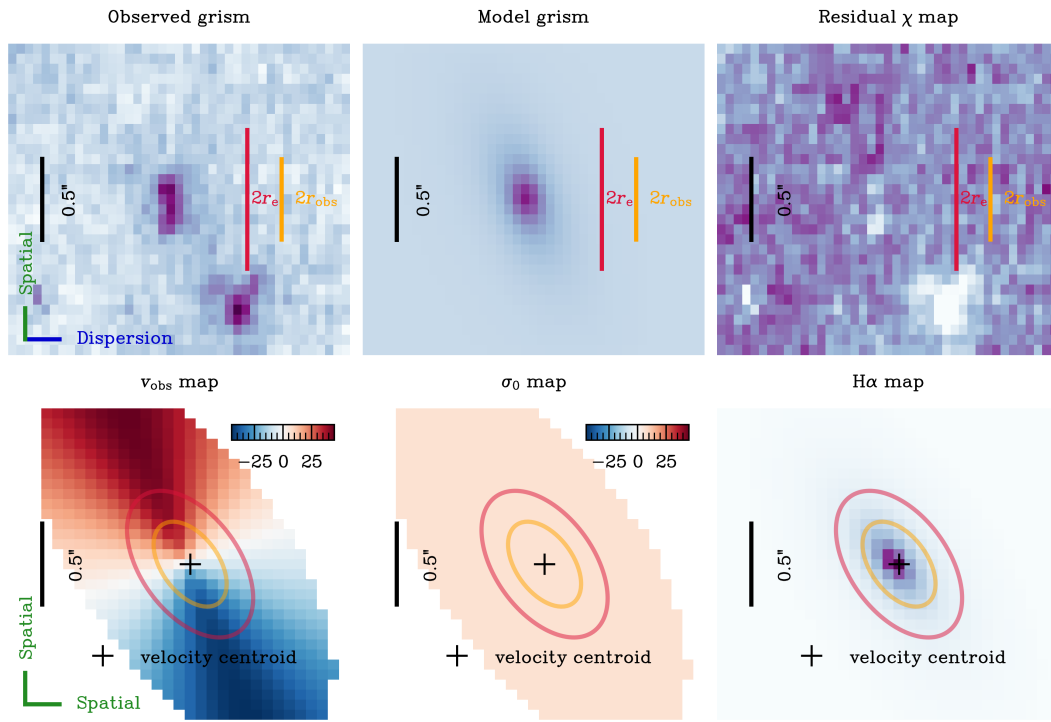
**Object JADES ID: 1085494**



**Figure F1.** Continued.

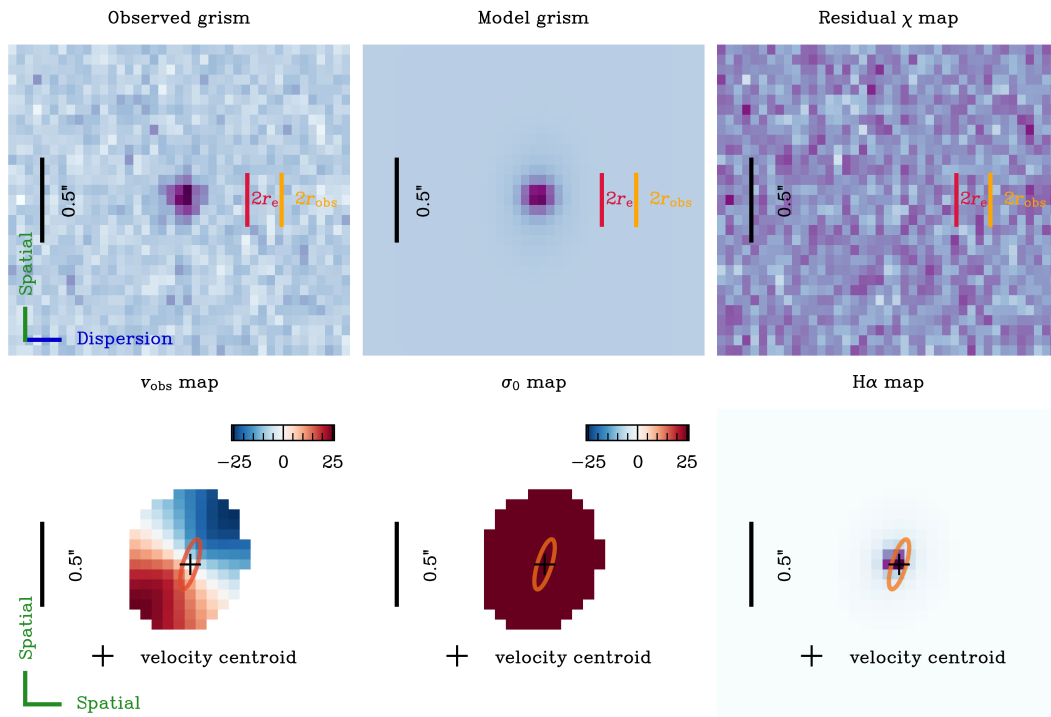


**Object JADES ID: 1086992**



**Figure F1.** Continued.

**Object JADES ID: 1087148**



**Figure F1.** Continued.



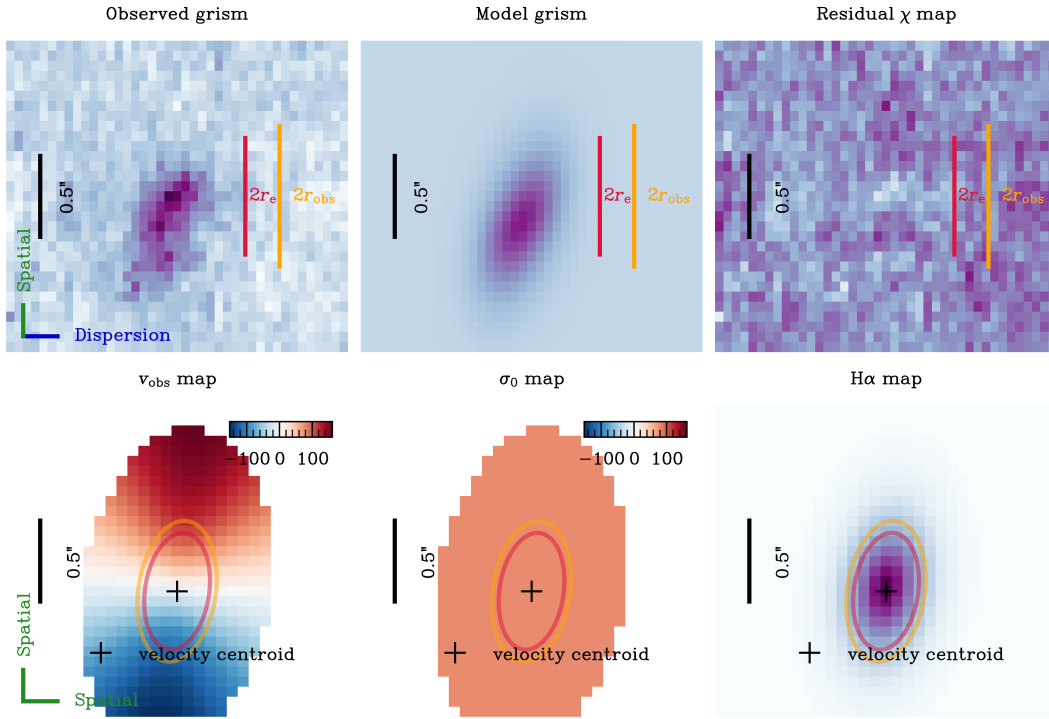
**Object JADES ID: 1088814**


Figure F1. Continued.

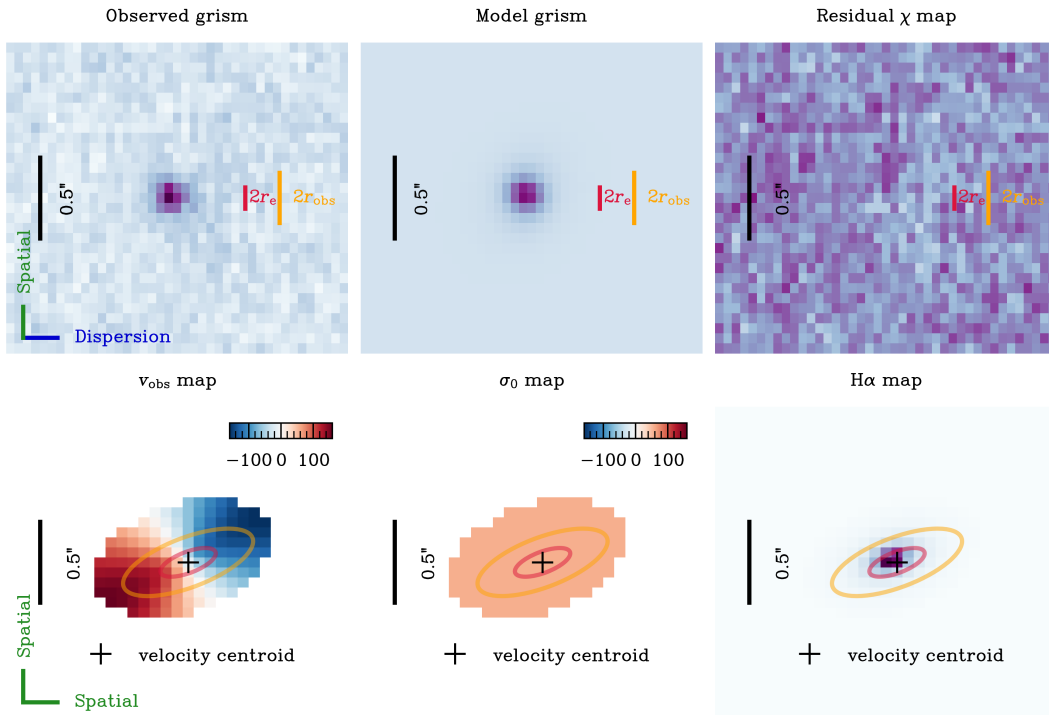
**Object JADES ID: 1089583**


Figure F1. Continued.

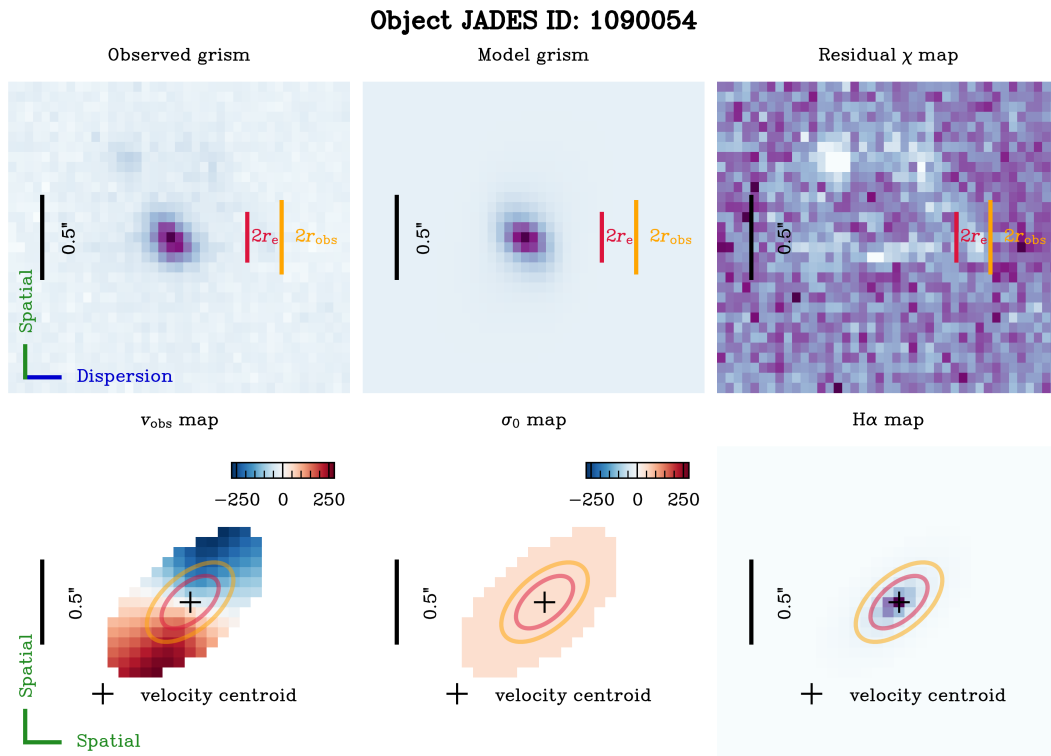


Figure F1. Continued.

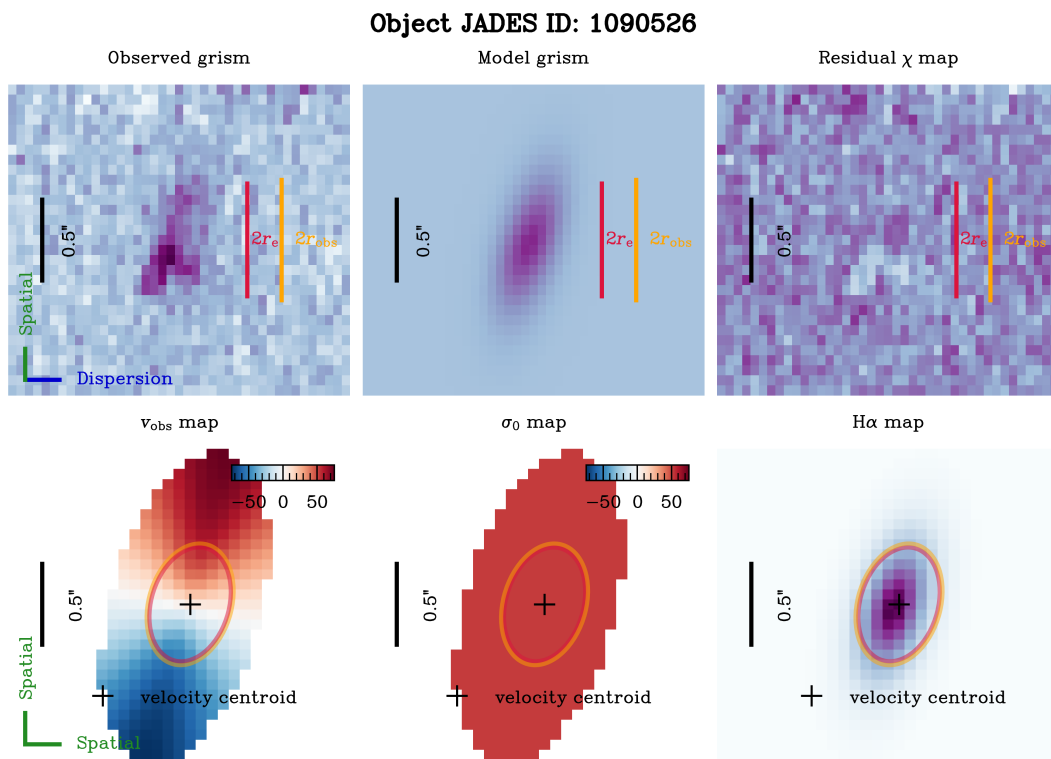


Figure F1. Continued.

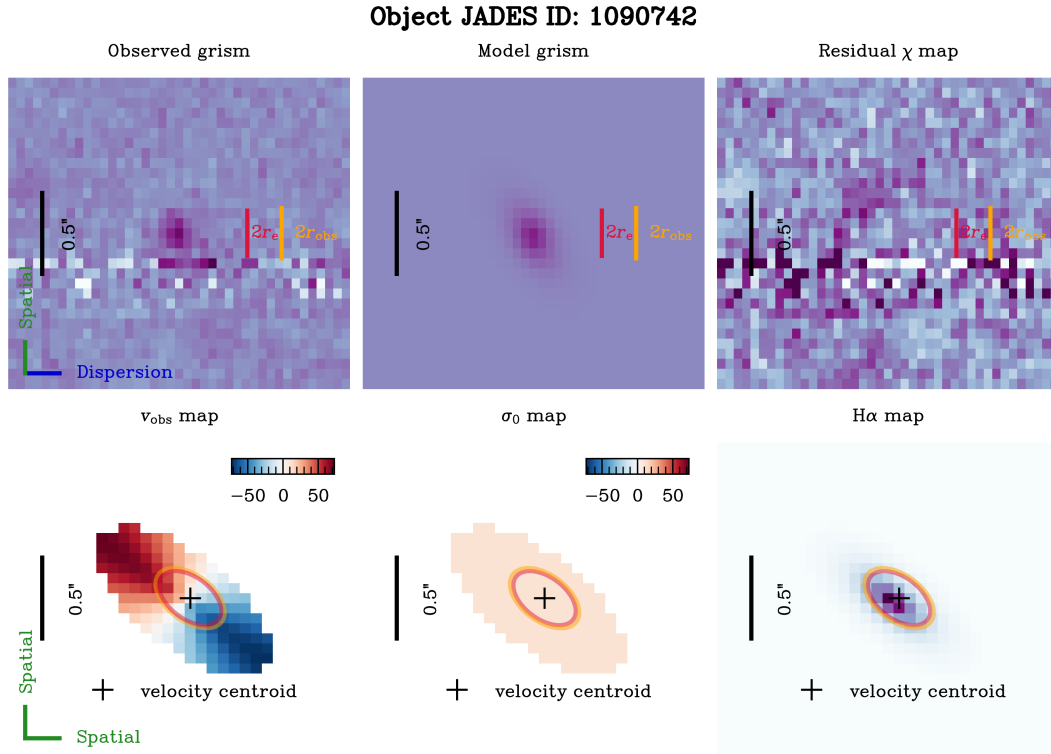


Figure F1. Continued.

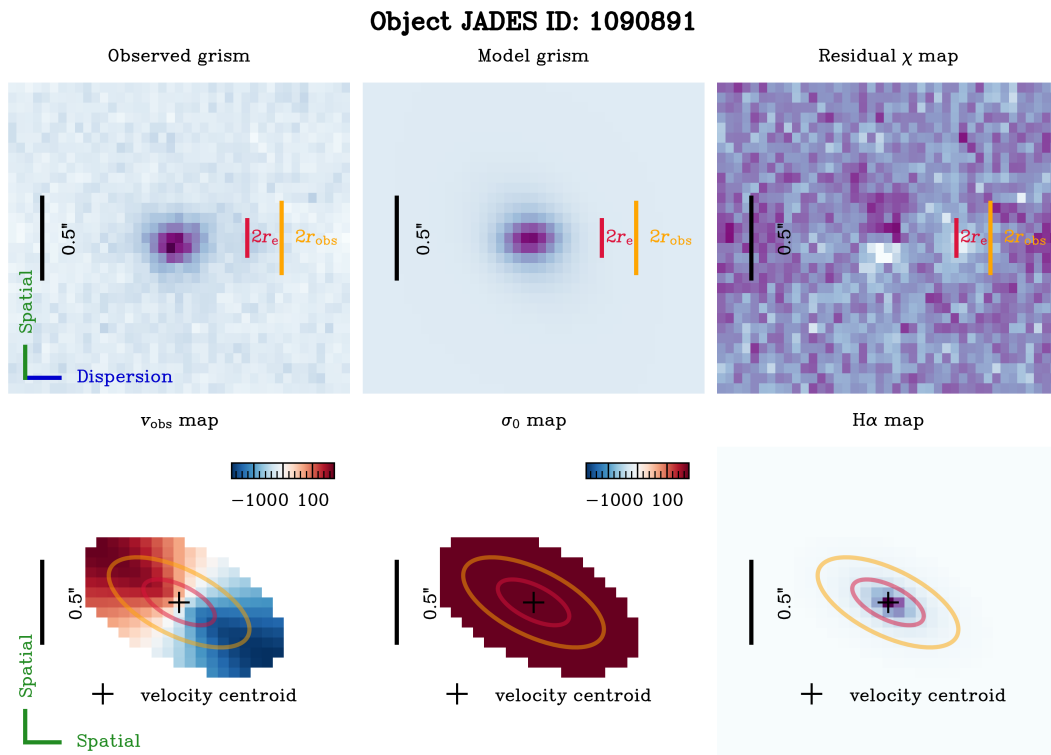


Figure F1. Continued.

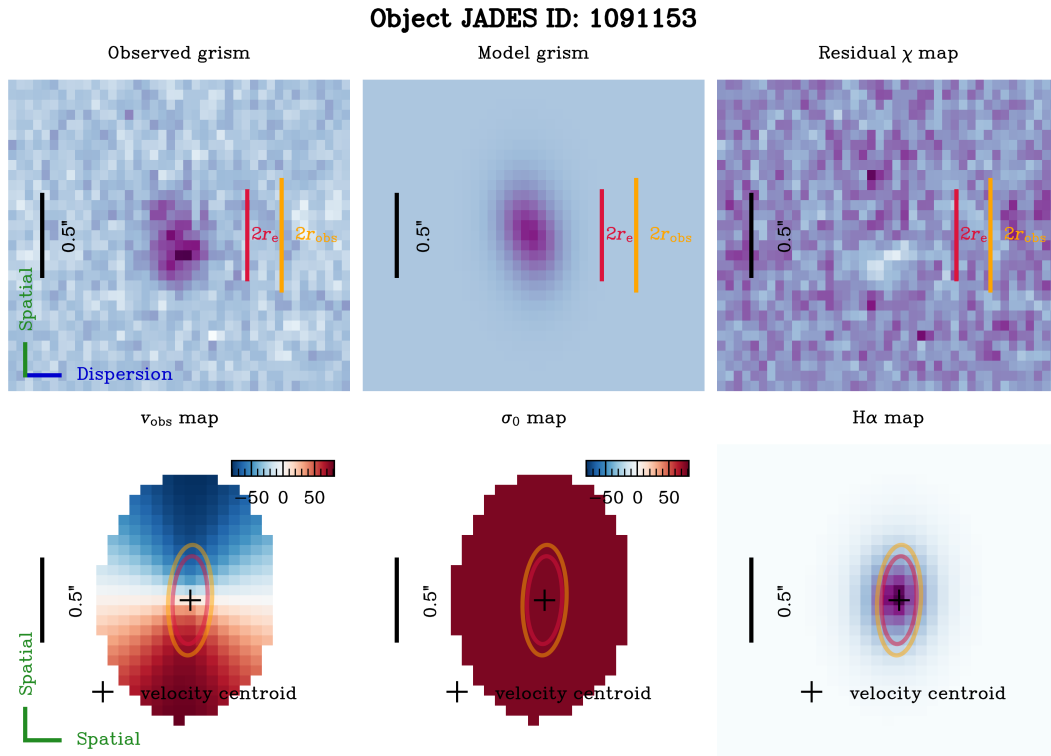


Figure F1. Continued.

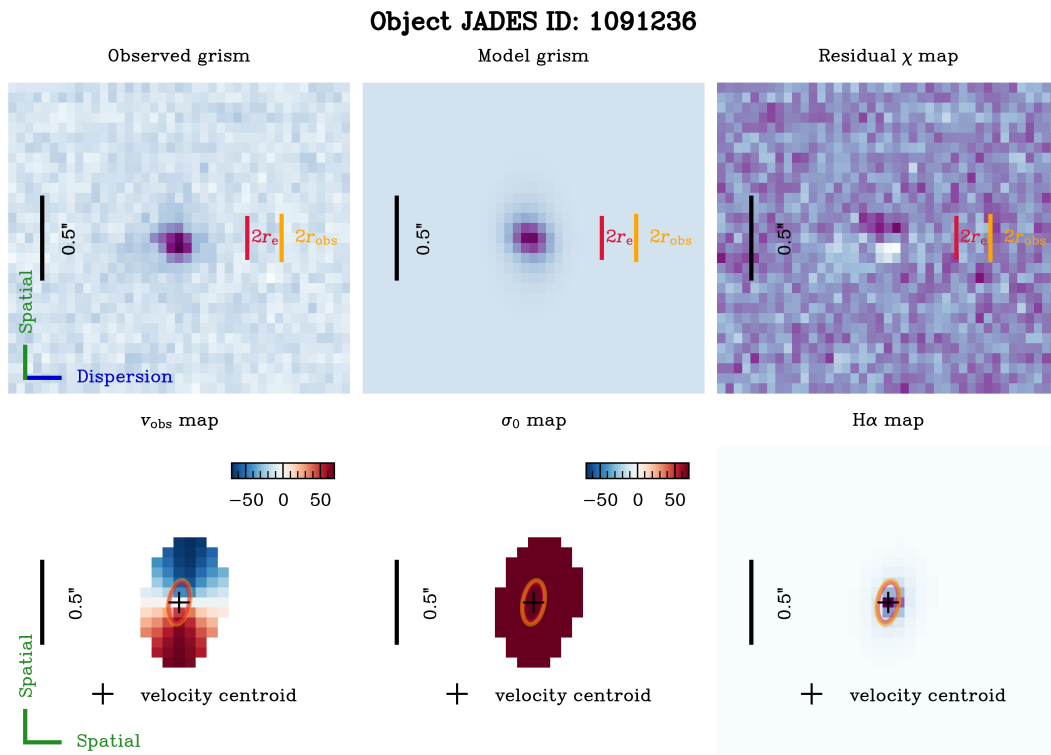
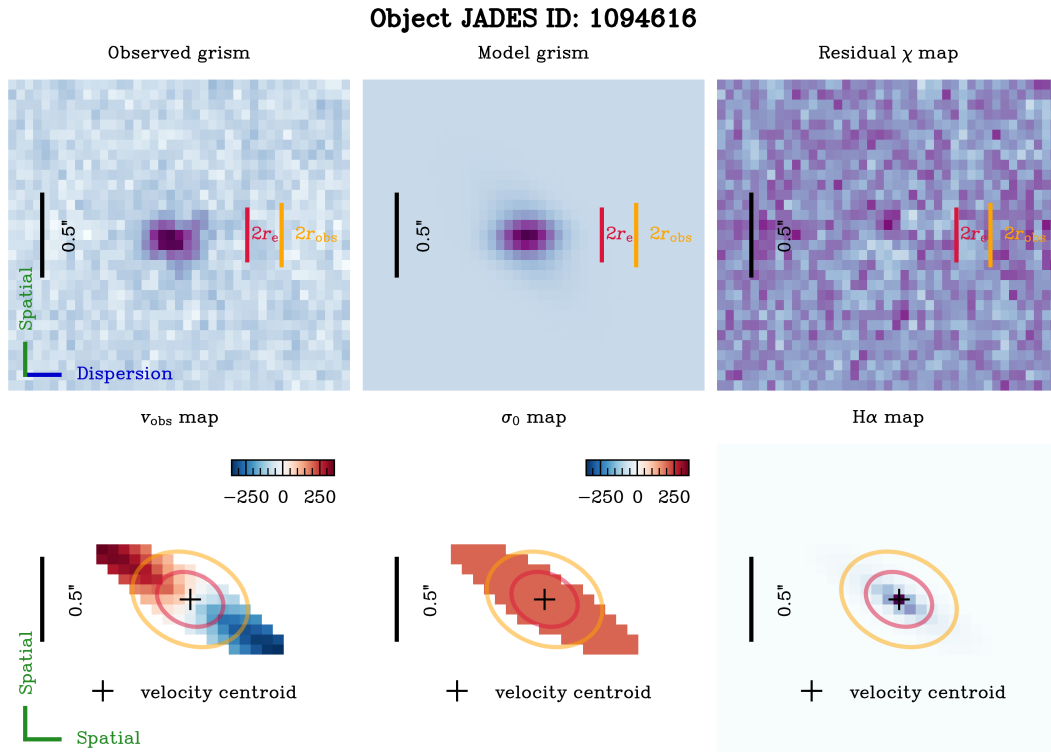
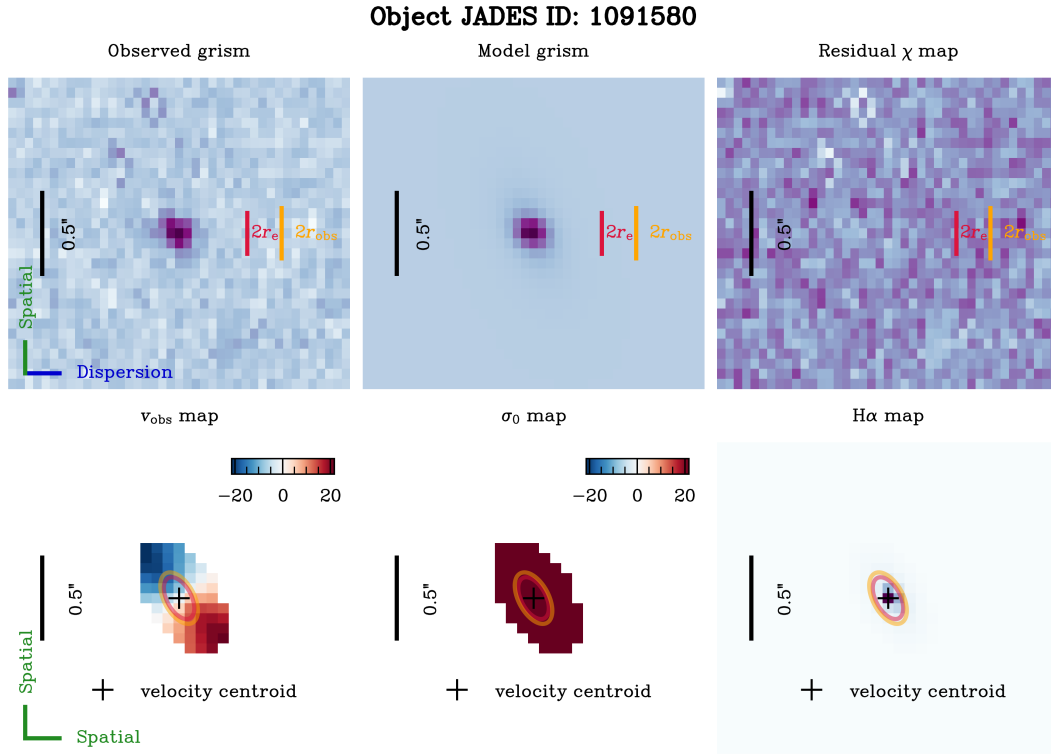
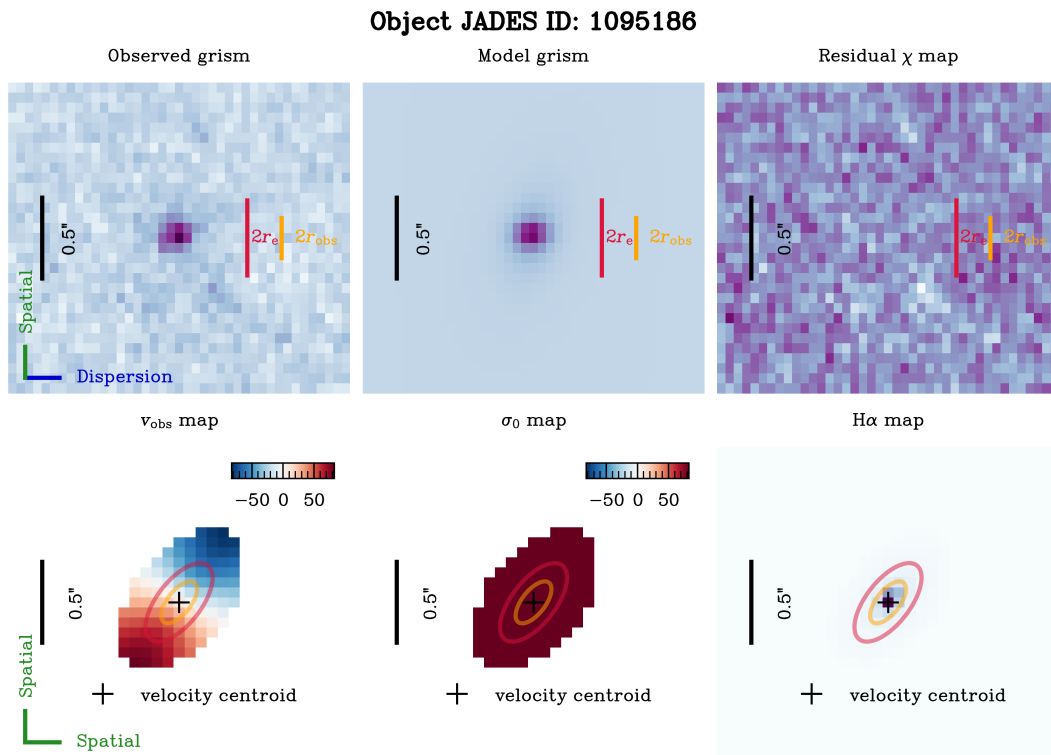
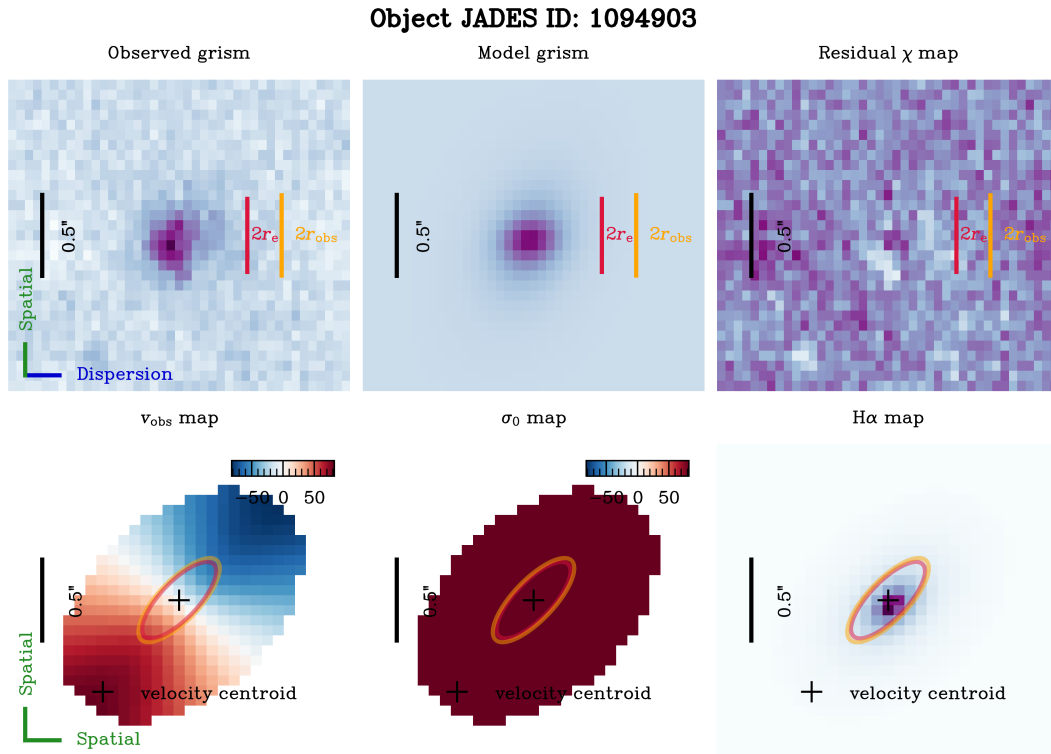


Figure F1. Continued.





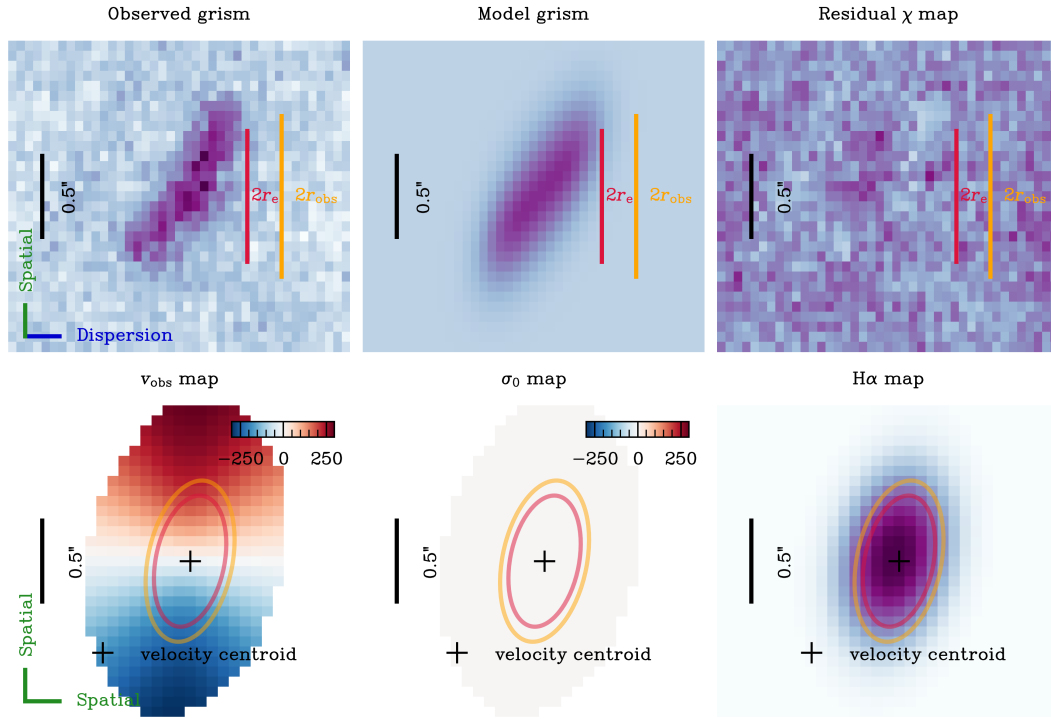
**Object JADES ID: 191250**


Figure F1. Continued.

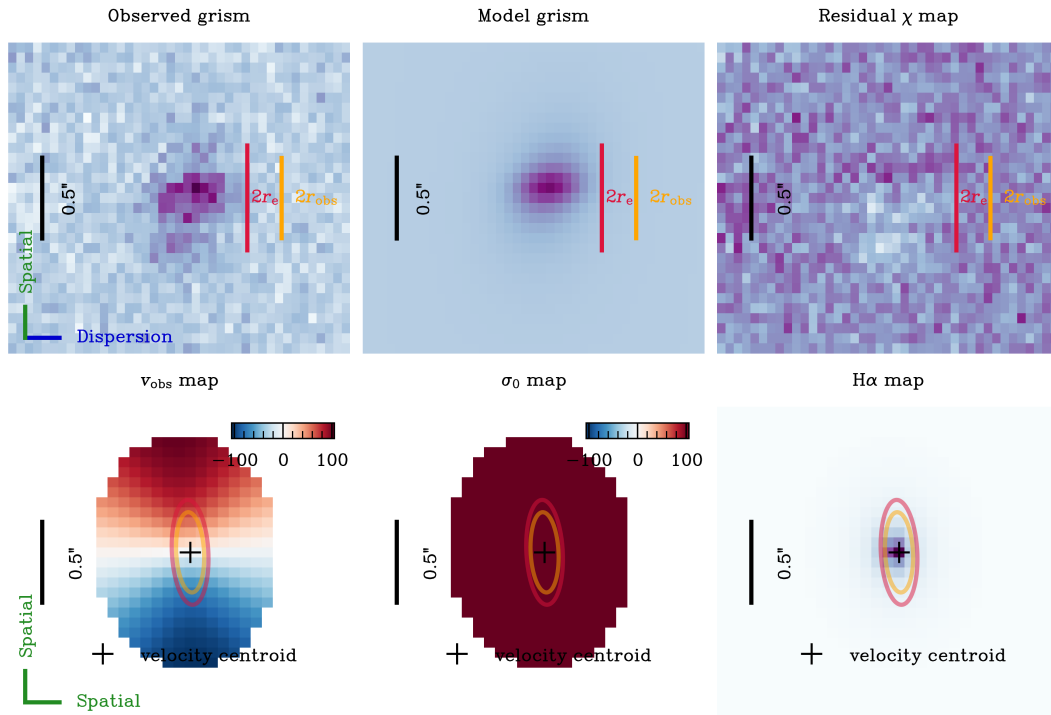
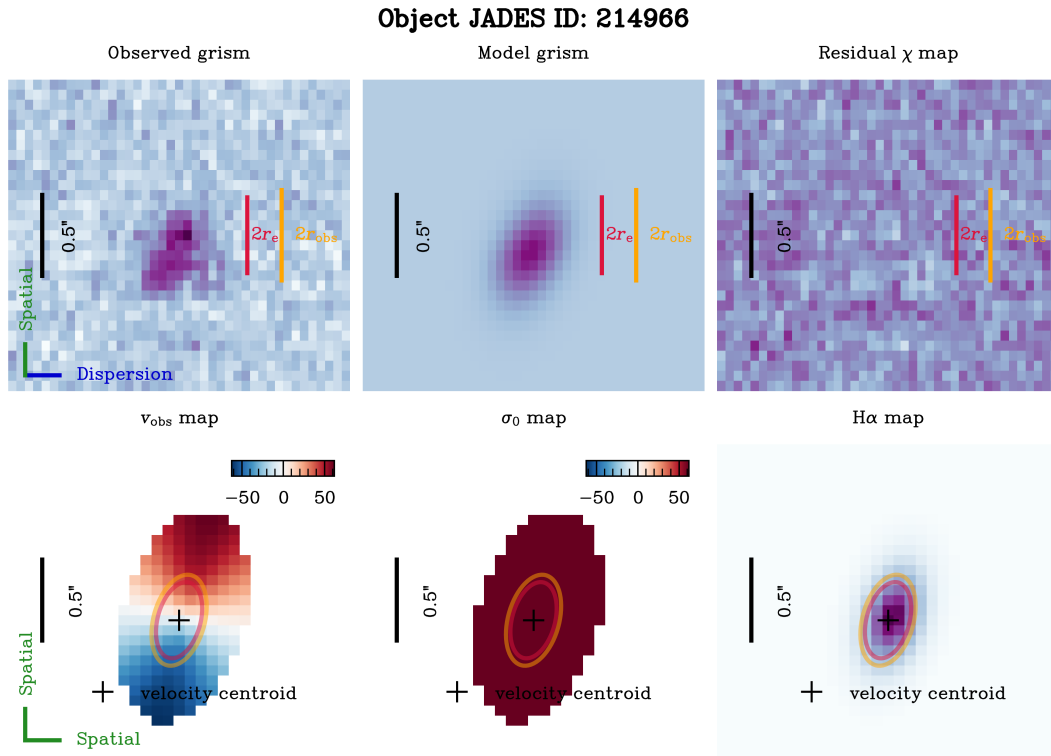
**Object JADES ID: 201125**


Figure F1. Continued.

**Figure F1.** Continued.